8-2013

NOVEL SIDE-VENT-CHANNEL BASED BLAST MITIGATION CONCEPT FOR LIGHT TACTICAL VEHICLES

Ramin Yavari
Clemson University, ryavari@clemson.edu

NOVEL SIDE-VENT-CHANNEL BASED BLAST MITIGATION CONCEPT FOR LIGHT TACTICAL VEHICLES

A Thesis
Presented to
the Graduate School of
Clemson University

In Partial Fulfillment
of the Requirements for the Degree
Master of Science
Mechanical Engineering

---

by
Ramin Yavari
August 2013

Accepted by:
Dr. Mica Grujicic, Committee Chair
Dr. Chenning Tong
Dr. Jay Ochterbeck

ABSTRACT

A new concept solution for improving survivability of the light tactical military vehicles to blast-loads resulting from a shallow-buried mine detonated underneath such vehicles is proposed and critically assessed using computational engineering methods and tools. The solution is inspired by the principle of operation of the rocket-engine nozzles, in general and the so called "***pulse detonation***" rocket engines, in particular, and is an extension of the recently introduced so-called "***blast chimney***" concept (essentially a vertical channel connecting the bottom and the roof and passing through the cabin of a light tactical vehicle).

Relative to the blast-chimney concept, the new solution offers benefits since it does not compromise the cabin space or the ability of the vehicle occupants to scout the environment and, is not expected to, degrade the vehicle's off-road structural durability/reliability. The proposed concept utilizes properly sized and shaped side-vent channels attached to the V-shaped vehicle underbody. The utility and the blast-mitigation capacity of this concept is examined in the present work using different (i.e. coupled Eulerian/Lagrangian and coupled finite-element/discrete-particle) computational methods and tools.

To maximize the blast-mitigation potential of the proposed solution, standard engineering optimization methods and tools are employed for the design of side-vent-channels. It is shown that, by proper shaping and sizing of the side-vent-channels, venting of ejected soil and supersonically-expanding gaseous detonation products can be promoted, resulting in an increase in the downward thrust on the targeted vehicle.

Furthermore, it is found that optimization of the geometry and size of the side-vent-channel solution for the maximum blast-mitigation performance, requires consideration of a tradeoff between the maximum reductions in the detonation-induced total momentum transferred

to, and the acceleration acquired by, the target vehicle. The results obtained farther confirmed the blast-mitigation effects of the side-vent-channels, although the extent of these effects is relatively small (3-4%).

Keywords: Side Vent Channels, Blast and Soil Ejecta Loading, Computational Engineering and Design-Optimization Analyses

DEDICATION

This thesis would have been impossible without the unwavering love and support from my father, Mr. Nasser Ali Yavari, my mother, Mrs. Zamzam Rabiee, my brother, Babak Yavari and my sisters Manak Yavari and Shirin Yavari to whom this thesis is dedicated.

ACKNOWLEDGEMENTS

I wish to express my sincere gratitude to my advisor, Professor Mica Grujicic, for his continuous encouragement, supervision, useful suggestions, and support throughout this research endeavor. His extensive knowledge and timely suggestions have been helpful in providing elegant solutions to the problems encountered throughout this research project.

My sincere thanks is also due to my advisory committee members Professor Chenning Tong, and Professor Jay Ochterbeck for their valuable suggestions during the course of this research project. Other faculty members of the department of Mechanical Engineering at Clemson University and the administrative staff are also greatly acknowledged for their support.

This acknowledgement will not be complete without the mention of my friends and colleagues at Clemson University whose valuable support and insightful discussions have helped mold this research into its existing form. Finally, I would like to thank my family and friends for their continuous support and encouragement during the whole tenure of my research.

The material presented in this paper is based on work supported by the Army Research Office (ARO) research contract entitled "***Concept Validation and Optimization for a Vent-based Mine-blast Mitigation System***," contract number W911NF-11-1-0518. I am also indebted to Dr. Rahul Gupta, Technical Assistant to the Director of Weapons and Materials Research Directorate, and Dr. Frederick Ferguson at U.S. Army Research Laboratory for their continuing interest and support.

TABLE OF CONTENTS

Page

LIST OF FIGURES

Figure Page

CHAPTER 1: INTRODUCTION AND BACKGROUND, AND THESIS OUTLINE

1.1. Introduction and Background

In the present work, a new concept and solution for improved survivability of light tactical military vehicles to beneath-underbody shallow-buried mine detonation is proposed, analyzed (computationally) and geometrically/functionally optimized. Therefore, the main topics most closely related to the work addressed in this thesis include: (a) identification of the main limitations of recently and currently employed light tactical vehicles; (b) examination of the phenomena and processes associated with the interaction of the soil ejecta and gaseous detonation products, resulting from the detonation of shallow-buried mines, with the target structure, and elucidation/quantification of the resulting impulse loading; (c) a brief overview of the side-vent-channel-based blast-mitigation concept, and of the computational methods and tools used to analyze and validate this concept/solution; and (d) an overview of the computational engineering analyses, including mechanical/design optimization analysis, used for validation and optimization of the blast mitigation concepts such as the side-vent channel concept. A brief overview of these four subjects is given in the remainder of this section. A more detailed description of the same will be presented in chapters 2 to 4.

Limitations of the Current Tactical Vehicles: The High Mobility Multipurpose Wheeled Vehicle (HMMWV) is the prototypical light tactical vehicle which has been used by the US military for over 20 years. This vehicle was originally developed and deployed for conventional military conflicts with well-defined frontlines, and was intended for use behind the frontline. Consequently, and not surprisingly, the recent and the ongoing asymmetric warfare, in which the distinction between frontline combat and transportation convoys has been severely blurred, has revealed the lack of necessary blast and ballistic resistance of the HMMWV. These shortcomings

of the HMMWV are the reason that bigger, heavier MRAP (Mine Resistant Ambush Protected) vehicles, have mostly replaced HMMWVs in the past conflict in Iraq and the ongoing conflict in Afghanistan. However, the improvements in IED (Improvised Explosive Devices) blast-resistance of MRAP vehicles have come with new limitations, including: (a) reduced tactical mobility/utility; (b) limited maneuverability on crowded city streets; (c) inferior fuel economy; and (d) significantly reduced deployability (these vehicles are too heavy to be driven over 70% of the world's bridges) and transportability (the MRAP vehicle weight typically exceeds the payload capacity of the CH-47 Chinook helicopter).

Mine-Detonation-Induced Impulse Loading on Target Structures: Landmines buried in or near roads have resulted in numerous instances of tactical vehicle destruction and soldier casualties incurred by the U.S. military during the recent/ongoing campaigns in Iraq and Afghanistan. When these landmines detonate, the impact of the resulting blast waves, ejected soil, mine casing/shrapnel, and expanded gaseous detonation products produces large impulsive loads on the targeted vehicle/personnel. Development of military vehicles (and general structural platforms) with a high-level of resistance/survivability to landmine-/IED-detonation entails at least the following: (a) the understanding of and ability to quantify the impulsive loads associated with the detonation of landmines buried/deployed in soil of differing compositions/constitutions; and (b) the ability to predict the kinematic and structural (including failure) response of the targeted vehicles/platforms. Acquiring such understanding and predictive ability, however, is typically quite challenging since the detonation-induced loads depend strongly on the deployed mine's shape, size and depth of burial (DOB), the distance between the soil surface and the target (the so-called stand-off distance, SOD), and the soil properties (density, particle mean size and distribution, presence of inorganic/organic matter, water content, etc.).

Due to the sensitive nature of the subject matter, only a few scientific papers and technical reports dealing with the problem of detonation of buried (explosive) charges and the resulting impulse loading experienced by the target structure are publicly available. A detailed overview of these papers/reports which are considered to be most closely related to work described the present thesis is given in chapters 2 to 4.

The Side-Vent-Channel Blast-Mitigation Concept: To address the limitations of light tactical vehicles mentioned above, the US military continues to seek innovative concepts and solutions which: (a) can improve blast-survivability of these vehicles; and (b) do so without compromising vehicle mobility/maneuverability, transportability, deployability or fuel economy. One of the concepts currently being used in the light tactical vehicles is the V-shaped vehicle hull (or simply V-hull). While the use of V-shaped hull yields blast-mitigation benefits, the extent of these benefits is not very high due to the conflicting requirements related to the minimum ground clearance of the vehicle and the maximum steepness of the V-hull.

The V-hull concept was further advanced in the present thesis by attaching to it a series of side-vent-channels. The resulting so-called side-vent-channel solution will be described in greater details, analyzed computationally and optimized geometrically and functionally in chapters 2 to 4. As will be shown later, this solution utilizes flared tubular side-vent-channels (of the appropriate cross-sectional shape and wall thickness) open at both ends. The bottom end of each tube is cut parallel to the ground (to promote inflow of the detonation by-products and soil ejecta, and to prevent crushing/crumpling of the tube inlet under blast loads) and flush with the V-hull bottom. The channels/tubes are intended to function as exhaust nozzles as in the case of the pulse-detonation engine and, thus, provide a downward thrust to the vehicle (through the gaseous-detonation products supersonic-expansion effects). The additional role of the side-vent-

channels is to reduce the blast momentum transferred to the targeted vehicle by improving the venting of the gaseous detonation products, soil ejecta and mine-casing fragments. To validate the side-vent-channel concept, detailed computational analyses involving detonation of a landmine (of a prototypical shape, size and DOB) buried underneath the vent-channel-equipped vehicle, and the interaction of the air-blast, soil ejecta, and mine-casing fragments with the vehicle will be conducted in chapters 2 to 4.

Overview of the computational engineering analyses: The computational analysis employed in chapter 2 is of a combined Lagrangian/Eulerian fluid-structure interaction (FSI) type, within which both the gaseous materials (i.e. air and detonation products) and non-vehicle solid materials (i.e. soil and mine fragments) are modeled as a multi-component Eulerian material. Consequently, this type of analysis suffered from at least the following two major deficiencies: (a) inaccuracies/uncertainties related to the definition of the boundaries between different components of the Eulerian material, and between the Eulerian and vehicle-Lagrangian materials; and (b) inability to take into account the granular/discrete character of the soil ejecta. Despite these deficiencies, the computational analyses carried out in chapter 2 established, at least in semi-quantitative terms, that the side-vent-channels: (i) lower the blast impulse transferred to the vehicle, by promoting venting of soil ejecta, gaseous detonation products and mine-casing fragments resulting from a mine-blast underneath the vehicle; (ii) lower the possibility for the vehicle lift-off from the ground, by promoting supersonic expansion of gaseous detonation products exiting the channel, and thereby helping to create a downward thrust on the vehicle; (iii) do not limit the mobility of the occupants within the vehicle and their ability to survey the surroundings, since the vent-channels do not pass through the vehicle cabin; and (iv) do not compromise vehicle off-road structural reliability and durability, since the side-vent-channels

attached to the V-hull do not considerably increase vehicle-frame rigidity and, thus, do not significantly increase the rate of vehicle-frame fatigue-induced failure.

The aforementioned deficiencies of the combined Eulerian/Lagrangian analysis employed in the computational investigation of the side-vent-channel concept in chapter 2 were addressed in chapter 3. In chapter 3, the side-vent-channel concept/solution is re-examined using combined Finite-Element/Discrete-Particle computational methods and tools. Within this approach, all non-vehicle materials are treated as assemblies of discrete particles. The combined finite-element/discrete-particle analysis reconfirmed the aforementioned findings (yielded by the combined Eulerian/Lagrangian computational analysis) regarding the blast-mitigation utility and efficacy of the side-vent-channel solution.

Geometrical and size optimization of the proposed side-vent-channel concept/solution for mitigation of the blast-loads resulting from a shallow-buried mine detonated underneath a light tactical vehicle is carried out in chapter 4. By proper shaping and sizing of the side-vent-channels, venting of ejected soil and supersonically-expanding gaseous detonation products is promoted in order to generate a downward thrust on the targeted vehicle. In the course of the optimization procedure, the geometry and size of the side-vent-channel solution are varied in order to attain maximum blast-mitigation performance (as defined by a tradeoff between the maximum reductions in the detonation-induced total momentum transferred to, and the acceleration acquired by, the target vehicle).

1.2 Thesis Outline

The present thesis is organized in the following way: combined Eulerian/Lagrangian computational analysis of the newly proposed side-vent-channel blast mitigation concept is carried out in chapter 2. Re-examination of the same solution using combined Finite-Element/Discrete-Particle computational analysis is carried out in chapter 3. Geometrical and shape optimization of the side-vent-channel blast-mitigation solution for maximum blast-mitigation performance is presented in chapter 4. A summary of the main findings and conclusions obtained in the present thesis as well as suggestions for the future work are presented in chapter 5.

CHAPTER 2: A NOVEL BLAST-MITIGATION CONCEPT FOR LIGHT TACTICAL VEHICLES

2.1. Abstract

A new concept solution for improving blast survivability of the light tactical military vehicles is proposed and critically assessed using computational engineering methods and tools. The solution is inspired by the principle of operation of the rocket-engine nozzles, in general and the so called "***pulse detonation***" rocket engines, in particular, and is an extension of the recently introduced so-called "***blast chimney***" concept (essentially a vertical channel connecting the bottom and the roof and passing through the cabin of a light tactical vehicle). Relative to the blast-chimney concept, the new solution offers benefits since it does not compromise the cabin space or the ability of the vehicle occupants to scout the environment and, is not expected to, degrade the vehicle's structural durability/reliability. The proposed concept utilizes side vent channels attached to the V-shaped vehicle underbody whose geometry is optimized with respect to the attainment of the maximum downward thrust on the vehicle. In the course of the channel design optimization, analytical and computational analyses of supersonic flow (analogous to the one often used in the case of the pulse detonation engine) are employed. The preliminary results obtained reveal the beneficial effects of the side channels in reducing the blast momentum, although the extent of these effects is quite small (2-4%).

2.2. Introduction

In the present work, a new concept solution for improving blast survivability of the light tactical military vehicles is proposed and investigated using computational engineering methods and tools. The solution is an extension of the recently introduced so-called "***blast chimney***" concept [1] and is also inspired by the principle of operation of the rocket-engine nozzles, in general and the so called "***pulse detonation***" rocket engines, in particular [2]. Hence, the main topics to be overviewed in this introductory section of the present manuscript include: (a) main limitations of the (light) tactical vehicles currently in use; (b) the blast chimney blast- mitigation concept; (c) principle of operation of a rocket engine nozzle; and (d) the principles of operation of pulse-detonation rocket engines.

Limitations of the Current Tactical Vehicles: The HMMWV (High Mobility Multipurpose Wheeled Vehicle) is the prototypical light tactical vehicle used by the US military. This vehicle was designed and developed during the cold war and, not surprisingly, has been found lacking the necessary blast and ballistic resistance in the ongoing asymmetric warfare, in which the distinction between front line combat and transportation convoys has been severely blurred. Thus, in conflicts in Iraq and Afghanistan, HMMWVs have been largely replaced by larger, heavier MRAP (Mine Resistant Ambush Protected) vehicles, which have been specifically designed for resistance to IEDs (Improvised Explosive Devices) blast [1].

However, the added mass which plays a key role in the superior IED survivability of the MRAP, also negatively affects other performance aspects of this vehicle such as: (a) tactical utility/mobility is severely compromised relative to that of the HMMWV; (b) diminished maneuverability on narrow city streets; (c) poor fuel economy; (d) its weight exceeds the payload capacity of the CH-47 Chinook helicopter [1] severely affecting its transportability; and (e) its

weight exceeds the load carrying capacity of 72% of the world's bridges [3] seriously hampering its deployment.

Blast Chimney Concept: To fill the need for lighter, high-mobility/maneuverability, fuel efficient, transportable and deployable light tactical vehicles with improved mine/IED survivability, HMMWV manufacturer AM General LLC, South Bend, Indiana and DoD Contractor Hardwire LLC, Pocomoke City, Maryland are in the process of developing a new generation of HMMWVs. While a number of blast mitigation solutions (e.g. energy absorbing floor, shock-absorbing seats, a gunner protection system, blast-resistant doors etc.) [1, 4] are being utilized in the new HMMWV, the key new concept introduced is the so-called "***blast chimney***". The blast chimney is simply a vertical channel which connects the vehicle bottom to its roof and enables the venting of soil ejecta, gaseous detonation products and mine casing fragments [1, 4] resulting from a mine blast underneath the vehicle.

Due to the sensitive nature of the subject matter, relatively little has been reported in the open literature regarding the blast mitigation potential of the blast chimney concept. Among the ones reported to the public, the following are found to be the most relevant: (a) In eleven tests conducted by the Army Test Center, the 16300 pound enhanced HMMWV provided the mandatory occupant survivability level required of the smallest MRAPs (M-ATVs, Mine Resistant Ambush Protected All-Terrain Vehicles), which weigh approximately 30000 pounds [4]. It should be noted that it is not claimed here that the occupant survivability level offered by the enhanced HMMWV matches that offered by the M-ATV but that it merely meets the occupant survivability level minimal requirements for the M-ATVs; (b) In a DARPA-sponsored investigation, an attempt is being made to decouple and assess the contributions of all the blast-mitigation solutions used in the enhanced HMMWV and to specifically isolate the blast

mitigation potential of the blast chimney [4]. The results obtained so far are inconclusive. In particular, it is presently unclear, to what extent the observed enhanced blast mitigation performance is a consequence of the venting effects offered by the blast chimney and to what extent it is the result of an enhanced structural rigidity of the cabin arising from the additional bottom to roof connections provided by the chimney[4]; (c) Not surprisingly, it has been found that the incorporation of the chimney which runs through the vehicle cabin limits the mobility of the occupants within the vehicle and their ability to survey the surroundings [4]; and (d) Off-road vehicle-testing performance studies have indicated a loss in the vehicle structural reliability and durability which has been currently attributed to the enhanced rate of vehicle-frame fatigue-induced failure which, in turn, has been linked with the aforementioned increased cabin rigidity [4].

While the initial primary function of the chimney was to enable venting of soil ejecta, gaseous detonation products and mine casing fragments (and thus lower the blast impulse transferred to the vehicle), the aforementioned testing has suggested a two-fold action of the blast chimney: (a) the venting effect described above; and (b) a downward thrust imparted to the vehicle by the supersonically expanding gaseous detonation products exiting the blast chimney [5]. It should be noted that the blast venting effect offered by the blast chimney complements the reduced blast-impulse effect offered by the conventional V-shaped vehicle hulls. To demonstrate this point, simple schematics of three vehicle hull configurations/geometries are depicted in Figures 2-1(a)-(c). The conventional V-hull is depicted in Figure 2-1(a). In this case, the blast mitigation performance increases with an increase in the V-hull steepness. However, constraints associated with vehicle ground clearance and height limit the maximum allowable V-hull steepness. A truncated V-hull design is depicted in Figure 2-1(b). In this case, the blast mitigation

performance is enhanced relative to that offered by the design depicted in Figure 2-1(a) since the benefits (decreased blast impulse) offered by the increased steepness of the V-hull outweighs the penalty (i.e. increased blast impulse) incurred due to the small flat section. As seen in Figure 2-1(c), incorporation of a chimney, allows the gaseous detonation products, soil ejecta and mine casing fragments under the chimney to be vented, while still permitting highly steep V-hull sides [5].

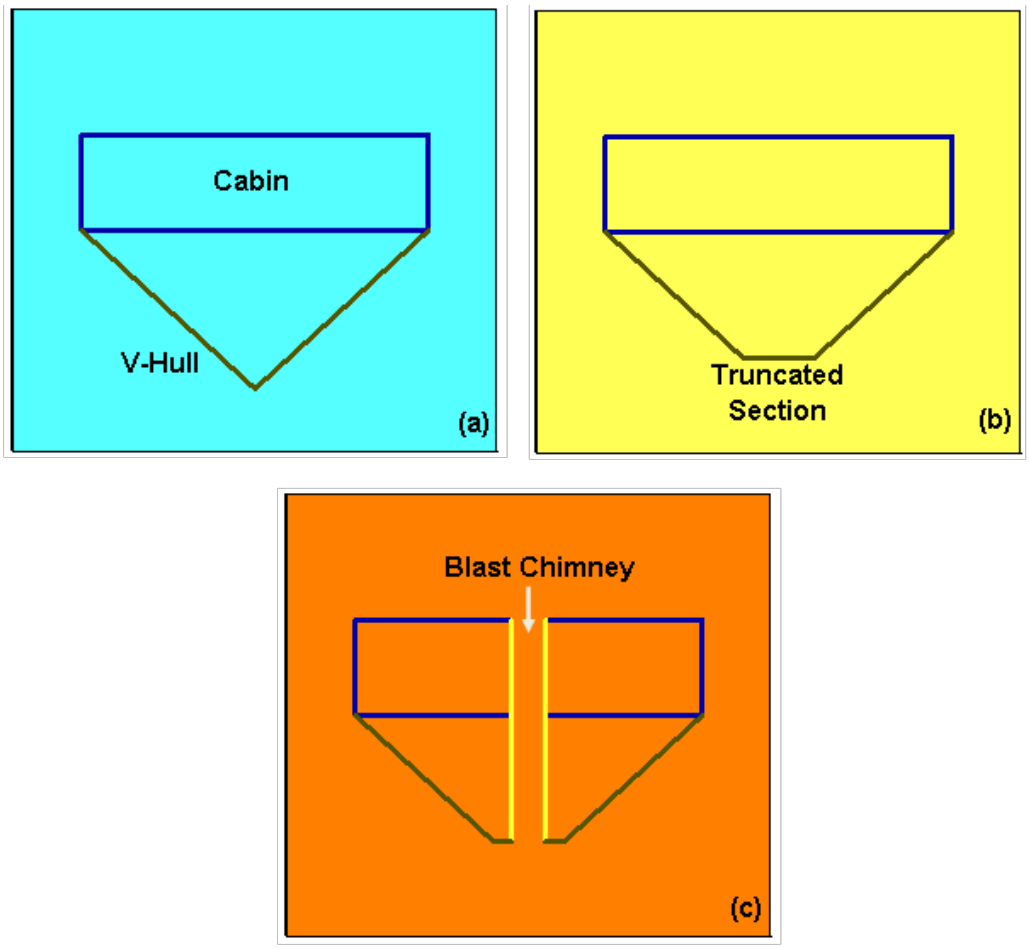

Figure 2–1 Three blast-mitigation vehicle-hull concepts: (a) V-shaped hull; (b) truncated V-shaped hull; and (c) same as (b) but with addition of a blast chimney.

As mentioned earlier, the high-pressure supersonically expanding gaseous detonation products exiting the chimney provide a down-ward thrust to the vehicle, offsetting some of the blast-induced impulse delivered to the vehicle thus lowering the possibility for the vehicle lift-off from the ground [5]. The physical principles governing the creation of the down-ward thrust are analogous to those encountered in the context of rocket engines and are reviewed below.

Principle of Operation of a Rocket Engine Nozzle: In the subsonic flow regime, a fluid can be accelerated by passing it through a converging nozzle. In this case, to ensure constancy of the mass flow rate, the fluid velocity at the nozzle exit must be higher than that at the nozzle inlet. The force required to accelerate the fluid in the subsonic regime is derived solely from the higher upstream pressure. The effect of higher upstream pressure is propagated through the advancing fluid at the speed of sound. Hence, once the fluid at the nozzle exit reaches the sonic velocity, further increase in the fluid upstream pressure will not cause an additional increase in the fluid exit velocity. Simply stated, since the fluid at the nozzle exit flows at the sonic speed, the information regarding the increased upstream pressure never reaches the exiting fluid. A converging nozzle in which the fluid exit velocity is the sonic velocity is referred to as being in the "***choked-flow***" condition.

The analysis presented above shows that the fluid cannot be accelerated into the supersonic regime by simply pushing-off against the upstream fluid. Consequently, to achieve the supersonic flow condition, the fluid should be provided with a forward facing solid surface upon which the flow can exert a force. This is the reason that a typical rocket engine nozzle contains not only a converging but also a subsequent diverging section. In this type of nozzle design, the converging section accelerates the fluid from subsonic to sonic velocity while the diverging

section accelerates the fluid from a sonic to supersonic velocity. The converging-diverging rocket-engine nozzle design described here is typically referred to as the "***de Laval***" nozzle.

As the fluid is being accelerated into the supersonic regime, it exerts a force (in the direction opposite to the flow) on the walls of the diverging sections of the nozzle. It is this force that provides a thrust/propulsion to the rocket. To maximize the amount of thrust for a given level of the fluid pressure at the nozzle throat (transition between the converging and diverging sections of the nozzle), the exit velocity of the fluid (from the diverging section of the nozzle) must be maximized while ensuring that the exiting fluid is at the ambient pressure condition. This condition is generally referred to as the "***ideally-expanded***" fluid flow. If this condition is not attained, the fluid flow could be either "***under-expanded***" (the fluid exit pressure is higher than the ambient pressure) or "***over-expanded***" (the fluid exit pressure is lower than the ambient pressure). Both of these conditions are undesirable since they yield a lower value of the propulsion thrust. Specifically, in the case of the under-expanded flow, the potential of the expanding fluid to push-off the walls of the diverging section of the nozzle has been under-utilized. On the other hand, in the case of the over-expanded flow, a stationary shock is formed at the nozzle exit which reduces effectively the momentum of the fluid exiting the nozzle.

To attain the ideally-expanded flow condition for the given values of the fluid pressure at the nozzle throat and the ambient pressure, one typically carries out a one dimensional steady (time-invariant) isentropic (no thermal conduction or energy exchange) fluid-expansion analysis. The outcome of this analysis is the optimal nozzle exit-to-throat area ratio which provides the maximum propulsion thrust. Below, an example of this analysis which utilizes the mass and energy (but not linear momentum) conservation equations is provided. It should be noted that the

identical final results could be obtained using an analogous analysis which combines the mass and the linear momentum conservation equations.

For a calorically perfect (i.e. temperature-invariant specific heat), inviscid (i.e. zero viscosity), ideal gas undergoing adiabatic, one-dimensional expansion, the conservation of energy requires:

$$C_p T_1 + \frac{V_1^2}{2} = C_p T_2 + \frac{V_2^2}{2} \tag{2-1}$$

where C_p denotes constant-pressure specific heat, T the absolute temperature, V the fluid velocity and subscripts 1 and 2 refer to the nozzle inlet (more precisely the throat) and the exit conditions. It should be noted that the two terms on each side of Eq. (2-1), denote respectively the mass-based thermal and kinetic energy-density components. Eq. (2-1) can be rearranged as:

$$\frac{T_2}{T_1} = \frac{1 + V_1^2/(2C_p T_1)}{1 + V_2^2/(2C_p T_2)} \tag{2-2}$$

Using the definition of the Mach number $M=V/C_s$, where C_s ($=\sqrt{\gamma RT}$, γ is the constant-pressure to the constant-volume specific-heat ratio, R is the gas-specific gas constant) denotes the speed of sound in the fluid, one can show that $V^2/(2C_p T) = \frac{1}{2}(\gamma - 1)M^2$ and, in turn, rewrite Eq. (2-2) as:

$$\frac{T_2}{T_1} = \frac{1 + \frac{1}{2}(\gamma - 1)M_1^2}{1 + \frac{1}{2}(\gamma - 1)M_2^2} \tag{2-3}$$

Using the functional relationship for a P-T isentrope, where P denotes pressure, $PT^{\frac{\gamma-1}{\gamma}} = Const.$, Eq. (2-3) could be recast as:

$$\frac{P_2}{P_1} = \left(\frac{T_2}{T_1}\right)^{\frac{\gamma}{\gamma-1}} = \left(\frac{1+\frac{1}{2}(\gamma-1)M_1^2}{1+\frac{1}{2}(\gamma-1)M_2^2}\right)^{\frac{\gamma}{\gamma-1}} \tag{2-4}$$

or

$$M_2 = \sqrt{\left(\frac{2}{\gamma-1}+M_1^2\right)\left(\frac{P_1}{P_2}\right)^{\frac{\gamma-1}{\gamma}} - \frac{2}{\gamma-1}} \tag{2-5}$$

For the given values of the nozzle throat fluid pressure P_1, velocity V_1 and temperature T_1 and the nozzle exit fluid pressure P_2 (= ambient pressure), Eq. (2-5) enables the calculation of the fluid exit Mach number associated with the ideally-expanded flow. However, one would also like to know the nozzle exit-to-throat area ratio which should be used to attain this condition. This can be done through the use of the mass conservation equation which can be defined as:

$$A_1\rho_1V_1 = A_2\rho_2V_2 \tag{2-6}$$

or

$$\frac{A_2}{A_1} = \left(\frac{V_1}{V_2}\right)\left(\frac{\rho_1}{\rho_2}\right) \tag{2-7}$$

where ρ represents mass density and A the nozzle cross-sectional area. Using the functional relationship for a P-ρ isentrope, $\frac{P}{\rho^\gamma} = Const.$, the aforementioned P-T isentropic relation and the Mach number definition, Eq. (2-7) can be rewritten as:

$$\frac{A_2}{A_1} = \left(\frac{P_1}{P_2}\right)^{\frac{1+\gamma}{2\gamma}}\left(\frac{M_1}{M_2}\right) \tag{2-8}$$

Eq. (2-8) shows that once the state of the fluid (including its velocity) at the nozzle throat and the ambient pressure are known, one can compute the optimal nozzle exit to throat area ratio (associated with the "***ideally-expanded***" fluid-flow condition) which yields the maximum (backward) thrust on the diverging section of the nozzle.

An example of the results obtained in this type of analysis is depicted in Figure 2-2 for the case of air with the following air-material parameters, the nozzle throat material states and the ambient-air pressure: γ=1.4, P_1=3MPa, ρ_1= 4kg/m3, V_1=900m/s and P_2=101.3kPa. The optimal nozzle cross-section area ratio is denoted by a solid circle in this figure. It should be noted that the functional relationship between exit Mach number and the area ratio, Eqs. (2-5) and (2-8), are valid only under the ideal expansion conditions i.e. when the nozzle exit pressure is equal to the ambient pressure. When this condition is not met, the exit momentum of the fluid is altered/lowered by the presence of a stationary decompression simple wave at the nozzle exit (in the case of an under-expanded flow) or by the presence of a stationary (compression) shock (in the case of an over-expanded flow). While an analysis involving the contribution of these waves/ shocks is beyond the scope of the present work, the exit momentum predictions based on the inclusion of the shock effects is also shown in Figure 2-2. Examination of the results displayed in Figure 2-2 shows that the optimum nozzle cross-sectional area ratio is ca. 5.06.

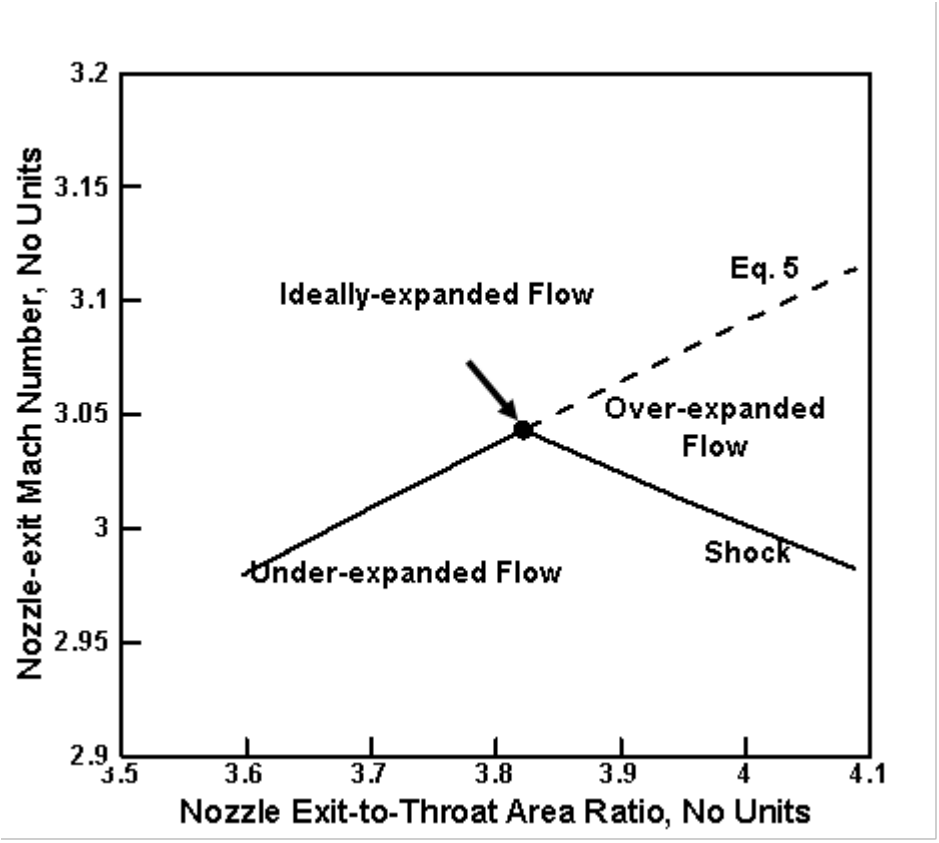

Figure 2–2 The effect of the nozzle exit-to-throat area ratio on the exit Mach number (see text for details).

To calculate the associated thrust force, F_{thrust}, the linear momentum conservation equation should be employed as:

$$A_2\rho_2V_2^2 - A_1\rho_1V_1^2 = (P_1A_1 - P_2A_2) + F_{thrust} \tag{2-9}$$

The net quantity on each side of Eq. (2-9) represents the total force acting on the fluid within the nozzle, F_{Fluid}. By combining Eqs. (2-6) and (2-9) with the Mach number definition and the P-ρ isentrope, the fluid force per unit nozzle inlet cross-sectional area can be defined as:

$$\frac{F_{Fluid}}{A_1} = \rho_1V_1\left(M_2\sqrt{\gamma\frac{P_2}{\rho_1\left(\frac{P_2}{P_1}\right)^{\frac{1}{\gamma}}}} - V_1\right) \tag{2-10}$$

For the aforementioned air inlet states and the normal ambient pressure, the fluid force per unit nozzle inlet cross-sectional area corresponding to the ideal nozzle cross-sectional area ratio was found to be ca. 4.02 MN/m^2. The calculation of the thrust force requires the knowledge of the nozzle inlet and outlet cross-sectional areas.

Principle of Operation of the Pulse-detonation Rocket Engine: The rocket engine nozzle design analysis presented above deals with a steady, continuous flow and assumes the existence of sonic flow at the nozzle throat. These flow conditions are generally not encountered in the case of a mine-detonation event. That is, the flow is in the transient (not steady) state, it involves a single pulse (rather than being continuous) and the gaseous detonation products, from the onset, are already in the supersonic flow regime. Thus, a natural question arises as to whether the aforementioned analysis is adequate or even relevant to the problem of blast-mitigation system design. To address this question, it is first recognized that there are some similarities between the so-called "***pulse detonation***" engine and a prototypical mine detonation event. These similarities

pertain to the characteristic times (several hundred microseconds) of the associated blast events and in the fact that the fluid in question (detonation by-products and fuel/oxidizer mixture combustion products) are, from the onset, in the supersonic flow regime. Consequently, a brief overview of the principles of operation of a pulse detonation engine is given in this section.

The pulse detonation engine (the subject of active ongoing research and development) is an intermittent combustion engine and is a variant of the pulse jet engine, a simple engine with no moving parts. The latter engine was famously employed in the German V-1 "***buzz bomb***" during World War II. The main difference between the pulse detonation engine and most of the current rocket engines (including pulse jet engines) is that in the former case fuel oxidizer combustion (detonation) takes place at a supersonic speed while in the latter case the combustion rate is subsonic (i.e. it is in the deflagration regime). As will be discussed below, this difference results in an improved thermodynamic efficiency of the pulse detonation engine.

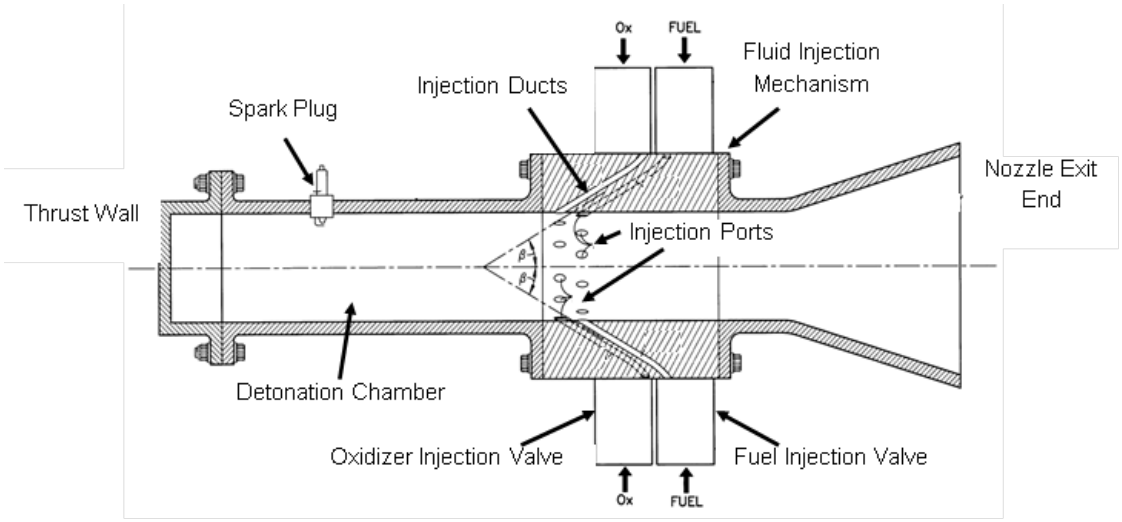

Figure 2–3 Pulse detonation engine with an aerodynamic valve.

A pulse detonation engine, Figure 2-3, typically consists of a combustion/detonation chamber equipped with a fuel-oxidizer inlet valve, a thrust wall (at the front) and a diverging exhaust nozzle (at the back). A single engine cycle begins with air/oxidizer mixture entering through the inlet valve. The inlet valve is then closed and fuel is injected to create a detonable mixture. The mixture is ignited from the front end, resulting in a detonation wave which travels rearward and exits through the exhaust nozzle, resulting in a short term, and high-velocity outflow of combustion products. This process creates under-pressure in the front portion of the combustion chamber and provides the conditions necessary for the intake of the fuel-oxidizer mixture for the next cycle. Due to the isentropic expansion of the combustion products exiting the exhaust nozzle, intermittent thrust is generated in the forward direction.

As discussed earlier, in contrast to most rocket engines, in general, and pulse jet engines in particular, which rely upon the rapid deflagration of the fuel-oxidizer mixture, pulse detonation engines utilize detonation of the same mixture. In other words, while in the case of a pulse jet engine the combustion front advances relatively slowly (since the rate of combustion is limited by heat conduction/convection); in the case of the pulse-detonation engine the combustion front advances at a supersonic velocity (since the combustion process is initiated by the arrival of the shock/detonation wave). This difference in the rate of combustion gives rise to several important advantages for the pulse detonation engine such as: (a) improved thermodynamic efficiency due to the fact that combustion takes place under constant volume rather than constant pressure conditions [7]. Simply stated, in the case of pulse jet engines, the combustion-induced shock wave expels a considerable amount of un-burnt fuel-oxidizer mixture through the nozzle exit (while maintaining fairly constant pressure level within the combustion chamber). In the case of the pulse detonation engines on the other hand, effectively no expulsion of the un-burnt

fuel/oxidizer mixture takes place; (b) as a consequence of (a) significant improvements are attained in the specific impulse generated by the engine; and (c) due to a very short cycle time (several 100's of microseconds), the pulse detonation engines run, for all practical purposes, continuously, which results in greatly reduced vibrations.

When designing a rocket engine, a substantial effort is invested in the optimizing the shape of the exhaust nozzle in order to maximize the amount of forward propulsion thrust. It should be noted that, due to the intermittent character of the combustion process, the nozzle-design optimization in the case of pulse detonation engines is more challenging than in the case of the conventional (continuous flow) rocket engines. Specifically, in the case of the continuous flow engines, variations in the combustion chamber pressure are relatively small and, hence, the exhaust nozzle design is optimized to a relatively narrow range of nozzle inlet-to-outlet pressure ratios. In sharp contrast, in the case of pulse detonation engines, the pressure ratio across the nozzle peaks with the arrival of the detonation wave at the nozzle inlet and then diminishes as the combustion products exit the combustion chamber through the exhaust nozzle. This process is typically referred to as "***blowdown***" [6]. It is this variability of the pressure ratio across the nozzle which makes its design and optimization a complicated process.

The problem of the optimal design of the exhaust nozzle for the pulse detonation engine has been recently addressed by Owens and Hanson [6] who studied the effect of exhaust nozzle shapes (a straight tube, a converging-diverging nozzle, and a diverging nozzle) on the specific impulse delivered. They employed a numerical, quasi-one-dimensional analysis in which kinetics of the combustion elementary chemical reactions is combined with the mass, momentum and energy conservation equations in order to determine the optimal nozzle shape and the area ratios for maximum propulsion thrust. The computational results were subsequently validated in a

companion experimental investigation. Their investigation yielded two important findings: (a) among the nozzle shapes tested, the diverging nozzle produced the maximum propulsion thrust; and (b) for each of the three nozzle shapes tested, the optimum area ratio was found to be quite close to the one that could be obtained through the use of a steady isentropic expansion-flow analysis (of the type discussed in the previous section) in which the (constant) pressure ratio across the nozzle is replaced with the time-average of the corresponding variable pressure ratio over the duration of a single combustion cycle. The latter finding is quite interesting since it suggests that, despite the fact that many of the conditions associated with the steady isentropic-expansion analysis are not met in the course of a pulse detonation engine cycle, this analysis may still be relevant when carrying out design optimization of a pulse detonation engine exhaust nozzle.

Objective: In the present work, an attempt is made to develop a concept level solution for an alternative blast mitigation system, which in contrast to the blast chimney solution, does not compromise structural durability or intrude into the interior space of the vehicle, as will be discussed in greater detail in the next section. This alternative solution, utilizes side vent channels attached to the V-shaped vehicle underbody. The main purpose of the channels is to direct flow upward at maximum velocity and, thus, maximize the downward thrust on the vehicle. Channel shaping was conducted by combining a conventional design optimization methodology with the analytical and computational analyses of supersonic flow (analogous to the ones overviewed above in the case of the pulse detonation engine).

Organization: In Section II, a brief description is provided of the proposed blast-mitigation concept. The utility of the continuous-steady isentropic expansion analysis in identifying the optimal area-ratio across the channels/tubes which maximizes the downward thrust is addressed

in Section III. A simplified two-dimensional mine blast computational analysis is carried out in Section IV. Section V contains a more refined three-dimensional analysis of the same problem. The main conclusions resulting from the present work are listed in Section VI.

2.3. Concept Description

In this section, a brief description is provided of the new blast mitigation concept proposed in the present work. To prevent potential misuse, of the ideas proposed and the results obtained in the present work, the term "***vehicle***" will be replaced with the term "***surrogate box structure***" (SBS).

The proposed concept is depicted schematically in Figure 2-4 and involves the use of tubes/channels (of the appropriate cross sectional shape and wall thickness) attached to the underside of a V-shaped hull and open at both ends. The bottom end of each tube is cut parallel to the ground (to promote inflow of the detonation by-products and soil ejecta and to prevent structural collapse (crushing) of the tube inlet under blast loads) and flush with the V-hull bottom. The channels/tubes are intended to function as exhaust nozzles in the case of the pulse-detonation engine and, thus, provide a downward thrust to the vehicle. The secondary role of the channels/tubes is to enable the venting of the gaseous detonation products, soil ejecta and mine-casing fragments.

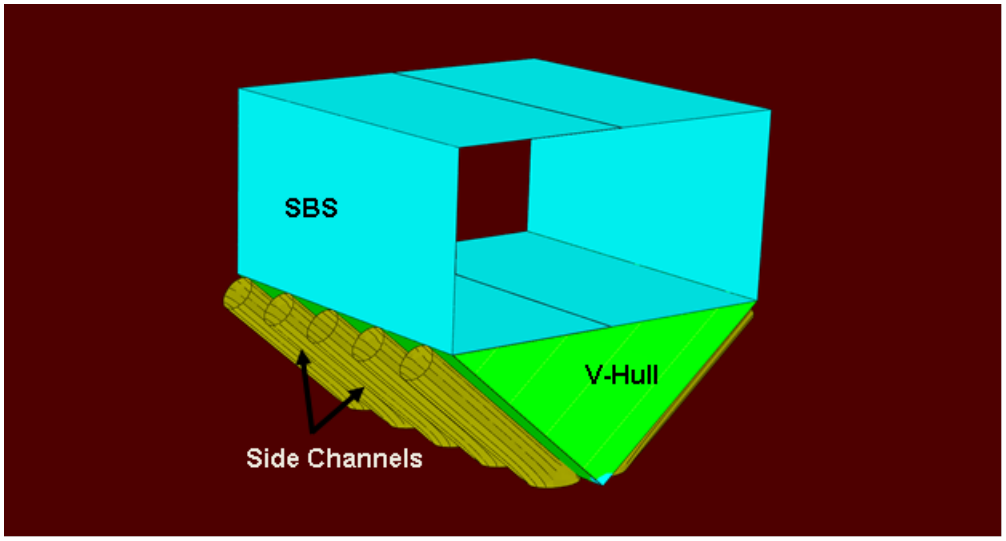

Figure 2–4 Side channels/tubes based blast-mitigation concept proposed in the present work.

The concept proposed here is a natural extension of the blast chimney solution which tries to address the main short comings of the blast chimney concept (i.e. loss of cabin space, inability of the vehicle occupants to scout the environment and a reduction in the vehicle's structural durability/reliability). In addition, the concept proposed here builds on the similarities between a mine detonation event and a pulse detonation engine combustion cycle. In particular, explosion of a mine is a short duration event which creates shock waves in air and the impingement of these waves on to the target structure causes a momentum transfer. Similar events occur in the course of a pulse detonation engine cycle except that the shock waves propagate through the fuel-oxidizer mixture and give rise to mixture combustion.

The geometry of the channels/tubes is optimized in order to maximize the downward thrust resulting from the supersonic expansion of the gaseous detonation products. Specific design parameters include variation of tube cross-sectional area along its length and the orientation of the tube top-end cut.

In the channel tube design optimization analysis both the analytical, steady isentropic expansion analysis (with the stagnation pressure equal to the time averaged detonation product pressure at the channel/tube inlet) and a transient numerical analysis are employed. The analytical analysis is identical to the one reviewed in the previous section while the numerical analysis is described in greater detail in the next section.

2.4. Continuous-Steady vs. Pulsed-Transient Flow Analyses

The two main objectives of the work presented in this section are: (a) to establish the capability of the employed computational methods and tools for reproducing the basic results yielded by the continuous-steady isentropic expansion analysis; and (b) to address the question of utility of the continuous-steady isentropic expansion analysis in identifying the optimal area-ratio across the channels/tubes which maximizes the downward thrust on the SBS (under pulsed-transient flow, i.e. blast-loading conditions). The steady isentropic analysis was presented in Section I, where it was shown that the knowledge of the fluid inlet states and properties as well as the ambient pressure is required in order to compute the optimum channel area ratio along with the exit Mach number and the thrust force per unit inlet cross-sectional area. Details of the numerical pulsed-transient flow analysis are presented below. It should be noted that, in the present analysis, the presence of soil within the fluid passing through the channel is not accounted for, either explicitly or implicitly. Thus, the analysis may be deemed more relevant to the case of ground-laid explosives and less relevant to the buried-mine detonation cases.

2.4.1. Steady/Transient Flow Computational Procedure

Computational Domain: A typical computational domain used in the present analysis is depicted in Figure 2-5. It contains a circular cross-section channel in which the end segments have constant (but different) radii, and in the middle section the radius transitions linearly along the channel length. To take advantage of the symmetry of the model, only one quarter of the channel is explicitly analyzed. Typically, the computational domain is meshed using ca. 10000 hexahedron first order reduced integration Eulerian elements.

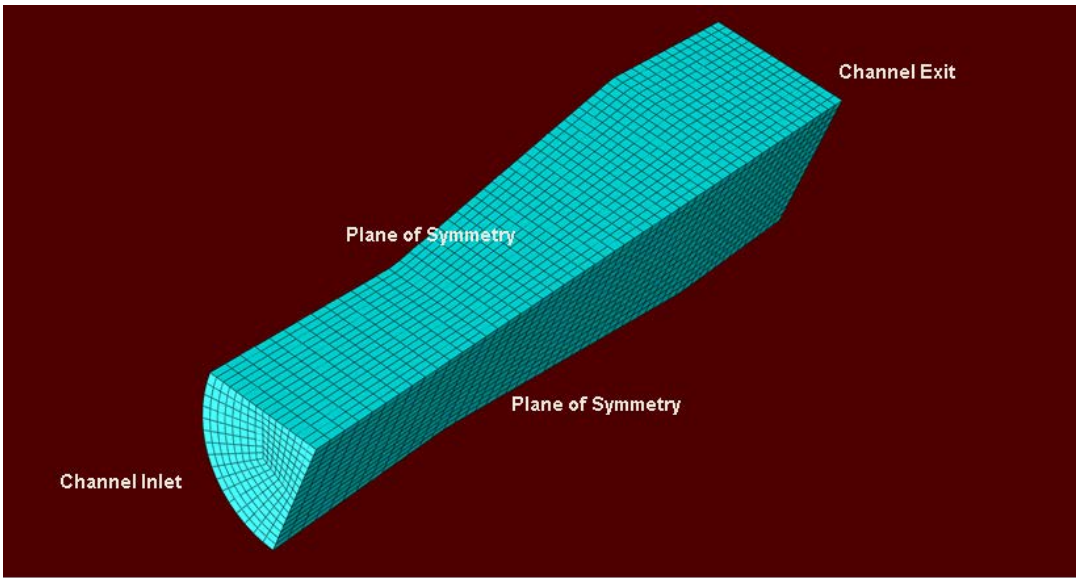

Figure 2–5 prototypical computational domain used in the transient finite element analysis of the fluid flow through the side channel.

Computational Analysis Type: The fluid flow through the channel is analyzed using a thermo-mechanical purely Eulerian formulation within which the mesh is fixed in space while the fluid is allowed to flow through it. The flow is assumed to be of a laminar character since the finite element program used, ABAQUS/Explicit [8] does not contain any turbulence models. While it is beyond the scope of the present work to provide quantitative assessment of the turbulence effects, these effects are expected not to have a first-order influence on the results reported later in this section. This conjecture is based on the fact that the flow fields in the present case are dominated by the strong, uni-directional/axial component of the field variables.

Initial Conditions: The computational domain is initially filled with different material states, depending on the main objective of the computational analysis. That is, in the analysis in which the main objective was validation of the employed numerical methods and tools, the initial material state is set equal to that predicted by the continuous-steady isentropic expansion analysis for the inlet pressure of 3 MPa, inlet fluid density of 4 kg/m^3, inlet particle velocity of 900 m/s and the ambient value of the outlet pressure. On the other hand, in the computational investigations in which the main objective was establishment of the utility of the continuous-steady isentropic expansion analysis, the following material states were assigned: (a) the initial straight section of the channel is assigned the initial pressure, density, temperature and particle velocity consistent with the von Neumann point source approach [22], explosive energy E_0=10 MJ, and the channel-inlet stand-off distance of 1 m [9-12]. Within the point-source approach, the explosive charge is shrunken to a point and, under an "***ideal-explosion assumption***" (i.e. under a condition that the ambient pressure is so small in comparison to the detonation pressure that it could be neglected), the similarity property of the point-source solution can be taken advantage of in order to compute spatial distribution of the material states in the vicinity of the point-source.

Clearly, due to a rapid decrease in the detonation pressure with time, the ideal-explosion assumption is valid only over a very short post-detonation time. A summary of the point-source results generated in the present work, following the procedure described in Ref. [22], is given in Figures 2-6(a)-(d). In these figures, a standoff distance (relative to the detonation site) normalized by the radial position (also relative to the detonation site) of the blast-wave front is plotted along the x-axis. As far as the y-axis is concerned, it displays, in each case, the appropriate material-state variable normalized by its value at the blast-wave front. The material-state variables depicted in Figures 2-6(a)-(d) are respectively: mass density, particle velocity, static pressure and absolute temperature. The aforementioned similarity property of the point-source solution simply states that the plots shown in Figures 2-6(a)-(d) are time invariant, as long as the ideal-explosion condition is satisfied; and (b) the remainder of the channel is filled with quiescent, atmospheric-pressure air.

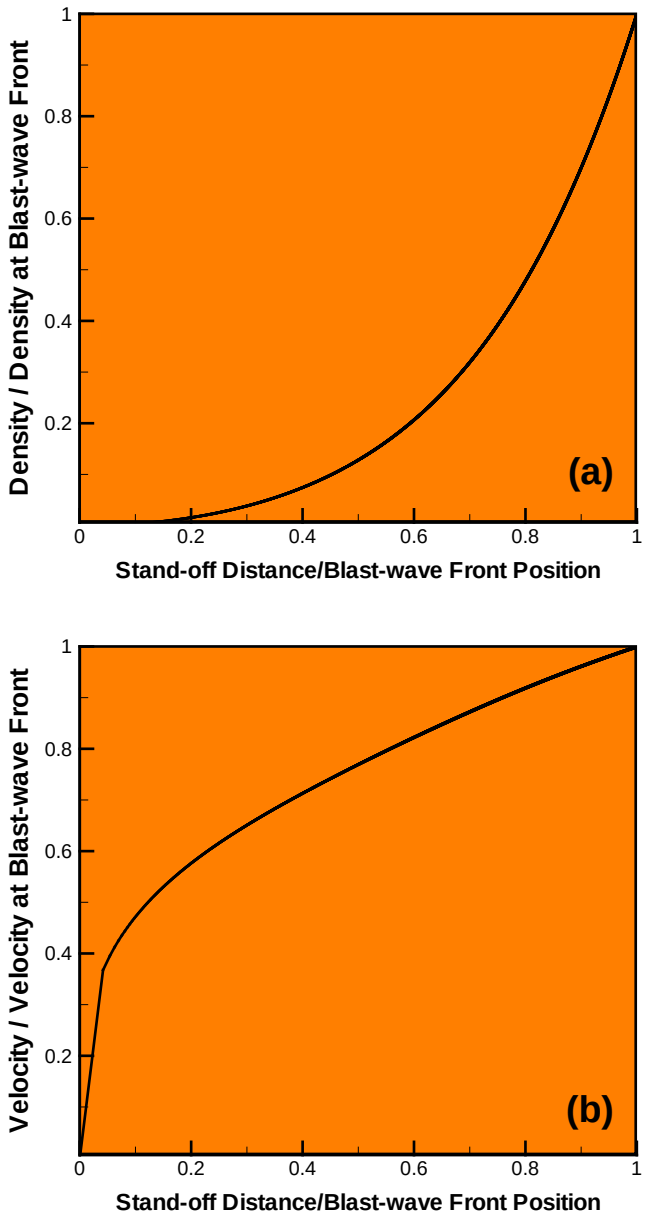

Figure 2–6 Point-source solution for: (a) mass density; (b) particle velocity; (c) static pressure; and (d) temperature

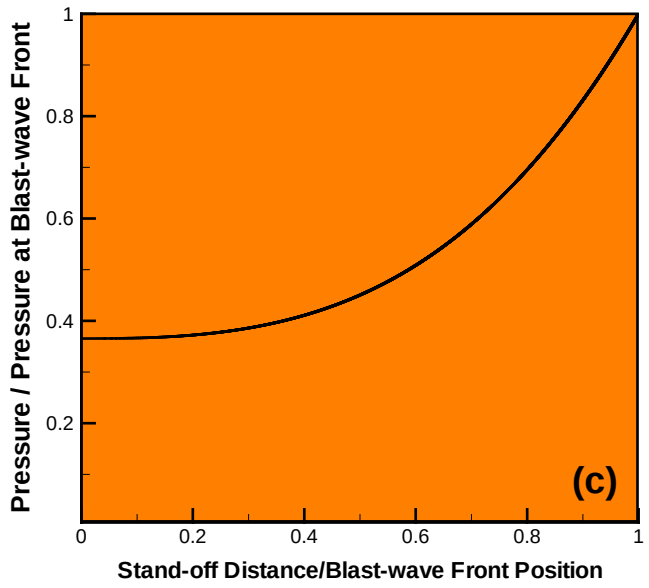

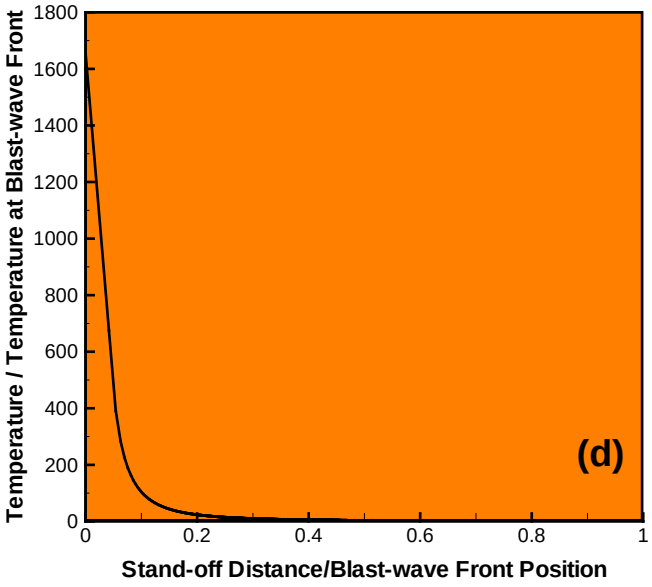

Figure 2-6. Continued.

Boundary Conditions: To account for the two-orthogonal-plane symmetry of the computational model, the appropriate symmetry (i.e., zero normal velocity) boundary conditions are applied along the flat faces (parallel to the symmetry planes) of the quarter model shown in Figure 2-5. Zero normal velocity conditions are applied also along the curved face of the channel. The use of the last boundary condition indicates that the channel walls are treated as rigid and immobile. In our future work, channel walls will be treated as deformable and, hence, an appropriate Fluid Structure Interaction (FSI) contact algorithm will be used in place of the boundary condition in question. Also, to comply with one of the basic simplifications within the theory of gas dynamics, zero-friction boundary conditions are enabled along the curved face of the computational domain. The pressure at the channel exit is maintained at the ambient pressure level (101kPa) while the inlet pressure is: (a) maintained at 3MPa, in the cases in which the main objective was validation of the employed computational methods and tools; and (b) varied in accordance with the point-source decaying-shock solution mentioned in the initial-condition section, in the computational investigations in which the main objective was establishment of the utility of the continuous-steady isentropic expansion analysis.

Fluid/Channel-wall Interactions: While the channel walls are not explicitly modeled, the nature of the velocity boundary conditions along the curved face of the quarter model described above implies that the channel walls are modeled implicitly as being rigid with zero-friction conditions along the fluid channel-wall contact surfaces. It should be noted that since the channel wall was not modeled explicitly, the thrust force exerted on to this wall cannot be directly calculated. Rather, the associated force acting on the fluid within the channel could be assessed from the difference in the exiting and the in-coming momentum of the fluid, Eq. (2-9). In addition, since no FSI effects are included at the air/channel-wall interface (i.e. the wall is not allowed to expand

outward and relieve some of the pressure acting on it), the downward thrust effects (reported later in this section) are expected to be somewhat overestimated.

Material Model: As mentioned earlier, the Eulerian domain was filled with air. Air was modeled as an ideal gas and, consequently, its equation of state was defined by the ideal-gas gamma-law relation as [13]:

$$P = (\gamma - 1)\rho E \tag{2-11}$$

where E ($=C_v T$) mass based internal energy density and C_v is the constant volume specific heat. For Eq. (2-11) to yield the standard atmospheric pressure of 101.3kPa and the standard air density of 1.19kg/m^3 at the standard temperature of 293K with γ=1.4, the corresponding mass based internal energy density has to be set to 211.5kJ/kg.

Since air is a gaseous material, it has zero shear stiffness. However, shear stresses can be developed as a result of a gradient in the flow velocity. A provision is made for viscous shear stresses in the present work while assuming a Newtonian fluid–like behavior i.e. the shear stress scales linearly with the velocity gradient with the proportionality constant, the viscosity, being set at $1.78 \cdot 10^{-5}$Pa·s.

Computational Algorithm: The governing mass, linear momentum and energy conservation and heat conduction equations are solved within ABAQUS/Explicit with a second order accurate conditionally stable explicit finite element algorithm. Within each time increment, the solution procedure for the aforementioned governing equations involves two distinct steps: (i) the Lagrangian step within which the computational domain is temporarily treated as being of a Lagrangian-type (i.e. nodes and elements are attached to and move/deform with the material); and (ii) the "***remap***" step within which the distorted mesh is mapped onto the original Eulerian mesh

and the accompanying material transport is computed and used to update the Eulerian-material states and inter-material boundaries.

Computational Accuracy, Stability and Cost: A standard mesh sensitivity analysis was carried out (the results not shown for brevity) in order to ensure that the results obtained are accurate, i.e. insensitive to the size of the elements used.

Due to the conditionally-stable nature of the explicit finite element analysis used, the maximum time increment during each computational step had to be lower than the attendant stable time increment. A typical 25ms computational analysis followed by a detailed post-processing data reduction analysis required on average 30 minutes of (wall-clock) time on a 12 core, 3.0GHz machine with 16GB of memory.

2.4.2. Results and Discussion

Continuous-steady Flow Analysis: To assess the accuracy of the Eulerian finite element analysis carried out in the present work using ABAQUS/Explicit [8], an attempt was made to reproduce the key results yielded by the continuous-steady isentropic analysis for the material-state boundary conditions specified in the previous section. Examples of the typical results obtained in this portion of the work are displayed in Figures 2-7(a)-(c).

Figure 2-7(a) shows the temporal evolution of the fluid force per inlet unit area (solid curve). This force is obtained by dividing the total fluid force (calculated as a sum, over all the Eulerian nodes, of the product of mass allotted to each node and the corresponding nodal (axial) acceleration) by the channel inlet area. In the same figure, the fluid force per unit inlet area predicted by the analytical steady isentropic expansion analysis is denoted with a dashed horizontal line. Examination of the results displayed in Figure 2-7(a) shows that the numerically predicted steady force (per unit inlet area) exerted on the fluid in the axial direction is smaller (by about 10%) than its analytical isentropic expansion counterpart.

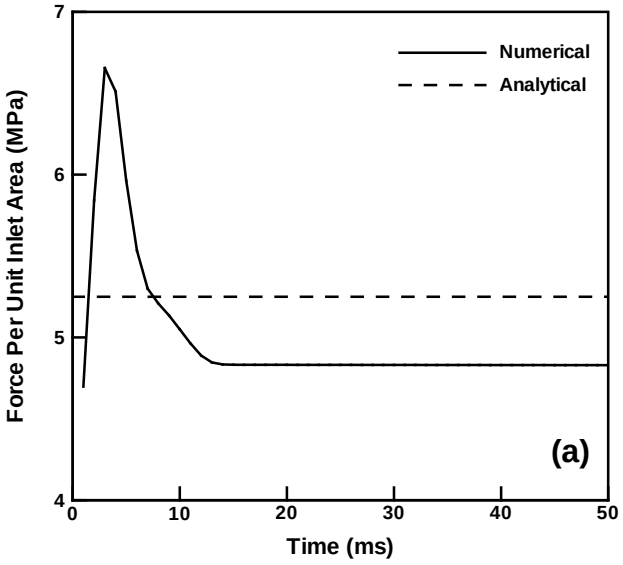

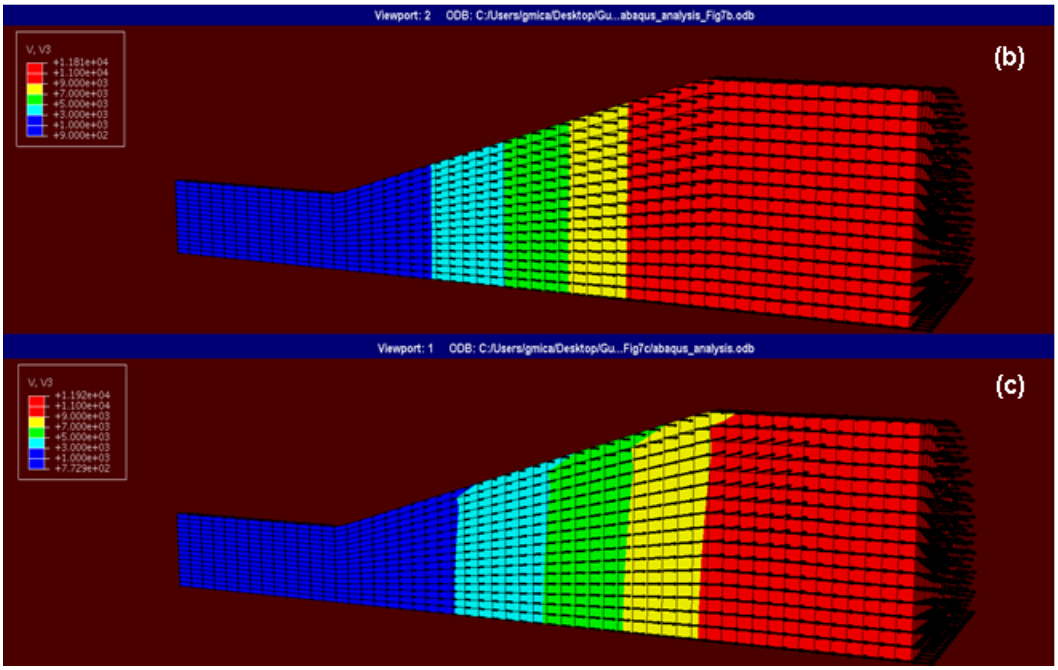

Figure 2–7 Temporal evolution of fluid force per unit area obtained using purely Eulerian computational analysis (curve) and corresponding value (dashed line) found using the isentropic expansion analysis; (b) and (c) effectively steady axial and radial fluid velocities within the channel obtained in the same computational analysis.

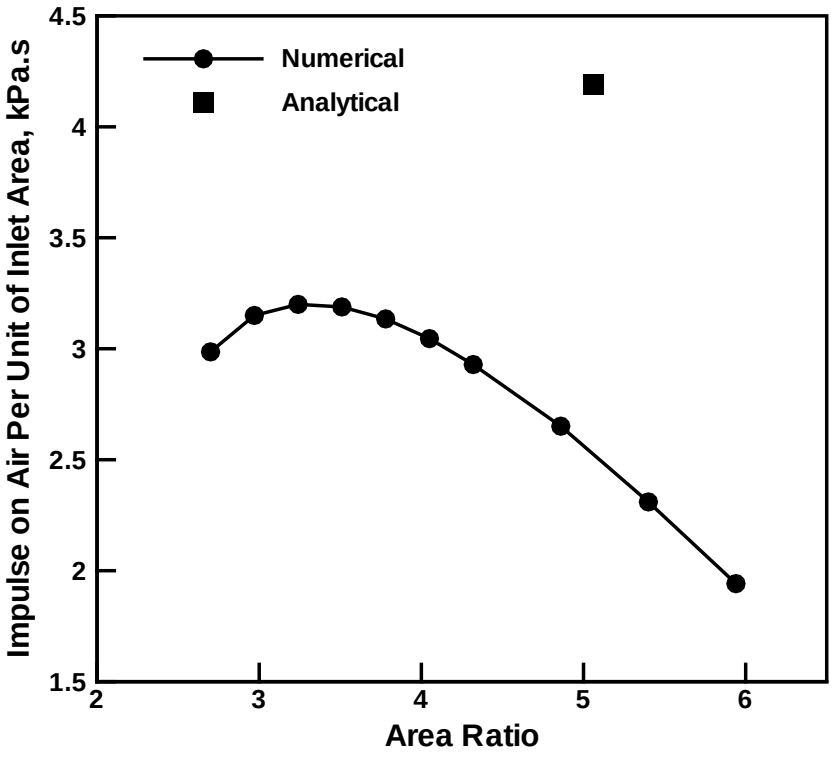

Figure 2–8 Dependence of the impulse exerted on the fluid within the channel (solid line) on the cross-sectional area ratio. The ideal area ratio and the associated impulse per unit area (based on the time-averaged inlet pressure and the same blast-loading time) are represented by a single black-color filled square symbol.

To provide a rationale for the aforementioned discrepancy between the numerical and the analytical results, flow fields through the Eulerian domain are examined and compared with their analytical counterparts. An example of this comparison is shown in Figures 2-7(b)-(c). In these figures, fluid (axial and resultant) velocities are plotted for the analytical case, Figure 2-7(b), and for the numerical case, Figure 2-7(c). The axial component of the velocity was represented using a contour plot, while arrows are used to denote (the magnitude and the orientation of) the resultant velocity. It is seen that the analytical solution assumes that the flow is entirely in the axial direction while the numerical results show that the flow contains a significant radial component (in the diverging section of the computational domain). It should be noted that the observed differences between the analytical and the numerical solutions seen in Figures 2-7(b) and (c) do not invalidate the computational procedure used but simply indicate that the flow field is not entirely axial, as postulated in the analytical steady isentropic expansion analysis.

Pulsed-transient Flow Analysis: As mentioned above, the main purpose of this portion of the work was to establish if the steady isentropic expansion analysis can be used, in place of a pulsed-transient flow analysis, to determine the optimum area ratio which maximizes the downward thrust on the SBS. An example of the results obtained in this portion of the work is displayed in Figure 2-8 in which the effect of the varying channel cross-sectional area ratio on the (axial) impulse exerted onto the fluid within the channel is displayed. A single black-color filled square symbol is used, in the same figure, to denote the optimal area ratio and the associated impulse per unit area as predicted by the analytical steady isentropic expansion analysis (based on the time-averaged inlet pressure and the same blast-loading time). Examination of the results displayed in Figure 2-8 shows that the optimal area ratio predicted by the present numerical procedure (ca. 3.24) is approximately 36% smaller than its analytical counterpart (ca. 5.06). In addition, the numerically predicted maximum value of the impulse per unit area is substantially lower than its

analytical counterpart. These differences between the numerical and the analytical results are quite large and are in sharp contrast with the findings of Owens and Hansen [6] and suggest that the use of the analytical isentropic expansion analysis in predicting the optimum area ratio of a channel may not be very reliable under blast-loading conditions.

2.5. Two-Dimensional Mine Blast Fluid-Structure Interaction Analysis

In the previous section, a purely Eulerian computational analysis is carried out to study the detonation products flow through a prototypical side channel. In that case, detonation of a mine buried in soil/sand and the accompanying expulsion of the gaseous detonation products, soil ejecta and mine casing fragments was not explicitly modeled. Instead, mine blast was assumed to merely generate high-pressure, high-density supersonic velocity gaseous detonation products which are vented through the side channels. Clearly, such analysis is over simplified and one might question its utility relative to assessing the blast mitigation potential of a new concept. To overcome these shortcomings of the aforementioned analysis, in this section, a combined Eulerian/Lagrangian finite element analysis of a prototypical buried-mine detonation event is carried out. In this analysis, mine detonation products, soil as well as the target structure equipped with the blast mitigation side channels are all modeled explicitly. Since the computational cost of a fully three-dimensional investigation is quite high and not fully justified at the concept validation stage analyzed in the present work, a simpler, computationally more efficient two dimensional analysis is first utilized. A more complete three-dimensional analysis of the same problem will be presented in the next section.

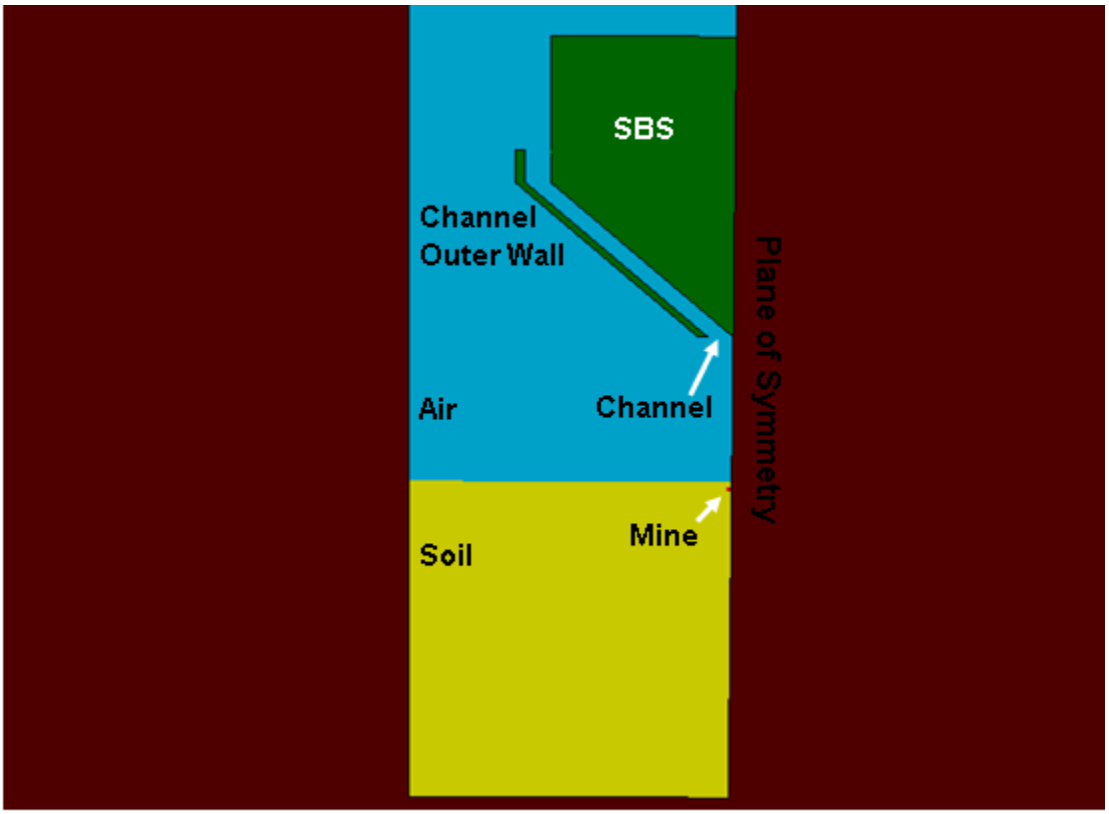

Figure 2–9 A prototypical computational domain used in the two-dimensional transient finite element analysis of the mine blast detonation event: SBS-Surrogate Box Structure.

2.5.1. Computational Procedure

A brief description regarding the computational model and the numerical procedure used in this portion of the work is described below.

Computational Domain: The computational domain used consists of two separate sub-domains, one of an Eulerian-type and the other of a Lagrangian-type, Figure 2-9. The Eulerian sub-domain (used to model sand/soil, mine/detonation products and the ambient air) is of a parallelepiped shape. This sub-domain is typically discretized using hexahedral first order reduced integration Eulerian elements. Due to the aforementioned two-dimensional nature of the model, the mesh shown in Figure 2-9 extends only one element in the direction normal to the figure. Also, it should be noted that due to the inherent symmetry of the problem, only one-half of the computational model is explicitly analyzed.

As far as the Lagrangian sub-domain is concerned, it contains three hexahedron first order, reduced integration Lagrangian elements. One of the elements represents the cabin combined with the V-shaped hull. The other two elements define the inclined and the vertical segments of the side channel outer wall. The three Lagrangian elements are rigidized and grouped into a single rigid body. During the channel-geometry optimization, both the width of the channel and the exit cross-sectional area are varied. The width of the channel was varied by displacing the inclined and the vertical segments in the horizontal direction. The exit cross-sectional area is varied by changing the length of the inclined segment at its upper end.

Computational Analysis-type: The mine blast event is analyzed computationally using a Combined Eulerian Lagrangian and a fully-coupled thermo-mechanical finite-element algorithm. Within the Lagrangian sub-domain of the model, the mesh is attached to the underlying material and moves and deforms with it. While within the Eulerian sub-domain, the mesh is stationary and different (Eulerian) material are allowed to move through it. Heat dissipation associated with

plastic deformation (of soil) is treated as a heat-source in the governing thermal equation. On the other hand, the effect of temperature on the mechanical response of the attendant materials is taken into account through the use of temperature-dependent material properties.

Initial Conditions: The Eulerian sub-domain is initially filled with soil/sand, mine and the ambient air (by prescribing the corresponding material volume fractions), all at their respective standard state conditions. The Lagrangian sub-domain is assumed to be initially stationary.

Boundary Conditions: To account for the planar symmetry of the problem, the appropriate zero normal velocity boundary conditions are applied along the symmetry plane. The Eulerian boundaries associated with the soil are given non-reflecting out flow boundary conditions to prevent unphysical reflection of the shock at these boundaries. On the other hand, the Eulerian boundaries associated with the air are given no inflow and free outflow boundary conditions. Instead of fixing it fully in space, the Lagrangian portion of the model is allowed to move, but only in the vertical direction. This approach enabled capturing of the aforementioned FSI effects.

Euler-Lagrange Contact Conditions: Since the Eulerian and Lagrangian domains do not possess conformal meshes, the contact interfaces between the two could not be defined using mesh-based surfaces. Instead, contact interfaces between the Lagrangian and the Eulerian sub-domains are determined using the so-called "***immersed boundary method***" [8] which identifies, during each computational time increment, the boundary of the Eulerian sub-domain region which is occupied by the Lagrangian sub-domain. Eulerian-Lagrangian contact constraints are enforced using a penalty method, within which the extent of contact pressure is governed by the local surface penetrations (where the default penalty stiffness parameter is automatically maximized subject to stability limits). As far as the shear stresses are concerned they are transferred via a "***slip/stick***" algorithm, that is shear stresses lower than the frictional shear stress are transferred without interface sliding (otherwise interface sliding takes place). The frictional shear stress is defined by

a modified Coulomb law within which there is an upper limit to this quantity (set equal to the shear strength of the Lagrange sub-domain material). The frictional shear stress is then defined as a smaller of the product between the static/kinetic friction coefficient and the contact pressure, on one hand, and the Lagrangian sub-domain material shear strength, on the other. It should be recalled that the Lagrangian portion of the model is rigidized so that the shear strength is effectively made infinitely large.

In addition to the Eulerian-Lagrangian contacts, interactions (of a "***sticky***" character) also occur between different Eulerian materials. This type of interactions is a consequence of the kinematic constraint which requires that all Eulerian materials residing in a single Eulerian element are subjected to the same strain. The Eulerian-Eulerian contacts allow normal (tensile and compressive) stresses to be transferred between adjoining materials while no slip at the associated material boundaries is allowed.

Material Model(s): As mentioned earlier, the Eulerian domain was filled with air, mine and the soil. Also, the Lagrangian portion of the model is rigidized. A material model for air was presented in the previous section. The Lagrangian (rigid) material is fully defined by its density. Hence, in this section material models for the remaining two materials, mine/C4 high-energy explosive and soil, is presented.

Material models typically define the relationships between the flow variables (pressure, mass-density, energy-density, temperature, etc.) in a computational analysis. These relations typically involve: (a) an equation of state; (b) a strength equation and (c) a failure equation for each constituent material. These equations arise from the fact that, in general, the total stress tensor can be decomposed into a sum of a hydrostatic stress (pressure) tensor (which causes a change in the volume/density of the material) and a deviatoric stress tensor (which is responsible for the shape change of the material). An equation of state then is used to define the

corresponding functional relationship between pressure, mass density and internal energy density (temperature). Likewise, a (constitutive material) strength relation is used to define the appropriate equivalent plastic strain, equivalent plastic strain rate, and temperature dependencies of the material's yield strength. This relation, in conjunction with the appropriate yield-criterion and flow-rule relations, is used to compute the deviatoric part of stress under elastic-plastic loading conditions. In addition, a material model generally includes a failure criterion, (i.e. an equation describing the hydrostatic or deviatoric stress and/or strain condition(s) which, when attained, cause the material to fracture and lose its ability to support (abruptly in the case of brittle materials or gradually in the case of ductile materials) normal and shear stresses. Such failure criterion in combination with the corresponding material-property degradation and the flow-rule relations governs the evolution of stress during failure**.**

Mine/C4 High-energy Explosive: To model the hydrodynamic response of C4 high-energy (HE) explosive, both the ideal gas and the Jones-Wilkins-Lee (JWL) [13] EOS relations are used (in separate analyses). These two types of EOS are the preferred choice for the equation of state for high-energy explosives in most hydrodynamic calculations involving detonation. The results obtained for the two EOS models are found to be qualitatively and quantitatively quite similar and, hence, only the results obtained using the JWL EOS for the C4HE are presented in this section.

The JWL equation of state is defined as [13]:

$$P = A\left(1-\frac{w}{R_1 v}\right)e^{-R_1 v} + B_1\left(1-\frac{w}{R_2 v}\right)e^{-R_2 v} + \frac{wE}{v} \qquad (12)$$

where the constants A, R_1, B_1, R_2 and w for the C4 high-energy explosive are can be found in the AUTODYN materials library [13] and v is the specific volume of the material. Within a typical hydrodynamic analysis, detonation is modeled as an instantaneous process which converts

unreacted explosive into gaseous detonation products and detonation of the entire high-explosive material is typically completed at the very beginning of a given simulation. Consequently, no strength and failure models are required for high-energy explosives such as C4.

Soil: Soil is a very complicated material whose properties vary greatly with the presence/absence and relative amounts of various constituent materials (sand particles, clay, silt, gravel, etc.), and particle sizes and particle size distribution of the materials. In addition, the moisture content and the extent of pre-compaction can profoundly affect soil properties. To account for all these effects, Clemson University and the Army Research Laboratory (ARL), Aberdeen, Proving Ground, MD jointly developed [14] and subsequently parameterized (using the results of a detailed investigation of dynamic response of soil at different saturation levels, as carried out by researchers at the Cavendish Laboratory, Cambridge, UK [15, 16]) the new soil model [14, 17-20]. This model (used in the present work) is capable of capturing the effect of moisture on the dynamic behavior of soil and was named the CU-ARL soil model. In the remainder of this section, a brief qualitative description is provided of this material model. In addition, in Appendix A, key functional relations constituting this model are presented and explained.

For the CU-ARL soil model, a saturation-dependent porous-material/compaction equation of state is used which, as shown in our previous work [17] is a particular form of the Mie-Gruneisen equation of state [13]. Within this equation, separate pressure vs. density relations are defined for plastic compaction (gives rise to the densification of soil) and for unloading or elastic-reloading. Within the CU-ARL soil strength model, the yield strength is assumed to be pressure dependent and to be controlled by saturation-dependent inter-particle friction. In addition to specifying the yield stress vs. pressure relationship, the strength model entails the knowledge of the density and saturation dependent shear modulus. Within the CU-ARL soil failure model, failure is assumed to occur when the negative pressure falls below a critical saturation-dependent

value, i.e. a "***hydro***" type failure mechanism was adopted. After failure, the failed material element loses the ability to support tensile or shear loads while its ability to support compressive loads is retained.

Mine Detonation: The mine is detonated at time equal to zero, over its entire bottom face. The detonation of the remainder of the mine and the associated release of the explosive energy are then governed by the arrival of a planar detonation front, moving at a constant speed.

Computational Algorithm: The governing mass, linear momentum, energy conservation and heat conduction equations are solved within ABAQUS/Explicit with a second order accurate conditionally stable explicit finite element algorithm. The same computational algorithm, as the one described and used in the previous section, was employed in this portion of the work.

Computational Accuracy, Stability and Cost: A standard mesh sensitivity analysis was carried out (the results not shown for brevity) in order to ensure that the results obtained are accurate, i.e. insensitive to the size of the elements used.

As in the previous analysis, due to the conditionally-stable nature of the explicit finite element analysis used, the maximum time increment during each computational step had to be lower than the attendant stable time increment. A typical 10ms computational analysis followed by a detailed post-processing data reduction analysis required on average 30 minutes of (wall-clock) time on a 12 core, 3.0GHz machine with 16GB of memory.

2.5.2. Results and Discussion

Examples of typical results obtained in this portion of the work are displayed in Figures 2-10(a)-(b). In Figure 2-10(a), percent reduction (relative to the SBS case without side channel) in the total blast momentum resulting from the use of the side vent channel is plotted as a function of channel width, at two different exit-to-inlet cross-sectional area ratios of the channel and a constant value (0.03m) of the charge Depth Of Burial (DOB). The results displayed in this figure

show that: (a) the downward thrust is capable of reducing the blast momentum transferred to the SBS; (b) the effect is, however, quite small (maximum around 4%); (c) the case associated with the larger area ratio yields slightly higher percent momentum reduction; (d) at each of the cross-sectional area ratios considered, there appears to be a range of channel widths which yield maximum momentum reduction effects; and (e) at very small lower channel widths, the presence of the side channels could be detrimental since it increases the blast momentum transferred to the SBS.

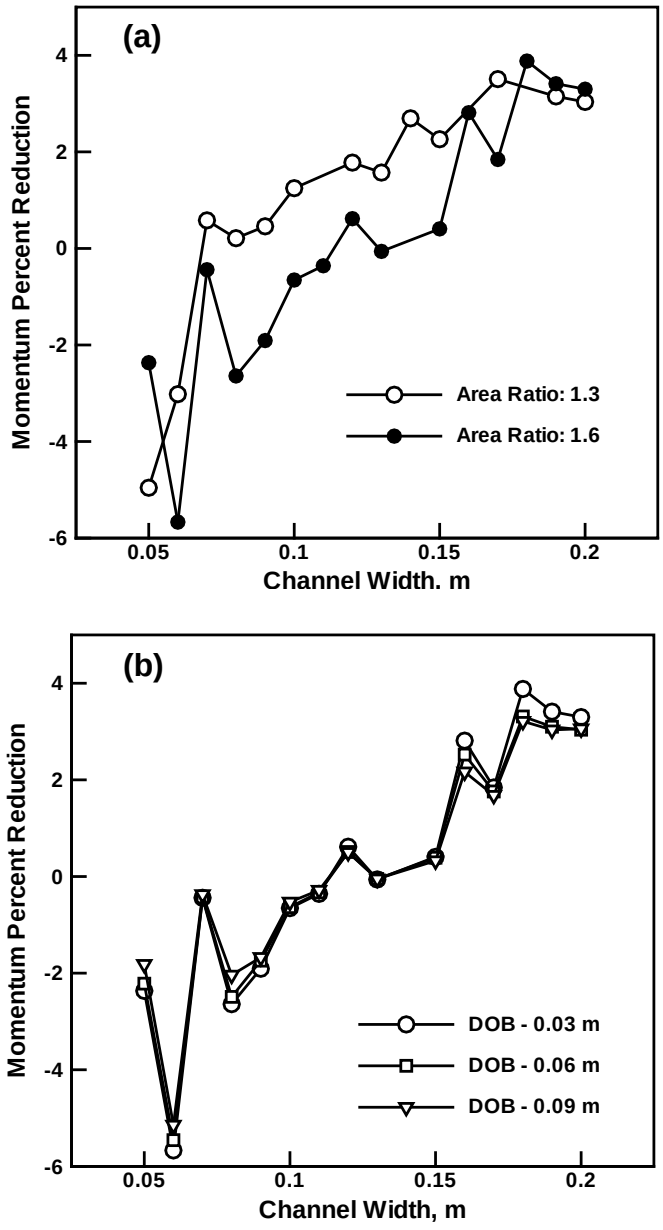

Figure 2–10 Two-dimensional fluid-structure interaction results pertaining to: (a) the effect of the channel width and the tube exit-to-inlet area ratio on the percent reduction in the blast momentum transferred to the SBS, at a constant depth of burial of 0.03m; and (b) the effect of the channel width and depth of burial on the same percent momentum reduction, at a constant tube exit-to-inlet area ratio of 1.6.

The results displayed in Figure 2-10(b) show the effect of channel width on the percent reduction in the total blast momentum at three different (0.03m, 0.06m and 0.09m) explosive-charge DOBs and at a constant value (1.6) of the exit-to-inlet cross-sectional area ratio of the channel. The results presented in this figure show that the beneficial effect of the channel is still present (but, somewhat lower) in the case of larger DOBs. These results are consistent with the fact that, as the DOB increases, larger fraction of the soil is present in the fluid passing through the channel. This in turn, reduces the extent of air-based isentropic expansion effects responsible for the observed momentum reduction.

2.6 Three-Dimensional Mine Blast Fluid-Structure Interaction Analysis

In the previous section, a two-dimensional fluid structure interaction analysis was carried out in order to assess the potential of the side channels in lowering the blast momentum transferred to the SBS through the downward thrust effects. The results obtained revealed the beneficial effects of the side channels but the magnitude of these effects was quite small. Since the analysis presented in the previous section does not consider the role of all three-dimensional effects, a more complete three-dimensional analysis of the mine blast and the associated fluid structure interactions is presented in this section.

2.6.1. Computational Procedure

The computational procedure used in this portion of the work is almost identical to the one employed in the previous section. Hence, details regarding this procedure will not be repeated here. Instead, only the aspects of the analysis which differ from their counterparts presented in the previous section will be overviewed.

Computational Domain: The computational domain used again consists of two separate sub-domains, one of an Eulerian-type and the other of a Lagrangian-type, Figure 2-11. The Eulerian sub-domain is again filled with sand/soil, mine/detonation products and the ambient air and is of a parallelepiped shape. This sub-domain is discretized using hexahedral first order reduced integration Eulerian elements. It should be noted that due to the inherent symmetry of the problem, only one-quarter of the computational model is explicitly analyzed.

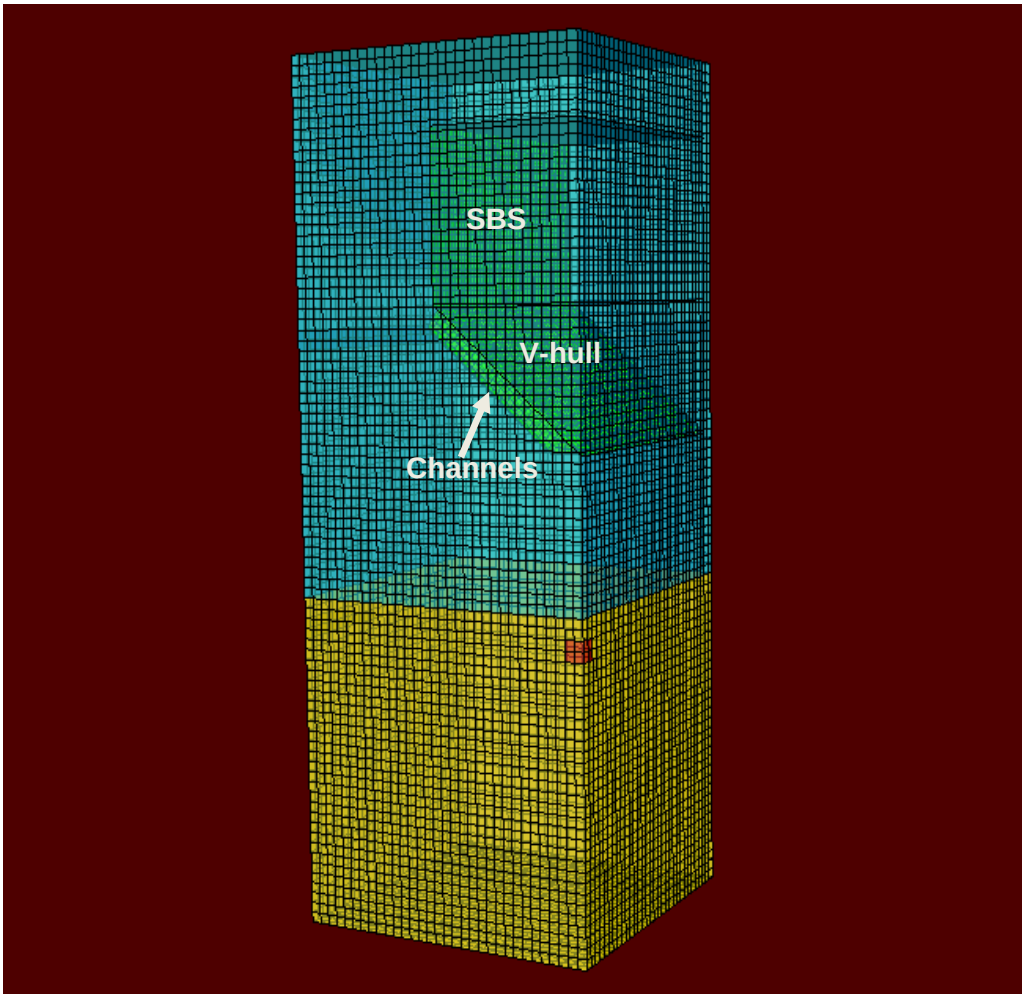

Figure 2–11 A prototypical computational domain used in the three-dimensional transient finite element analysis of the mine blast detonation event: SBS-Surrogate Box Structure.

As far as the Lagrangian sub-domain is concerned, it consists of the SBS, V-hull and side channels. The Lagrangian sub-domain is meshed using quadrilateral shell elements and rigidized to form a single rigid body. During the channel-geometry optimization, the channel inlet cross-sectional area and the outlet-to-inlet area ratio are varied.

Computational Accuracy, Stability and Cost: A standard mesh sensitivity analysis was again carried out (the results not shown for brevity) in order to ensure that the results obtained are accurate, i.e. insensitive to the size of the elements used. A typical 10ms computational analysis followed by a detailed post-processing data reduction analysis required on average 60 minutes of (wall-clock) time on a 12 core, 3.0GHz machine with 16GB of memory.

2.6.2. Results and Discussion

In order to assess the full blast-mitigation potential of the proposed venting system, and to shed additional light onto the blast-chimney concept, several distinct SBS configurations were examined. The main among these configurations are shown in Figures 2-12(a)-(d). The SBS configuration shown in Figure 2-12(a) has no side vent-channels (or the vertical "through-the-cabin" vent channel). The SBS configuration shown in Figure 2-12(b) contains constant-radius side vent-channels (but no vertical "through-the-cabin" vent channel). The SBS configuration shown in Figure 2-12(c) is very similar to that shown in Figure 2-12(b) except for the flaring of the side vent-channels (in their exit section). The SBS configuration shown in Figure 2-12(d) has the same side-vent channel configuration as that shown in Figure 2-12(c), but, in addition, also contains a vertical vent channel. The basic configuration analyzed in the present work is that shown in Figure 2-12(c) and configuration shown in Figures 2-12(a)-(b) enable respectively assessment of the blast-mitigation effects arising from the presence and from flaring of the side-vent channel. Configuration shown in Figure 2-12(d) on the other hand, enabled assessment of the blast-venting role of the "blast chimney" (as utilized in the HMMWV).

The computational analyses carried out in this portion of the work yielded the results pertaining to the temporal evolution and spatial distribution of various field quantities such as material-particle velocities, Euler-materials volume fraction, pressure, density, etc. In addition, results pertaining to the explosive-charge detonation-induced loading experienced by and the subsequent response of the SBS structure (modeled as a rigid body) were obtained. In the remainder of this section, few prototypical results are presented and discussed.

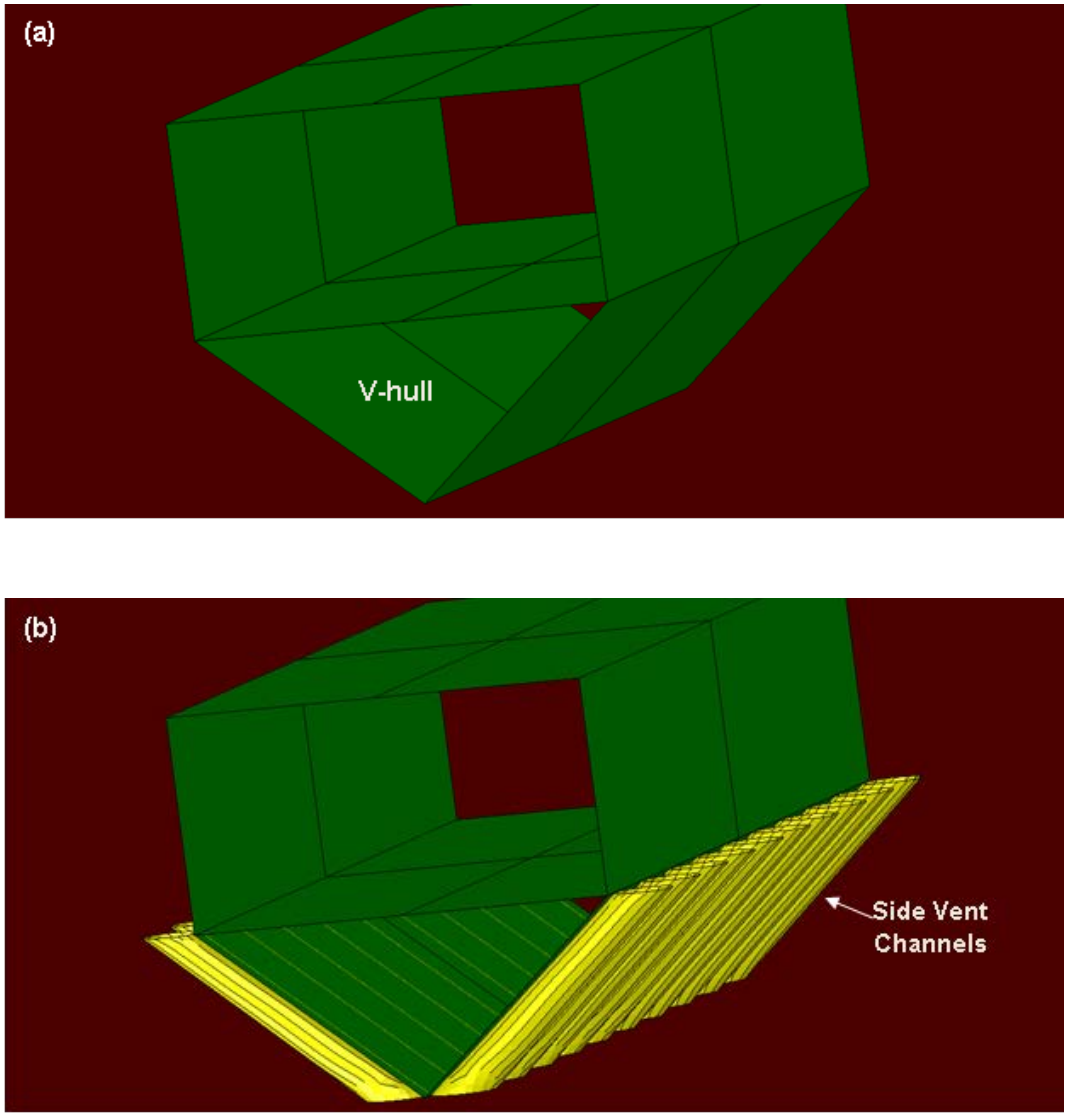

Figure 2–12 Main SBS configurations analyzed in the present work: (a) the baseline v-hull configuration; (b) same as (a), but with constant-radius side vent channels; (c) same as (b), but with channel flaring; and (d) same as (c), but with a vertical vent channel.

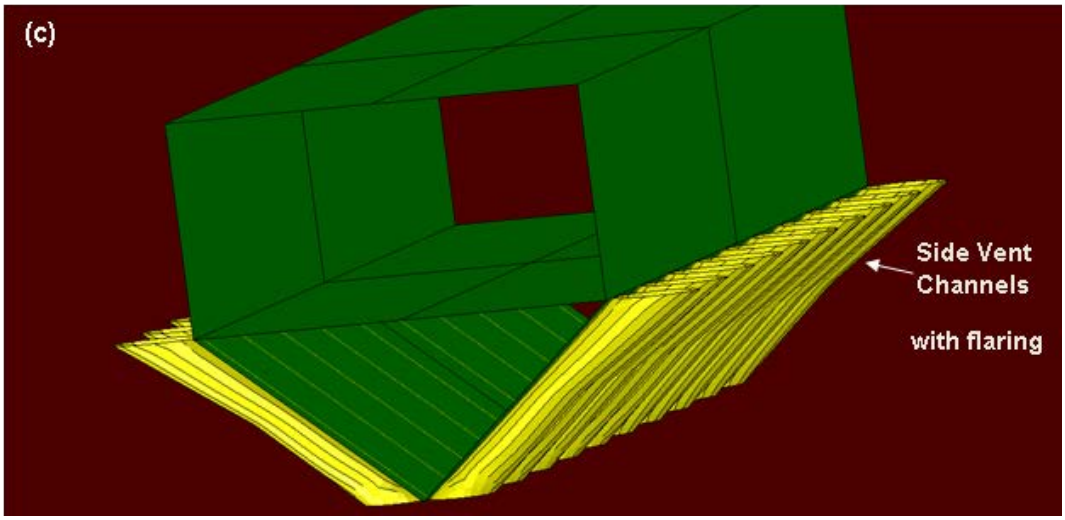

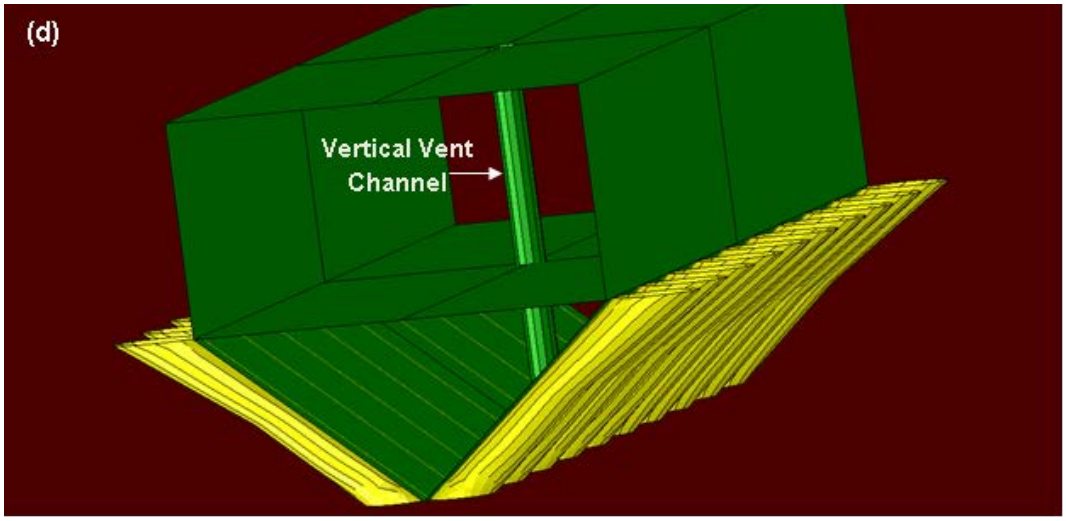

Figure 2-12. Continued.

A comparison of the prototypical Eulerian-domain total-velocity results for (a) the SBS configuration without channels; (b) the SBS configuration with constant cross-section channels; (c) the SBS configuration with flared channels; and (d) the SBS configuration with flared channels and a vertical blast-chimney is shown in Figures 2-13(a)-(d), respectively. In these figures, the outline of the SBS structure is denoted using heavy solid black lines. In the same figures, arrows are used to show the projected direction (onto the display/projection planes) of the total-velocity vector while contours are used to denote the magnitude of the total-velocity vector. Examination of the results displayed in Figures 2-13(a)-(d) reveals that: (a) the presence of side-vent channels helps guide the flow of the gaseous detonation products, soil-ejecta and air along the direction parallel with the side of the V-Hull. Specifically, in the no side-vent channel case, Figure 2-13(a), there is plenty of evidence of the impact and reflection of the gaseous detonation products, soil-ejecta and air from the V-Hull side. Consequently, one would expect (and the computational results confirmed) that the largest amount of momentum is transferred to the SBS, in the absence of side-vent channels; (b) flow of the Eulerian material through the side-vent channel is seen to result in an increase in the material-particle velocity, the phenomenon which is particularly pronounced in the flared-section of the side-vent channels, Figure 2-13(c). This phenomenon, as discussed earlier in this manuscript, leads to the development of a downward thrust to the side-vent channels and, in turn, to the SBS; (c) the presence of the blast-chimney promotes venting of gaseous detonation products, soil-ejecta and air; and (d) when analyzing the results displayed in Figures 2-13(a)-(d), it should be recalled that the arrows represent only the projection of the total-velocity vector onto the displayed plane while the contours pertain to the total-velocity vector overall magnitude. In other words, the fact that there are fewer and shorter arrows in Figure 2-13(a) relative to that in Figure 2-13(c) indicates that a substantial component of the flow takes place in a direction normal to the display plane. This observation re-emphasizes

the previously made point regarding the role of side-vent channels in guiding the flow in a direction parallel with the v-hull side.

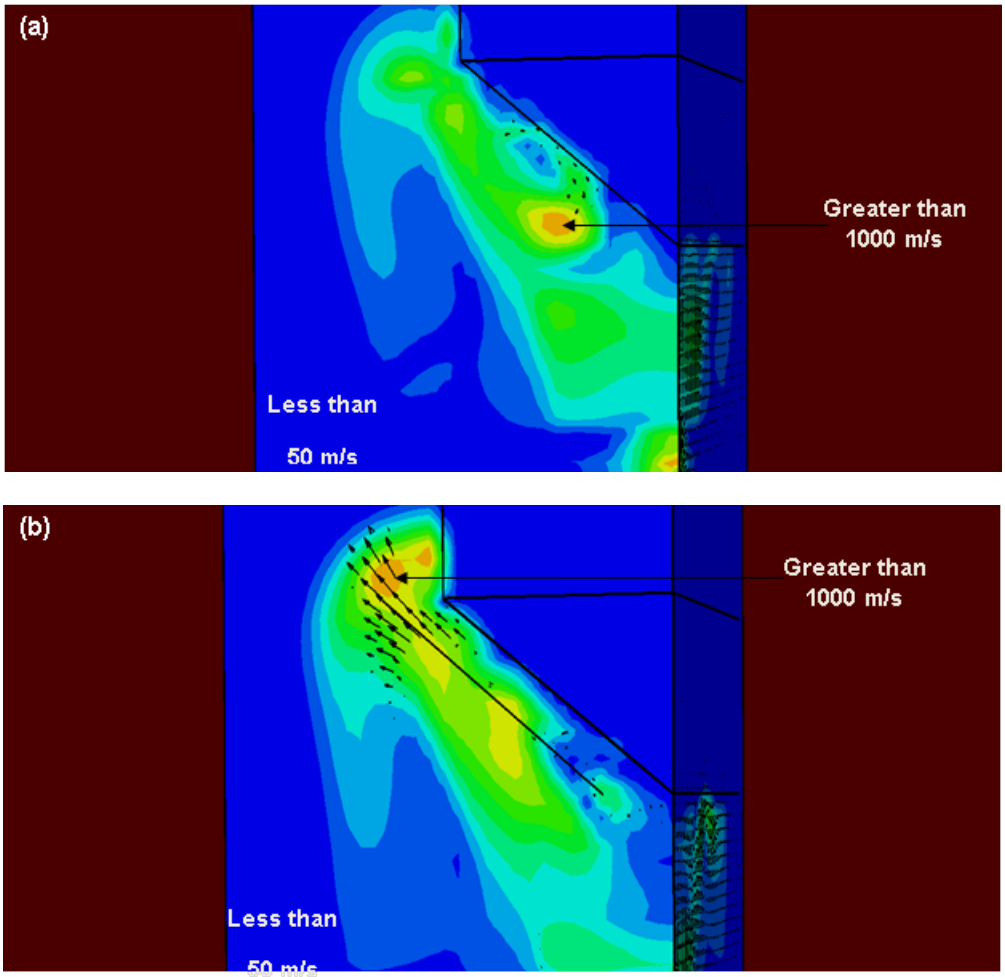

Figure 2–13 A comparison of the typical flow-field (velocity magnitude, in the present case) results for (a) the SBS configuration without channels; (b) the SBS configuration with constant cross-section channels; (c) the SBS configuration with channel flaring; and (d) like (c) but with a vertical-vent channel.

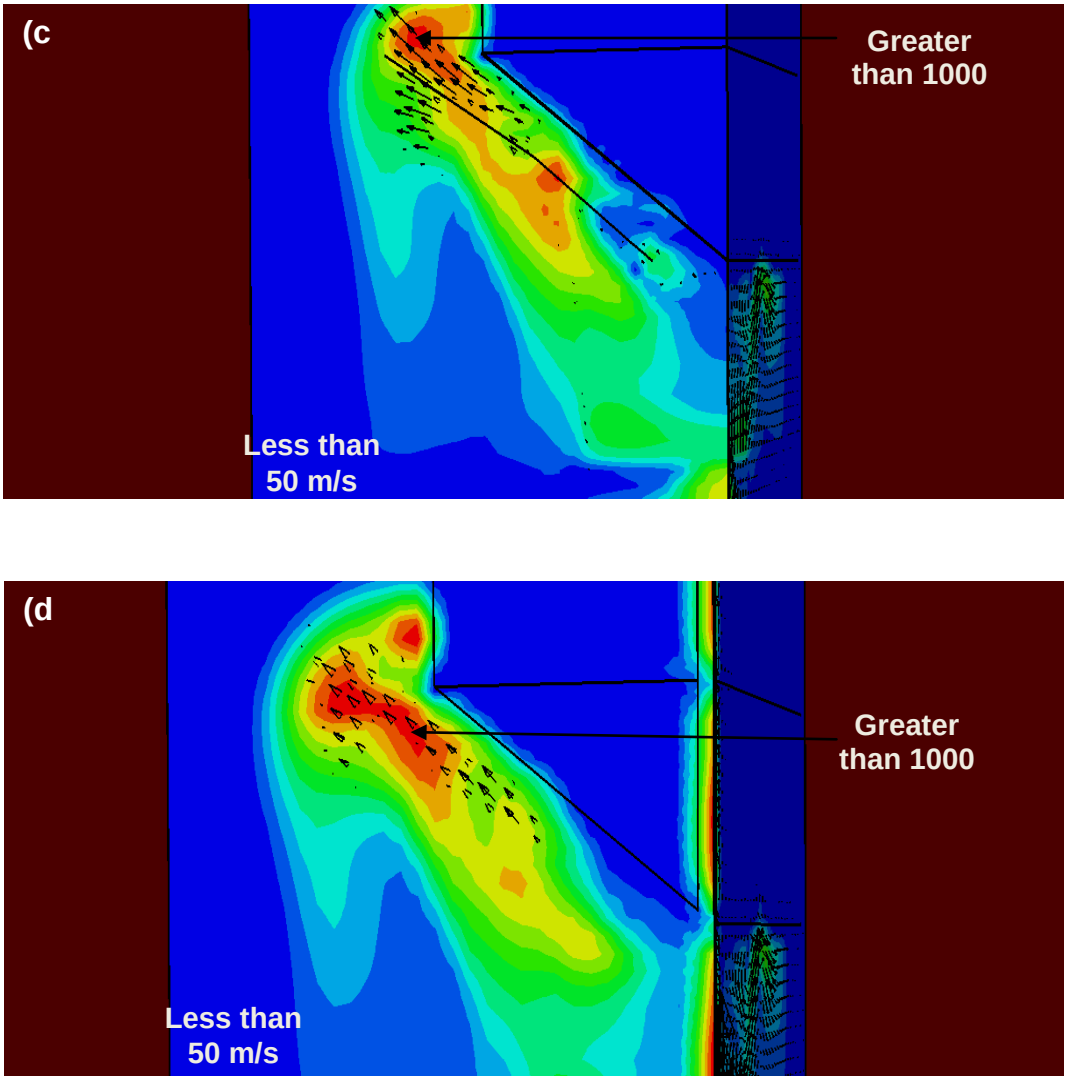

Figure 2-13. Continued.

Spatial distributions of the soil-material volume fraction at four (0μs, 20μs, 40μs and 60μs) post-detonation times within a vertical section passing through the axis of one of the flared side-vent channels are shown in Figures 2-14(a)-(d), respectively. In these figures, the Eulerian material with a high volume fraction of soil is represented in red, while the soil-free Eulerian material is displayed in blue. Examination of the results displayed in these figures clearly confirms the previously mentioned role of the side-vent channels in guiding the detonation products, soil-ejecta and air along the v-hull side. Specifically, in Figure 2-14(a), a well-defined planar interface is observed between the soil and the air. In Figure 2-14(b), it is seen that the ejected soil has reached the side-vent channel inlet. The soil (along with the detonation products) then enters the side-vent channel, travels through it and reaches the channel exit at the post-detonation time corresponding to Figure 2-14(c). Subsequently, as shown in Figure 2-14(d), the soil which has exited the channel flows upwards (parallel with the vertical side of the SBS cabin).

Examples of the typical results obtained in this portion of the work, which relate to the assessment of the blast-mitigation potential offered by the proposed side vent-channel concept are displayed in Figures 2-15(a)-(c). These results are discussed below.

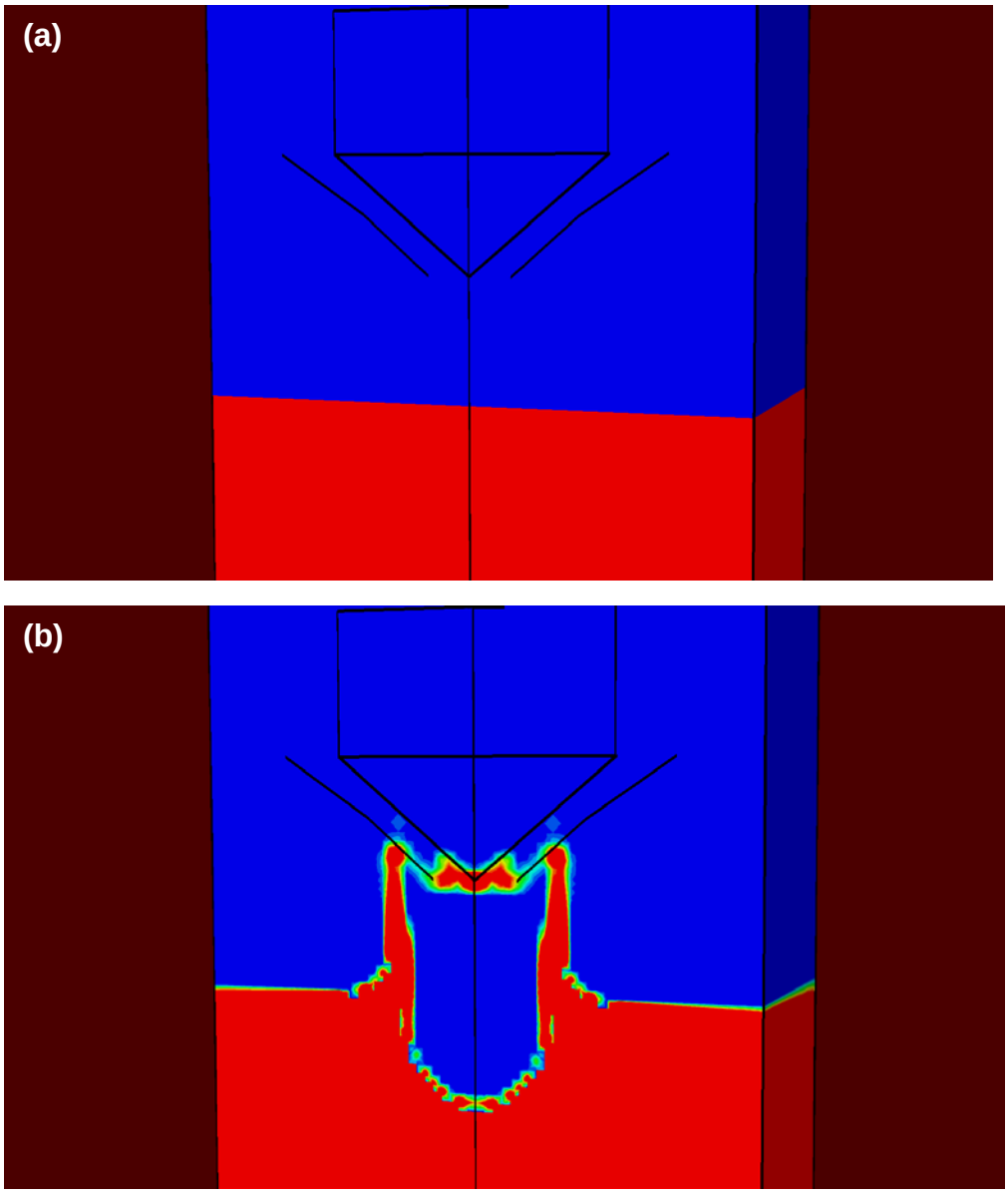

Figure 2–14 Spatial distributions of the soil-material volume fraction at: (a) 0μs; (b) 20μs; (c) 40μs and (d) 60μs post-detonation times within a vertical section passing through the axis of one of the flared side-vent channels.

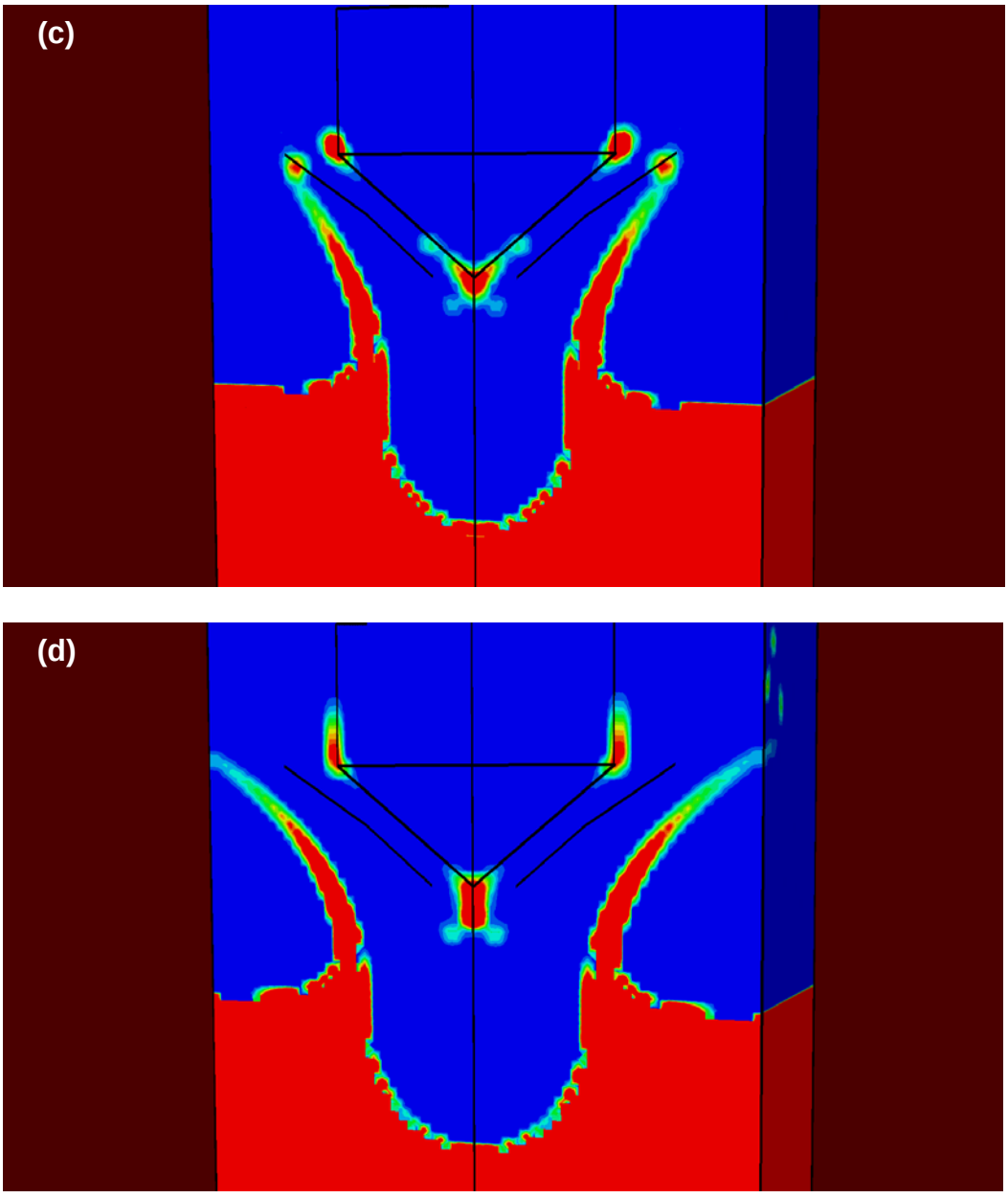

Figure 2-14. Continued.

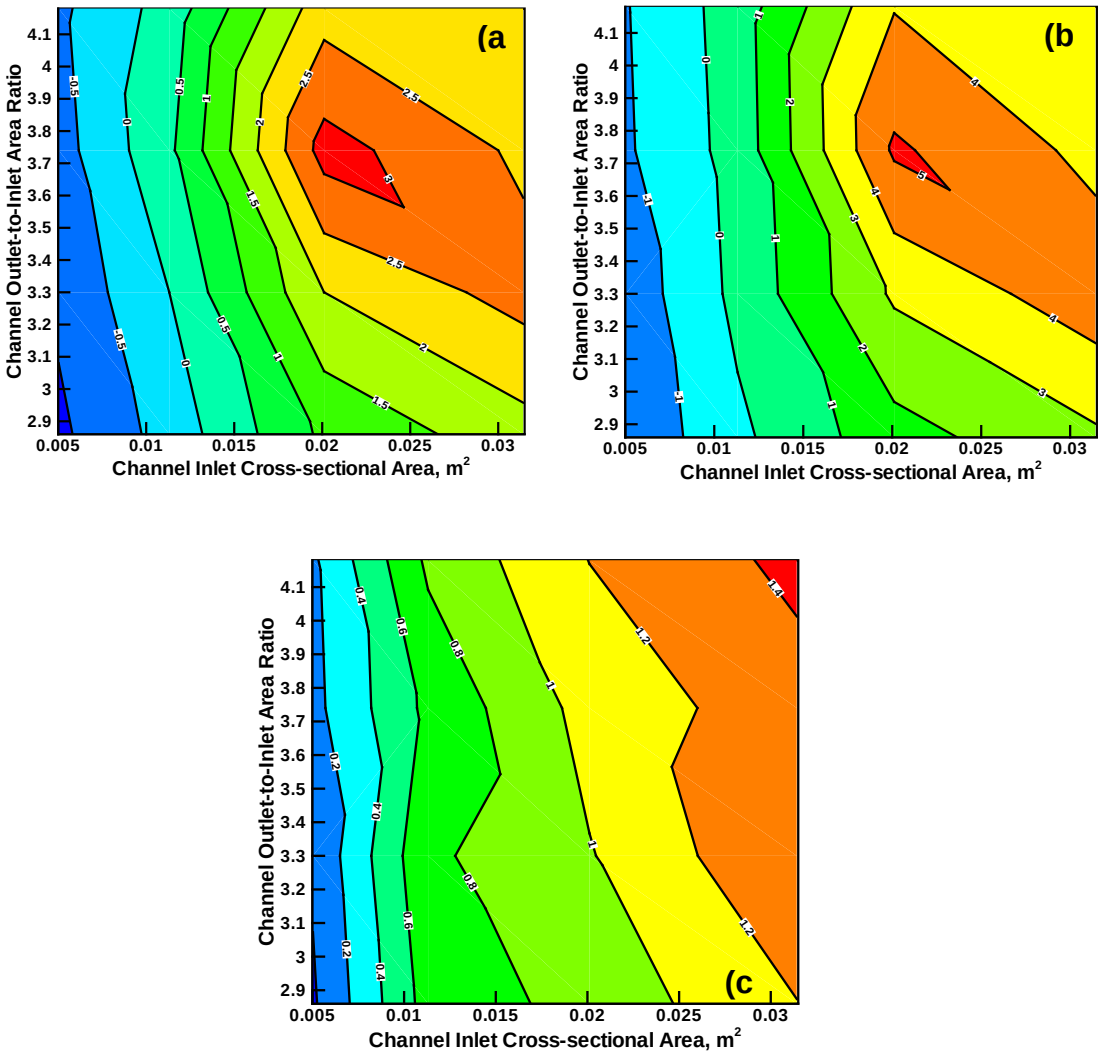

Figure 2–15 Percent reduction (relative to the SBS case without side-vent channels) in: (a) total blast momentum; (b) the maximum kinetic energy acquired by the SBS; and (c) the maximum SBS acceleration as a function of channel inlet-area and inlet-to-outlet area ratio.

In Figure 2-15(a), the total transferred-momentum percent reduction (relative to the SBS case without side channels) resulting from the use of side vent-channels is plotted as a function of channel inlet-area and inlet-to-outlet area ratio. The results displayed in this figure show that there is a region in the channel inlet area/channel outlet-to-inlet area ratio design space which is associated with reductions in the blast momentum transferred to the SBS. However, these reductions are even smaller (maximum 3.1%) than the ones found in the two-dimensional analysis (reported in Section IV). It should be noted that the SBS mass is not constant within the design space but increases both with the channel inlet area and outlet-to-inlet area ratio. In the portion of the design space in which the transmitted impulse takes on the lowest values, the SBS mass is ca. 1.8 % larger than that of the SBS without side channels.

In Figure 2-15(b), the percent reduction in maximum kinetic energy acquired by the SBS (relative to the SBS case without side channels) resulting from the use of side vent-channels is plotted as a function of channel inlet-area and inlet-to-outlet area ratio. The results displayed in this figure show that there is a region in the channel inlet area/channel outlet-to-inlet area ratio design space which is associated with ca. 5 % reductions in the kinetic energy acquired by the SBS. This region of the design space nearly coincides with the one identified in Figure 2-15(a) in which maximum reductions in the transmitted impulse were observed.

In Figure 2-15(c), the percent reduction in the maximum acceleration acquired by the SBS (relative to the SBS case without side channels) resulting from the use of side vent-channels is plotted as a function of channel inlet-area and inlet-to-outlet area ratio. The results displayed in this figure show that the largest reduction in the maximum SBS acceleration is obtained in the portion of the design space in which both the channel inlet area and channel outlet-to-inlet area ratio acquire the largest values. In this region, the SBS mass also acquires the largest values. The results displayed in Figure 2-15(c) are consistent with the fact that the SBS acquires a maximum

acceleration during the earlier stages of the blast/SBS interaction when the downward thrust affects are minimal or not present. Under such conditions, the (rigid) SBS response to the blast is dominated by the SBS mass.

It should be recalled that, in the case of the blast chimney, it has not been yet established to what extent the benefits offered by this blast-mitigation solution are the result of the blast-venting effect and to what extent they could be attributed to the downward thrust effect. To help shed some light on this problem, a series of computational analyses is carried out in the present work using a redesigned SBS with a vertical channel through it, Figure 2-12(d). These analyses also show quite small (2-3%) reduction in blast impulse due to the downward thrust effects. On the other hand, depending on the size of the vertical channel cross-sectional area, reduction in the momentum transfer to the SBS due to the venting effects could be several times higher (but still far short of the claims reported in the context of the blast chimney). It is, hence, speculated that the observed blast mitigation effects in the case of the blast chimney modified HMMWV are not solely the result of the presence of the blast chimney but that they are greatly influenced by the use of additional aforementioned blast-mitigation solutions (i.e. energy absorbing floor, shock-absorbing seats, a gunner protection system, blast-resistant doors etc.[1, 4]).

2.7. Summary and Conclusions

Based on the work presented in the manuscript, the following main summary remarks and conclusions can be drawn:

1. A new blast mitigation solution based on the use of side-vent channels/tubes attached to the v-hull is critically assessed. The solution is an extension of the recently introduced so-called "***blast chimney***" concept and is inspired by the principle of operation of the "***pulse detonation***" rocket engines.

2. Relative to the blast-chimney concept, the proposed solution offers, at least, the following three benefits: (a) it does not compromise the ease of movement within the cabin space; (b) it does not interfere with the ability of the vehicle occupants to scout their surroundings; and (c) it is not expected to, degrade the vehicle's structural durability/reliability.

3. A comprehensive series of transient nonlinear dynamics finite element fluid-structure interaction analyses under supersonic flow conditions is carried out in order to assess the blast mitigation potential of the new solution.

4. The results obtained show that the side-vent channels reduce the blast momentum by creating a downward thrust. The extent of blast momentum reduction (relative to an identical structure without side-vent channels) is ~3%. The accompanying reduction in kinetic energy acquired by the SBS is ca. 5 %, while the maximum reduction in the SBS acceleration is less than 1.5 % (and is dominated by the SBS mass rather than by the geometrical details of the side-vent channels).

5. In our future work, neglected turbulence, non-Newtonian fluid and soil granularity effects will be investigated to obtain a more accurate assessment of the blast momentum reduction.

2.8. Appendix A

In this section, a brief overview is provided of the key functional relations defining the CU-ARL soil material model [17-19].

Within the CU-ARL material model, soil is considered to generally have a complex structure consisting of mineral solid particles which form a skeleton. The pores between the solid particles are filled with either: (a) a low-moisture air (this type of soil is generally referred to as "***dry soil***"); (b) water containing a small fraction of air ("***saturated soil***"); or (c) with comparable amounts of water and air ("***unsaturated soil***"). The relative volume fractions of the three constituent materials in the soil (the solid mineral particles, water and air) are generally quantified by the porosity, α, and the degree of saturation (Saturation Ratio), β, which are respectively defined as: $\alpha = 1 - \overline{\rho} = \dfrac{V_p}{V}$ and $\beta = \dfrac{V_w}{V_p}$, where V_p is the volume of void (pores), V_w is the volume of water and V is the total volume.

The three main components of the CU-ARL soil model are overviewed in the following three sub-sections.

A.1 Equation of State

For the CU-ARL soil model, a porous-material/compaction equation of state is used which is a particular form of the Mie-Gruneisen equation of state:

$$P = P_H + \Gamma\rho\left(E - E_H\right) \tag{2-A.1}$$

in which the internal energy density dependence of the pressure is neglected. In Eq. (2-A.1), the following nomenclature is used: P is pressure (a sum of the pore pressure and effective stress in the soil skeleton), ρ the (current) mass density, Γ the Gruneisen gamma parameter, E the internal energy density and the subscript H is used to denote the reference shock-Hugoniot level of a given quantity.

By assuming a linear relationship between the shock speed, U_s, and the particle velocity, U_p [24], the Hugoniot pressure, P_H, is defined using the following expression for a stationary shock [13]:

$$P_H = \frac{\rho_0 C_0^2 \eta}{(1 - s\eta)^2} \tag{2-A.2}$$

Where $\rho_0 = (1-\alpha_0)\rho_{ref} + \alpha_0\beta_0\rho_w$ is the initial soil material mass density, where C_0 is the y-p equal to zero intercept in the U_s vs. U_p plot, for the homogenized soil medium [15], $\eta = \left(1 - \frac{\rho_0 - \alpha_0\beta_0\rho_w}{\rho - \alpha_0\beta_0\rho_w}\right) = \left(1 - \frac{(1-\alpha_0)\rho_{ref}}{\rho - \alpha_0\beta_0\rho_w}\right)$ the compressibility ratio, ρ_w the density of water and the parameter s represents a rate of increase of the (average) material-particle (not to be confused with soil particle) velocity, U_p, with an increase in the shock velocity, U_s and is defined by fitting U_s vs. U_p experimental data with the following linear function:

$$U_s = C_0 + sU_p \tag{2-A.3}$$

In the CU-ARL soil-model equation of state, the aforementioned relations for ρ_0 and η are substituted in Eq. (2-A.3) to get:

$$P = P_H = \frac{((1-\alpha_0)\rho_{ref} + \alpha_0\beta_0\rho_w)C_0^2\left(1 - \frac{(1-\alpha_0)\rho_{ref}}{\rho - \alpha_0\beta_0\rho_w}\right)}{\left(1 - s\left(1 - \frac{(1-\alpha_0)\rho_{ref}}{\rho - \alpha_0\beta_0\rho_w}\right)\right)^2}, \qquad \rho \le \rho_{comp} \tag{2-A.4a}$$

and

$$P = P_H = P(\rho_{comp}) + C_0^2(\rho - \rho_{comp}), \qquad \rho > \rho_{comp} \tag{2-A.4b}$$

where $\rho_{comp} = \left(\frac{1-\alpha_0}{1-\alpha_0+\alpha_0\beta_0}\right)\rho_{ref} + \left(\frac{\alpha_0\beta_0}{1-\alpha_0+\alpha_0\beta_0}\right)\rho_w$ is the density of the soil at full compaction.

To account for the effect of saturation/hydration on the values of material parameters C_0 and s, the results obtained in Refs. [15,17] are fitted to a low order polynomial in which the coefficients are set to depend on the initial level of porosity and the reference density. These relations in conjunction with Eqs.(2-A.4a) and (2-A.4b) define the dependence of pressure on ρ_{ref}, α_0, β_0 and ρ.

The P vs. ρ relation just derived is valid only during loading and only when such loading gives rise to irreversible/plastic compaction of the porous material. It should be noted that the term loading implies an event within which the pressure is increased (and, in the case of plastic loading, a decrease in material porosity takes place). Conversely, unloading is associated with a decrease in pressure. As shown in our previous work [20], during unloading/elastic-reloading, the P vs. ρ relationship is defined as $\frac{dP}{d\rho} = C_0^2\left(\rho_{ref}, \alpha_0, \beta_0\right)$, where the $C_0\left(\rho_{ref}, \alpha_0, \beta_0\right)$ relation can be found in Ref.[17].

A.2 Strength Model

Within the dry-soil rendition of the CU-ARL soil model, material strength (a quantity which quantifies material's resistance to inelastic distortive deformation) is assumed to be pressure dependent, controlled by inter-particle friction and to be defined by the following relation:

$$\sigma_{y,dry} = \phi_{dry} P_{dry} \approx \begin{cases} 1.3732 P_{dry} & 0 < P_{dry} \le P_{MC} \\ 1.3732 P_{MC} & P_{dry} > P_{MC} \end{cases} \tag{2-A.5}$$

In the case of saturated soil, the CU-ARL soil model defines pressure-dependent material strength as:

$$\sigma_{y,sat} = \begin{cases} \phi_{sat} P_{sat} & 0 \le P_{sat} \le P_{MC} \\ \phi_{sat} P_{MC} & P_{sat} > P_{MC} \end{cases} \tag{2-A.6}$$

where the yield-stress-to-pressure proportionality coefficient, ϕ_{sat}, is defined as:

$$\phi_{sat} = \begin{cases} \left(0.1 + 1.2732 \dfrac{P_{sat}}{P_{MC}}\right) & 0 \le P_{sat} \le P_{MC} \\ 1.3732 & P_{sat} > P_{MC} \end{cases} \tag{2-A.7}$$

The term P_{MC} (=1.864.10^5 kPa) appearing in Eqs. (2-A.5)-(2-A.7) is the Mohr-Coulomb pressure (a pressure threshold beyond which the material strength is pressure insensitive). It should be noted that none of the Eqs. (2-A.5)-(2-A.7) include the effect of strain rate on the soil material strength. This was justified in our previous work [17], where it was shown that as long as the model is used at high deformation rates (ca. >1.0.10^{2}s^{-1}), the strength and failure behavior of soil can be considered rate independent.

Within the CU-ARL soil strength model, the strength vs. pressure relationship for unsaturated soil is defined using a linear combination of the strength/pressure proportionality coefficients in dry and the saturated soils as:

$$\sigma_{y,unsat} = \begin{cases} \phi_{unsat} P_{unsat} & 0 \le P_{unsat} \le P_{MC} \\ \phi_{unsat} P_{MC} & P_{unsat} > P_{MC} \end{cases} \tag{2-A.8}$$

where

$$\phi_{unsat} = (1 - \beta_o)\phi_{dry} + \beta_o \phi_{sat} \tag{2-A.9}$$

Defined in this way, Eqs. (2-A.8) and (2-A.9) can be also used for dry soil (β_0 = 0.0) and saturated soil (β_0 = 1.0).

In addition to specifying the strength vs. pressure relationship, the compaction strength model entails the knowledge of the density dependent shear modulus. Since water has no ability to support shear stresses, the shear modulus, *G*, of unsaturated soil is dominated by the shear modulus of the solid skeleton of the soil. However, the presence of water changes the density of the soil. Therefore, the original compaction shear modulus vs. density relationship for dry soil

was appropriately modified by: (a) correcting density with a $-\alpha_0\beta_0\rho_w$ term and (b) introducing a moisture-level dependent maximum shear modulus in order to obtain a (deformation-rate independent) shear modulus vs. density relationship for soil at different saturation levels. This procedure yielded the following shear modulus vs. density functional relationships:

$$G(kPa)=\begin{cases}5.2175\cdot 10^{-14}(\rho-\alpha_0\beta_0\rho_w)^6 & \rho(kg/m^3)<(1-\alpha_0\beta_0)\rho_{ref}+\alpha_0\beta_0\rho_w \\ (1-\alpha_0\beta_0)G_{Bulk} & \rho(kg/m^3)>=(1-\alpha_0\beta_0)\rho_{ref}+\alpha_0\beta_0\rho_w\end{cases} \quad \text{(2-A.10)}$$

where G_{Bulk} (=3.73470.10^7) denotes the shear modulus of fully compacted dry soil. Eq. (2-A.10) correctly accounts for the fact that, at full compaction, the soil density is equal to $(1-\alpha_0\beta_0)\rho_{ref}+\alpha_0\beta_0\rho_w$.

It should be noted that in the strength model developed in this section, the contribution of water to the material strength was neglected. This can be justified by recognizing the fact that viscosity of water is typically around 0.001 Pa.s and that even at very high deformation rates (1.0.10^5 s^{-1}), the contribution of water to the shear strength of the soil is merely around 100Pa.

A.3 Failure Model

It is well established that the presence of moisture in soil increases the soil's cohesive strength [21]. Therefore, the magnitude of the (negative) failure pressure for soil is expected to increase with the degree of saturation (β). Also, the moisture content should be substantial (β>0.7) before its effect on the cohesive strength of soil becomes significant [21]. To account for these two observations, within the CU-ARL soil failure model [17], the following expression was proposed for the magnitude of the (negative) failure pressure in unsaturated soil; $P_{fail,unsat}$:

$$P_{fail,unsat}=\beta_0^5 P_{fail,sat} \quad \text{(2-A.11)}$$

where $P_{fail,sat}$ (set equal to 70kPa) is the failure pressure in saturated soil [21]. The relationship given by Eq. (2-A.11) correctly predicts that the cohesive strength of unsaturated soil with a degree of saturation of 0.7 is around 10-15% of that in the saturated soil.

2.9. References

1. K. Barry and C. Philpot, "***Humvee for Victory***," Car and Driver, Nov. 2011, 22-23.

2. F. Ma, J. Y. Choi and V. Yang, "***Propulsive Performance of Air Breathing Pulse Detonation Engines***," Journal of Propulsion and Power, 22, 6, 2006, 1188-1203.

3. J. Capouellez, K. Drotleff, G. Wolfe, A. Cichosz, F. Helsel, A. Mikaila, J. R. Pickens , R. W. Semelsberger, S. Kerr, E. Wettlaufer, P. Massoud, J. Wood and B. Barringer, "***Optimized Light Tactical Vehicle***,", 27th Army Science Conference, No. FP-11, 2010, 1-8.

4. K. Brannen, "***Blast Chimney Shows Promise, Questions Remain***," Defense News, 22 July 2011, http://www.defensenews.com/story.php?i=7166742.

5. K. Brannen, "***'Chimney' Deflects IEDs***," Defense News, 1 Nov. 2010, http://www.defensenews.com/story.php?i=4996368.

6. Z. C. Owens and R. K. Hanson, "***Single-Cycle Unsteady Nozzle Phenomena in Pulse Detonation Engines***," Journal of Propulsion and Power, 23, 2007, 325-337.

7. X. He and A. R. Karagozian, "***Numerical Simulation of Pulse Detonation Engine Phenomena***," Journal of Scientific Computing, 19, 2003, 201-224.

8. ABAQUS Version 6.10, ***User Documentation***, Dassault Systems, 2010.

9. M. Grujicic, G. Arakere, H. K. Nallagatla, W. C. Bell, I. Haque, "***Computational Investigation of Blast Survivability and Off-road Performance of an Up-armored High-Mobility Multi-purpose Wheeled Vehicle (HMMWV)***," Journal of Automobile Engineering, 223, 2009, 301-325.

10. M. Grujicic, W. C. Bell, G. Arakere and I. Haque, "***Finite Element Analysis of the Effect of Up-armoring on the Off-road Braking and Sharp-turn Performance of a High-Mobility Multi-purpose Wheeled Vehicle (HMMWV)***," Journal of Automobile Engineering, 223, D11, 2009, 1419-1434.

11. M. Grujicic, H. Marvi, G. Arakere, W. C. Bell and I. Haque, "***The Effect of Up-armoring the High-Mobility Multi-purpose Wheeled Vehicle (HMMWV) on the Off-road Vehicle Performance***," Multidiscipline Modeling in Materials and Structures, 6, 2, 2010, 229-256.

12. M. Grujicic, G. Arakere, W. C. Bell, I. Haque, "***Computational Investigation of the Effect of Up-armoring on Occupant Injury/Fatality Reduction of a Prototypical High-mobility Multi-purpose Wheeled Vehicle Subjected to Mine-blast***," Journal of Automobile Engineering, 223, 2009, 903-920.

13. ANSYS/AUTODYN, ***Theory Manual***, version 6.1, 2009.

14. M. Grujicic, B. Pandurangan and B. Cheeseman, "***A Computational Analysis of Detonation of Buried Mines***," Multidiscipline Modeling in Materials and Structures, 2, 2006, 363-387.

15. A. M. Bragov, A. K. Lomunov, I. V. Sergeichev, K. Tsembelis and W. G. Proud, "***The Determination of Physicomechanical Properties of Soft Soils from Medium to High Strain Rates***," International Journal of Impact Engineering, 35, 9, 2008, 967-976.

16. D. J. Chapman, K. Tsembelis and W. G. Proud, "***The Behavior of Water Saturated Sand under Shock-loading***," Proceedings of the 2006 SEM Annual Conference and Exposition on Experimental and Applied Mechanics, 2, 2006, 834-840.

17. M. Grujicic, B. Pandurangan, B. A. Cheeseman, W. N. Roy, R. R. Skaggs and R. Gupta, "***Parameterization of the Porous-Material Model for Sand with Various Degrees of Water Saturation***," Soil Dynamics and Earthquake Engineering, 28, 2008, 20-35.

18. M. Grujicic, B. Pandurangan, N. Coutris, B. A. Cheeseman, W. N. Roy and R. R. Skaggs, "***Derivation and Validation of a Material Model for Clayey Sand for Use in Landmine Detonation Computational Analysis***", Multidiscipline Modeling in Materials and Structures, 5, 4, 2009, 311-344.

19. M. Grujicic, B. Pandurangan, N. Coutris, B. A. Cheeseman, W. N. Roy and R. R. Skaggs, "***Computer-simulations based Development of a High Strain-rate, Large-deformation, High-pressure Material Model for STANAG 4569 Sandy Gravel***," Soil Dynamics and Earthquake Engineering, 28, 2008, 1045–1062.

20. M. Grujicic, B. Pandurangan and B. Cheeseman, "***The Effect of Degree of Saturation of Sand on Detonation Phenomena Associated with Shallow-buried and Ground-laid Mines***," Journal of Shock and Vibration, 13, 2006, 41-62.

21. S. Stein and T. Kim, "***Effect of Moisture on Attraction Force on Beach Sand***," Marine Geosources and Geotechnology, 22, 2004, 33-47.

22. J. von Neumann, "***The point source solution***," A. J. Taub, editor, John von Neumann: Collected Works, 6, 219-237, Pentagon Press, 1963.

23. S. Stein and T. Kim, "***Effect of Moisture on Attraction Force on Beach Sand***," Marine Geosources and Geotechnology, 22, 2004, 33-47.

24. G. I. Kerley, "***The Linear US-uP Relation in Shock-Wave Physics***," Kerley Technical Services Research Report, KTS06-1, 2006, 1-21.

CHAPTER 3: A COMBINED FINITE-ELEMENT/DISCRETE-PARTICLE ANALYSIS OF A SIDE-VENT-CHANNEL-BASED CONCEPT FOR IMPROVED BLAST-SURVIVABILITY OF LIGHT TACTICAL VEHICLES

3.1. Abstract

The recently proposed concept solution for improving blast-survivability of the light tactical military vehicles is critically assessed using combined finite-element/discrete-particle computational methods and tools. The proposed concept involves the use of side-vent-channels attached to the V-shaped vehicle underbody. The solution involves extension and modification of the so-called "***blast chimney***" concept, which consists of a vertical channel connecting the bottom and the roof and passing through the cabin of a light tactical vehicle. However, in contrast to the blast-chimney solution, the side-vent-channel solution is not expected to: (a) reduce the available cabin space; (b) interfere with the vehicle occupants' ability to scout the surroundings; and (c) compromise the vehicle's off-road structural durability/reliability. Furthermore, the concept solution attempts to exploit ideas and principles of operation of the so-called "***pulse detonation***" rocket engines in order to create a downward thrust on the targeted vehicle. To maximize the downward thrust effects and minimize the extent of vehicle upward movement, standard engineering optimization methods and tools are employed for the design of side-vent-channels. The results obtained confirmed the beneficial effects of the side-vent-channels in reducing the blast momentum, although the extent of these effects is quite small (3–4%).

3.2. Introduction

In the present work, the recently proposed side-vent-channel-based blast-mitigation concept [1] for increasing soil-buried mine-blast survivability of light tactical vehicles (e.g. the High Mobility Multipurpose Wheeled Vehicle, HMMWV) has been investigated using a combined finite-element/discrete-particle computational analysis. Hence, the main topics to be overviewed in this introductory section of the present manuscript include: (a) main limitations of the (light) tactical vehicles currently in use; (b) detonation of shallow-buried mines; (c) impulse loading resulting from the interaction of soil ejecta and gaseous detonation products with a target structure; and (d) the side-vent-channel blast-mitigation concept. As far as a review of the computational methods used in the analysis of various mine-blast scenarios is concerned, it will be presented in Section II.

Limitations of the Current Tactical Vehicles: The HMMWV is the prototypical light tactical vehicle used by the US military. This vehicle was designed/developed during the Cold War and, not surprisingly, has been found lacking the necessary blast and ballistic resistance in the recent and the ongoing asymmetric warfare, in which the distinction between front line combat and transportation convoys has been severely blurred. Thus, in the past conflict in Iraq and the ongoing conflict in Afghanistan, HMMWVs have mostly been replaced by larger, heavier MRAP (Mine Resistant Ambush Protected) vehicles, which have been specifically designed for resistance to IEDs (Improvised Explosive Devices) blast [2]. However, the added mass which plays a key role in the superior IED survivability of the MRAP, also negatively affects other performance aspects of this vehicle. Specifically: (a) tactical utility/mobility of the MRAP is severely compromised relative to that of the HMMWV; (b) diminished maneuverability of the larger vehicle on narrow city streets; (c) poor fuel economy; (d) the MRAP weight exceeds the

payload capacity of the CH-47 Chinook helicopter [2] severely affecting its transportability; and (e) its weight exceeds the load carrying capacity of over 70% of the world's bridges [3] seriously reducing the extent of its deployment.

Detonation of Shallow Buried Mines: Detonation is a high-rate chemical reaction in which condensed matter explosive is converted into high-pressure, high-temperature expanding gases (commonly referred to as gaseous detonation products). Expansion of the gaseous detonation products against the surrounding medium is associated with exchange of linear momentum and various energy components (e.g. potential, thermal, kinetic, strain, etc.). In the case of detonation of soil-buried land-mines, two extreme scenarios are generally identified: (a) the so-called "***camouflet***" scenario in which the mine depth of burial is so large that the high potential energy of the detonation products is almost exclusively transformed into inelastic and elastic strain energy of the soil as well as into surface energy of fractured soil particles. In this case, attenuation of the detonation-induced shock waves within the soil is so prevalent that no significant blast wave is generated at the air/soil interface and no soil ejection takes place. In addition, gaseous detonation products remain trapped within the soil. Therefore, in the case of camouflet, structures located at or above the ground are not exposed to any significant threat while underground structures in close proximity can be threatened; and (b) the ground-laid mine detonation scenario in which the impulse energy carried by air-borne shock waves and the kinetic energy of the detonation products pose the main threat to an above-the-ground target structure.

In the majority of situations, mines are shallow-buried in soil and, hence, neither of these extreme scenarios is encountered. While blast waves and detonation products still pose a threat to the target structure, the soil ejecta pose a greater threat. Consequently, the detonation of shallow-buried mines is of main concern to the designers and developers of targeted structures with high

blast survivability (e.g. vehicle hull). That is the reason that this regime of mine deployment is discussed in greater detail in the remainder of this section.

The shallow-buried mine detonation process can be described in terms of three well defined temporal phases, Figures 3-1(a)–(f):

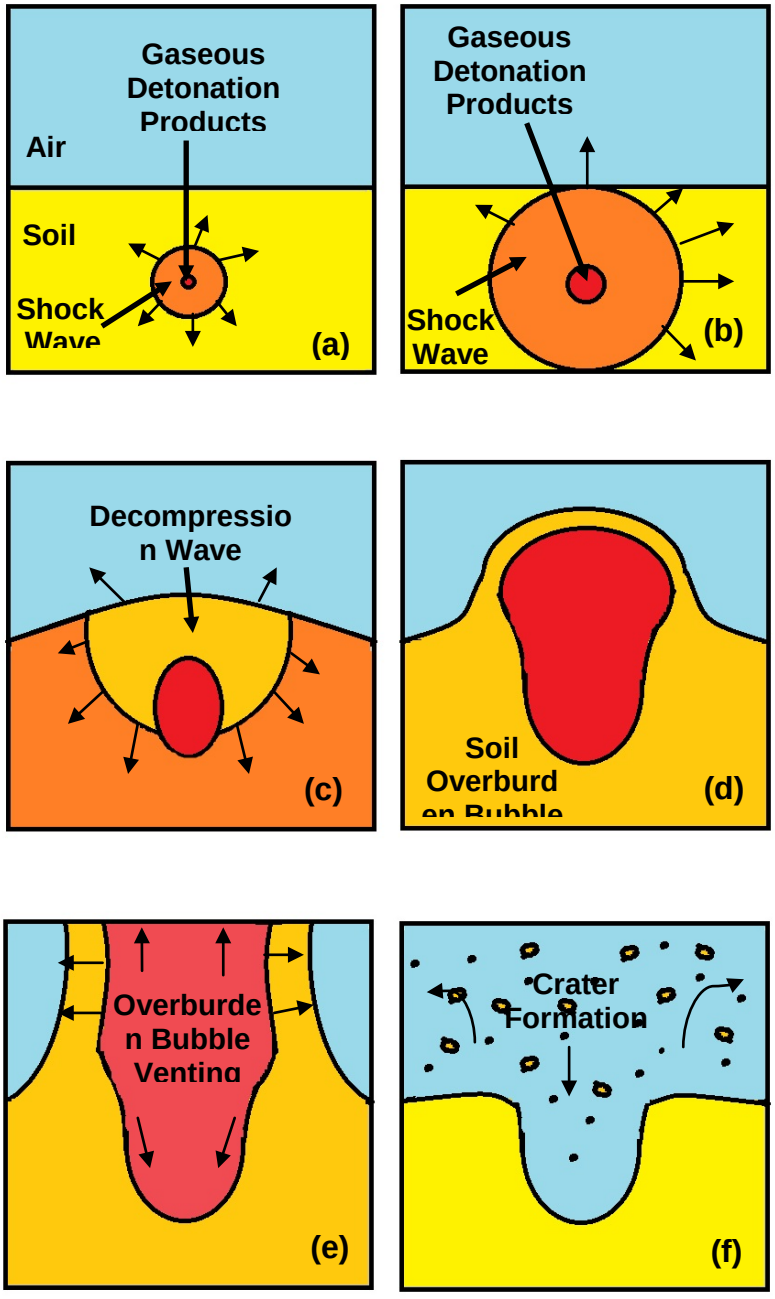

Figure 3–1 Various phases of detonation of a landmine shallow-buried in soil. Please see text for details.

(a) The initial phase, which is characterized by the interaction of high-pressure, high-temperature expanding gaseous detonation products with the surrounding soil. Within this phase, one can typically identify three distinct zones within the soil, the sizes of which scale with the mine characteristic dimension (e.g. radius, R_e). The innermost zone, commonly referred to as the "***zone of crushing***", extends ca. $2R_e$– $3R_e$. Within this zone the pressures and temperatures are so high that the soil melts/evaporates, rendering knowledge of the material constitutive response irrelevant. The intermediate zone extends between ca. $3R_e$ and $6R_e$, and the soil response to detonation-induced shock loading is dominated by irreversible compaction and crushing/fracturing of the soil particles. The outermost zone extends beyond ca. $6R_e$ and the (attenuated) shock-induced soil response within this zone is dominated by reversible/elastic deformation of the soil. It is generally believed that the initial phase of shallow-buried mine detonation controls the amount of energy available for conversion into soil kinetic energy and, in turn, the extent of threat posed to the targeted structure (e.g. [4]). Furthermore, the magnitude of the energy available for conversion is affected by factors such as mine shape, mine depth-of-burial, soil properties, etc.;

(b) The initial phase ends, and the next phase (commonly known as "***soil-overburden bubble initiation phase***") begins, at the moment of arrival of the soil-borne shock wave to and the interaction with the soil/air interface. Due to a large shock-impedance mismatch between soil and air, this interaction results in a weak transmitted compressive shock to air and a very strong reflected tensile-shock/release-wave. Under the influence of the tensile-shock/release-wave and the expanding high-pressure detonation products, the soil overburden begins to expand outward, forming (initially) a hemi-spherical dome. This phase typically lasts for a few milliseconds and

ends with the moment of rupture of soil overburden and the onset of venting of the detonation products; and

(c) The final phase of shallow-buried mine detonation is characterized by gaseous detonation product venting and pronounced soil ejection. Typically, the soil overburden represents only a minor fraction of the total ejected soil. The remaining major portion of the ejected soil is the result of the erosion of the cavity walls by the swirling gaseous detonation products, still residing within the cavity. This interaction gives rise to the formation of a soil crater with a volume many times larger than the volume of the detonated charge. The trajectory of the ejected soil falls within an inverted cone with an included angle (between 60–90°). Typically, the included angle varies inversely with DOB and soil initial density.

Detonation-induced Impulse Loading Experienced by the Target Structure: Numerous instances of soldier casualties and tactical vehicle destruction incurred by the U.S. military during the recent/ongoing campaigns in Iraq and Afghanistan have been caused by buried and roadside landmines. Detonation of these landmines produces large impulsive loads on the targeted vehicle/personnel through impact by the resulting blast waves, ejected soil and expanded gaseous detonation products. Development of military vehicles (and general structural platforms) with a high-level of blast-survivability entails: (a) the understanding of and ability to quantify the impulsive loads associated with the detonation of landmines deployed in soil of differing compositions/constitutions; and (b) the ability to predict the kinematic and structural (including failure) response of the targeted platforms. Acquiring such understanding and predictive ability, however, is typically quite challenging since the detonation-induced loads depend strongly on the deployed mine's shape, size and depth of burial (DOB), the distance between the soil surface and

the target (the so-called stand-off distance, SOD), and the soil properties (density, particle size and distribution, presence of inorganic/organic matter, water content, etc.).

An examination of the public-domain literature conducted for the present work revealed a number of scientific papers and technical reports pertaining to the problem of detonation of buried (explosive) charges. Most of the reported studies, however, are focused on the investigation of soil cratering processes (with emphasis on the efficient utilization of explosives for excavation) and not on the elucidation of blast phenomena and characterization of landmine blast output or on the survivability of structures subjected to blast-loading [4].

Among the reported experimental studies dealing with mine-detonation loading and kinematic/mechanical response of the targeted structure, the following appear to be the most closely related to the subject matter of the current study: (a) Westine et al. [5] conducted a series of experiments using a plate fixtured and centered above a (Anti-Tank landmine-simulating) buried charge. The plate was perforated at different radial distances and plugs of known mass were placed in the holes. Under the influence of the mine detonation-induced blast loads, the plugs were forced out of the plate and the local impulsive loading on the plate was quantified by measuring the plug velocity; (b) based on the results of Westine et al. [5], Morris [6] developed a computer code for design of mass-efficient, blast survivable vehicles/structures; (c) in the work of Bergeron et al. [7], an instrumented ballistic pendulum was utilized to investigate mine detonation-induced loads experienced by a target structure. In addition, this work quantified: (i) the time-dependent pressure and impulse at several locations in air directly above the mine; (ii) the time-dependent pressure and impulse at several locations in the sand surrounding the mine; and (iii) x-radiographs and high speed photographs of the associated soil cratering and ejection

phenomena; and (d) the work of Bergeron et al. [7] was subsequently extended by Braid [8] who incorporated improved instrumentation along with different charge sizes and soil types.

The Side-Vent-Channel Blast-Mitigation Concept: Due to the aforementioned inadequate blast-survivability of the light tactical vehicles, the US military is in constant search of new and effective blast-mitigation concepts which do not compromise vehicle mobility/maneuverability, transportability, deployability or fuel economy. One of such concepts is the integration of the so-called blast chimney into the conventional HMMWV. The blast chimney is simply a vertical channel which connects the vehicle bottom to its roof and enables the venting of soil ejecta, gaseous detonation products and mine casing fragments [2, 9] resulting from a mine blast underneath the vehicle.

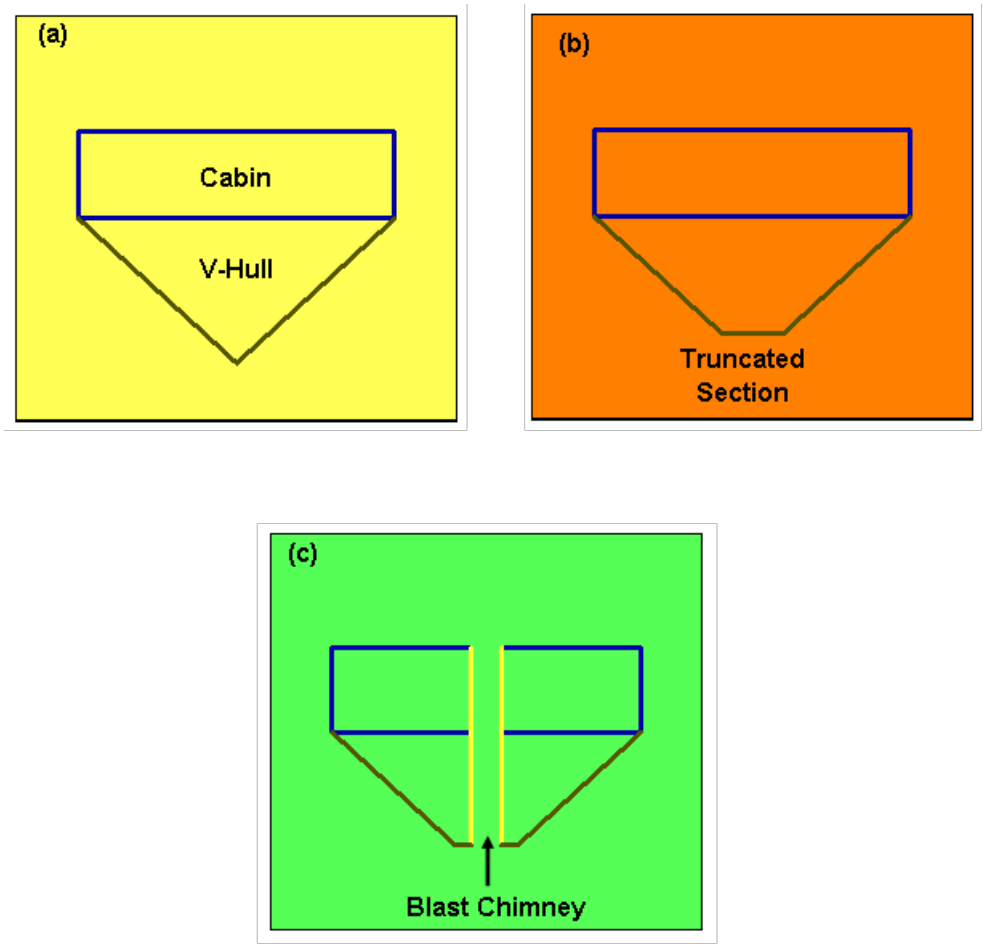

Figure 3–2 Three blast-mitigation vehicle-hull concepts: (a) V-shaped hull; (b) truncated V-shaped hull; and (c) same as (b) but with addition of a blast chimney.

Due to the sensitive nature of the subject matter, relatively little has been reported in the open literature regarding the blast-mitigation potential of the blast chimney concept. Nevertheless, it is suggested that the blast chimney improves the blast-survivability of light tactical vehicles beyond the level offered by the V-shaped hull of the vehicle in two ways: (a) by enabling venting of soil ejecta, gaseous detonation products and mine casing fragments (and thus lowering the blast impulse transferred to the vehicle); and (b) by creating a downward thrust on the vehicle via the promotion of supersonic expansion of gaseous detonation products exiting the blast chimney [10] (and thus lowering the possibility for the vehicle lift-off from the ground). To highlight the additional blast-mitigation effect offered by the blast chimney, simple schematics of three vehicle hull configurations/geometries are depicted in Figures 3-2(a)–(c). The conventional V-hull is depicted in Figure 3-2(a). In this case, the blast mitigation performance increases with an increase in the V-hull steepness. However, constraints associated with vehicle ground clearance and height limit the maximum allowable V-hull steepness. A truncated V-hull design is depicted in Figure 3-2(b). In this case, the blast mitigation performance is enhanced relative to that offered by the design depicted in Figure 3-2(a) since the benefits (decreased blast impulse) offered by the increased steepness of the V-hull outweighs the penalty (i.e. increased blast impulse) incurred due to the small flat section. As seen in Figure 3-2(c), incorporation of a chimney, allows the gaseous detonation products, soil ejecta and mine casing fragments under the chimney to be vented, while still permitting high-steepness V-hull sides [10].

While the blast-chimney concept offers benefits relative to the reduction in the blast momentum transferred to the target vehicle, it is also associated with at least two major shortcomings: (a) Not surprisingly, it has been found that the incorporation of the chimney which runs through the vehicle cabin limits the mobility of the occupants within the vehicle and their

ability to survey the surroundings [9]; and (b) Off-road vehicle-testing performance studies have indicated a loss in the vehicle structural reliability and durability which has been currently attributed to the enhanced rate of vehicle-frame fatigue-induced failure which, in turn, has been linked with the aforementioned increased cabin rigidity [9].

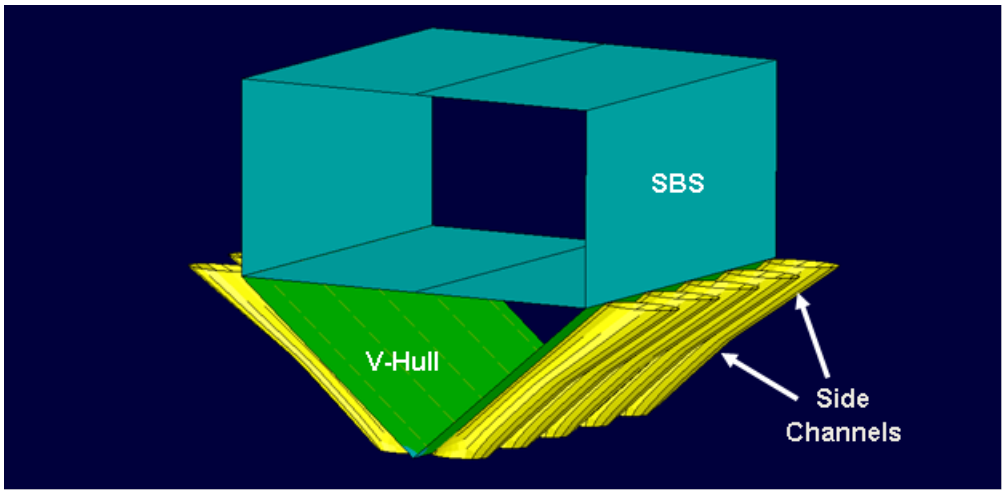

Figure 3–3 Side channels/tubes based blast-mitigation concept originally proposed in Ref. [1]. Note that the abbreviation SBS stands for "*surrogate box structure*".

To address the aforementioned limitations of the blast-chimney concept related to the loss of cabin space, ability of the vehicle occupants to scout the environment and degradation of the vehicle's structural durability/reliability, a new blast-mitigation concept (the so-called "***side-vent-channels concept***" [1]) has been recently proposed and investigated computationally. As shown schematically in Figure 3-3, this concept utilizes side vent tubes/channels (of the appropriate cross sectional shape and wall thickness) attached to the V-shaped vehicle underbody and open at both ends. The bottom end of each tube is cut parallel to the ground (to promote inflow of the detonation by-products and soil ejecta and to prevent structural collapse, crushing, of the tube inlet under blast loads) and flush with the V-hull bottom. The channels/tubes are intended to function as exhaust nozzles as in the case of the pulse-detonation engine and, thus, provide a downward thrust to the vehicle. The secondary role of the channels/tubes is to reduce the blast momentum transferred to the targeted vehicle by enabling the venting of the gaseous detonation products, soil ejecta and mine-casing fragments. The geometry of the side-vent-channels is optimized with respect to the attainment of the maximum downward thrust on the vehicle by coupling an optimization algorithm with a computational analysis (analogous to the one often employed in the case of design of pulse detonation rocket engines). It should be noted that in order to prevent potential misuse, of the ideas proposed and the results obtained in the present work, the term "***vehicle***" has been replaced in Figure 3-3 as well as in the remainder of the manuscript with the term "***surrogate box structure***" (SBS).

The computational analysis employed in Ref. [1] was of a combined Lagrangian/Eulerian fluid-structure interaction (FSI) type and, hence, suffered from at least the following two major deficiencies: (a) difficulties in defining the Eulerian material (e.g. detonation products, soil and air) interfaces and Lagrangian/Eulerian contact surfaces; and (b) inability to fully account for the

granular nature of the soil ejecta. These deficiencies of the combined Eulerian/Lagrangian analyses employed in the computational investigation of the side-vent-channel concept are addressed in the present work.

Main Objectives: The main objective of the present work is to address the aforementioned deficiencies of the computational analyses of the side-vent-channel concept reported in Ref. [1] by employing a combined finite-element/discrete-particle computational algorithm. Within this purely Lagrangian algorithm, difficulties associated with the definition of the material surfaces and contact interfaces are avoided while soil (as well as the detonation products and air) is given a discrete-particle character.

Paper Organization: A brief description of the problem analyzed in the present work and a brief overview of the computational methods and tools used are provided in Section II. The main results obtained in the current work are presented and discussed in Section III. The main conclusions resulting from the present work are summarized in Section IV.

3.3. Problem Description and Computational Analysis

As mentioned earlier, the main objective of the present work is to re-examine the new side-vent-channels blast-mitigation concept using a novel coupled finite-element/discrete-particle computational analysis. In this section, details are presented regarding the basic problem formulation as well as regarding the computational procedure utilized.

3.3.1. Problem Description

The basic problem analyzed in the present work involves a prototypical buried-mine detonation event followed by the interaction of gaseous detonation products, soil ejecta and blast waves with the target structure, a mock-up of an SBS equipped with a V-shaped vehicle hull underbody and side-vent-channels. Details regarding the computational model and the numerical procedure employed in the present work to investigate the blast-mitigation potential of the side-vent-channel concept are presented in subsequent sections.

3.3.2. Computational Domain

The computational domain used consists of two separate sub-domains, one of the continuum Lagrangian-type and the other of a discrete-particle type. The Lagrangian sub-domain comprises the SBS equipped with the V-hull and side channels, and is modeled as a finite-element structure consisting of 61,348 three-noded shell elements. In most of the analyses, the SBS structure is rigidized while in a few other analyses flexibility/deformability and damage/structural failure of the SBS was taken into account. During the vent-channel-geometry optimization, the inlet cross-sectional area and the outlet-to-inlet area ratio were varied.

As far as the discrete-particle sub-domain is concerned, it comprises mine/detonation-products, sand/soil, and the ambient air. The discrete-particle sub-domain is of a rectangular parallelepiped shape which encloses the SBS. Details regarding the discrete-particle modeling and simulations will be presented in the next section.

It should be noted that the SBS structure possesses two vertical planes of symmetry, suggesting that only one-quarter of the computational domain has to be analyzed explicitly. However, due to random distribution of the discrete (detonation-products, soil and air) particles, the entire computational domain was analyzed. By analyzing the entire computational domain, rather than one of its quarters, potential rotation of the SBS is also enabled. Figure 3-4 shows an initial configuration of the prototypical computational domain analyzed.

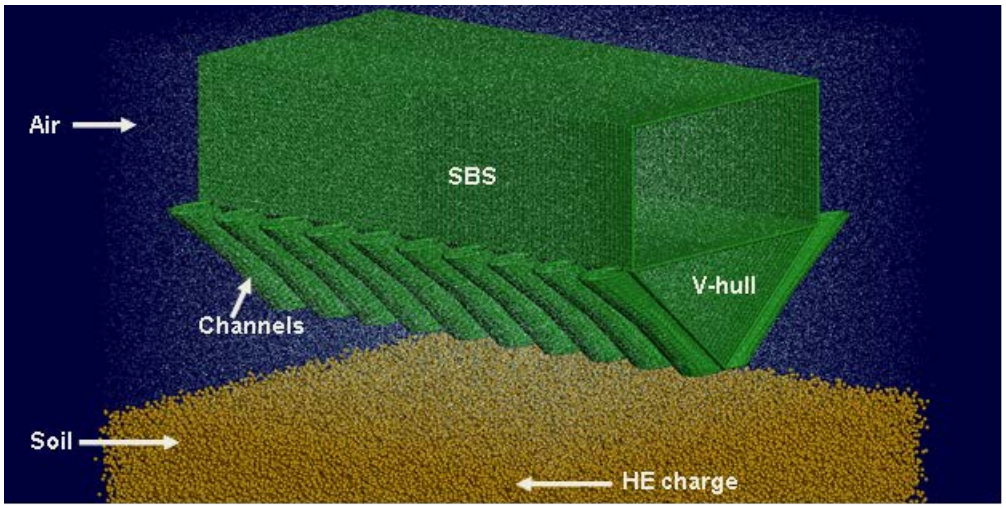

Figure 3–4 A prototypical computational domain used in the combined three-dimensional finite-element/discrete-particle analysis of the buried-mine detonation event and the subsequent interactions of the detonation products, soil ejecta and air blast with the SBS equipped with a V-hull and side vent channels. Please note that the mine is shallow-buried and its view is obstructed by the surrounding soil.

3.3.3. Discrete-Particle Formulation

As mentioned above, the behavior of high-explosive (HE) gaseous detonation products, soil and air, following detonation, and during their collision with the SBS is modeled in the present work using the discrete-particle (also known as the "***corpuscular***") approach proposed recently by Olovsson et al. [11]. Within this approach, HE gaseous detonation products, soil and air are all represented as assemblies of discrete, rigid, spherical, interacting particles which exchange momentum and kinetic energy during their collisions/contact with each other and/or the SBS. To make the computational cost manageable, each particle is defined to represent a collection of 10^{15}–10^{20} molecules.

As explained by Børvik and co-workers [12, 13], the discrete-particle method has the following three main advantages over the commonly used combined Lagrangian-Eulerian approaches: (a) due to its Lagrangian (material-based) character, the method does not require the calculation of the material advection through the mesh and, hence, does not suffer from errors associated with such calculation; (b) numerical detection and quantification of the contacts and interactions between HE detonation products, soil and air and complex-geometry Lagrangian target structures, which are quite challenging within the combined Lagrangian-Eulerian framework, is greatly simplified and accelerated; and (c) within the same computational model, HE detonation products, soil and air (all modeled using the discrete-particle approach) can be combined with continuum-Lagrangian-type target structures to analyze various scenarios related to detonation of shallow-buried mines and the interactions of the detonation products, soil ejecta and air-borne blast-waves with the structures.

In the remainder of this section, details are presented regarding the discrete-particle models for the HE detonation products, air and soil (with different levels of hydration). It should be noted that, as explained by Olovsson et al. [11], discrete-particle models for the HE detonation

products and air are essentially an extension of the kinetic molecular theory of gases, as formulated in 1860 by Maxwell [14]. Specifically: (i) discrete particles used in the numerical model represent a collection of a large number of atoms constituting the material in question; and (ii) inter-particle collisions are assumed to be purely elastic (i.e. kinetic-energy-preserving).

Kinetic Molecular Theory of Gases

The kinetic molecular theory is a theory which successfully relates molecular-level events such as collisions to the macroscopic properties, e.g. pressure or temperature of an ideal gas. Within the theory, the system of interacting gas molecules is assumed to have the following four properties: (a) the size of the molecules is much smaller than the average inter-molecular distance. Consequently, the volume of the molecules is negligible in comparison to the volume of the space within which the gas resides; (b) the system is in the state of thermodynamic equilibrium, i.e. there is no net flux of mass, linear momentum or energy through the system; (c) particle dynamics is governed by Newton's laws of motion; and (d) inter-molecular and molecule/structure interactions are perfectly elastic and, thus, not only the linear momentum but also the total kinetic energy is preserved.

The kinetic molecular theory was originally proposed by Bernoulli [15, 16] and further developed by Maxwell [14]. By carrying out a detailed statistical analysis of molecular-level interactions, Maxwell was able to derive the following (often referred to as the Maxwell-Boltzmann) expression for the equilibrium molecular velocity distribution function, $f(v)$:

$$f(v) = 4\pi \left(\frac{M}{2\pi RT} \right)^{3/2} v^2 \exp\left(\frac{-Mv^2}{2RT} \right) \tag{3-1}$$

where M is the molar mass, R is the universal gas constant and T is the absolute temperature.

Based on Eq. (3-1), Maxwell derived the root-mean-square (rms) molecular velocity, v_{rms}, as:

$$v_{rms} = \sqrt{\int_0^\infty v^2 f(v)\, dv} = \sqrt{\frac{3RT}{M}} \tag{3-2}$$

Under a condition that the gas molecules, modeled as spherical particles, possess a finite radius r_p, additional important quantities characterizing molecular-level interactions within an ideal gas include the mean-free-path, l, and frequency of collisions, f_c, defined as:

$$l = \frac{1}{\sqrt{2}\ \pi\, n\, r_p^2} \tag{3-3}$$

and

$$f_c = n\, r_p^2 \sqrt{\frac{8\pi RT}{M}} \tag{3-4}$$

where n is the number of molecules per unit volume.

Within the kinetic molecular theory of gases, the pressure is the result of the collisions of the molecules with the surroundings. By computing an average rate of change of the momentum per unit area of the surroundings, Maxwell was able to derive the following expression for pressure, p:

$$p = \frac{2}{3} e_t = \frac{m}{3V} \sum_{i=1}^{N} v_i^2 = \frac{mN}{3V} v_{rms}^2 \tag{3-5}$$

where e_t is the translational kinetic energy per unit volume, m is the molecular mass, V is the volume of the system and N is the number of molecules in the system.

High-Explosive Gaseous Detonation Products

The constitutive and the dynamic response of HE gaseous detonation products is represented using the discrete-particle material model proposed by Olovsson et al. [11]. Since a detailed overview of this model could be found in Ref. [11], only a brief account of it is given below. Complete parameterization of the HE discrete-particle model requires specification of the

following four quantities: (i) initial mass density, $\rho_{0,HE}$; (ii) initial volumetric internal energy density, $E_{0,HE}$; (iii) constant-pressure to constant-volume heat-capacity ratio $\gamma_{HE} = C_{p,HE}/C_{v,HE}$; and (iv) fraction of the total volume occupied by the discrete particles, b_{HE} . The four parameters are used to set up a discrete-particle computational model in the following way: (a) once the number of molecules per particle N_{mpp} is selected, $\rho_{0,HE}$ is used to determine the number of particles in the computational volume N_p; (b) since γ_{HE} controls partitioning of the total specific kinetic energy ($E_{0,HE}/V=e_{t,HE}+e_{s,HE}$) into its translational, $e_{t,HE}$, and rotational/vibrational, $e_{s,HE}$, components as:

$$\frac{e_{s,HE}}{e_{t,HE}} = \frac{5-3\gamma_{HE}}{3\gamma_{HE}-3} \tag{3-6}$$

$e_{t,HE}$ and $e_{s,HE}$ could be determined from the given $E_{0,HE}$ and γ_{HE} for a system of a given volume V; and (c) the extent of the so-called "***co-volume***" effect (discussed below) is controlled by the magnitude of b_{HE}.

Børvik et al. [13] pointed out that the kinetic molecular theory-based expression for pressure, Eq. (3-5), typically under-predicts pressure levels at extremely high densities encountered in HE detonation products. The reason for this breakdown is the fact that at such high density levels, the volume of the molecules (the so-called "***co-volume***" effects) could not be neglected (as is done in the case of the kinetic molecular theory). To account for the co-volume effects [17, 18], the radius/size of the HE discrete particles is adaptively increased within the present computational approach. This correction is similar to the van der Waals co-volume correction of the ideal gas pressure, Eq. (3-5), which involves division of the right-hand side of Eq. (3-5) by a factor ($1 - b_{HE}$). In addition to the aforementioned inability of the kinetic molecular theory to accurately predict pressure at high densities, this theory also fails to account for the

experimentally observed sharp drop in pressure during adiabatic expansion of the HE detonation products. To overcome this problem, Olovsson et al. [11] suggested that γ_{HE} be changed from its prototypical value of 7/5 for a di-atomic gas to its maximum theoretical value of 5/3 (i.e. to the value found in a mono-atomic gas). The effect of adiabatic expansion from state 1 to state 2 is described by the following ideal gas relation:

$$\frac{p_2}{p_1} = \left(\frac{V_2}{V_1} \right)^{-\gamma} \tag{3-7}$$

This relation reveals how increasing γ_{HE} from 7/5 to 5/3 increases the rate of adiabatic expansion pressure drop. It should be noted that, as pointed out above, γ_{HE} controls the $e_{s,HE} / e_{t,HE}$ ratio and according to Eq. (3-6), for γ_{HE} = 5/3 this ratio becomes zero. In other words, the total internal energy becomes equal to the kinetic/translational energy (i.e. zero rotational/vibrational kinetic energy is assigned to the HE discrete particles).

In order to parameterize the discrete-particle model for the HE, one must first choose the type/grade of HE. In the present work, C-4 high explosive is selected. For the discrete-particle HE model to be considered realistic, it must reproduce some of the basic findings obtained using experimental and/or purely continuum-type computational approaches. Within the continuum framework, the behavior of HE detonation products is commonly represented using the so-called "***equation of state***" (EOS), a function relating the pressure to the material mass-density/specific-volume and mass-based internal-energy-density/temperature. Typically, either the Jones-Wilkins-Lee (JWL) or the ideal gas EOS is used.

As pointed out by Børvik et al. [13], parameterization of the C-4 discrete-particle model can be carried out by stipulating that the aforementioned requirement is fulfilled. Specifically, Børvik et al. [13] systematically varied the C-4 discrete-particle model parameters within an

optimization scheme in order to match the experimental (as well as the continuum-level modeling) results of the so-called "***cylinder test***" [19, 20]. Within the cylinder test, an oxygen free high conductivity (OFHC) copper pipe is filled with an HE and the explosive is detonated at one end. This causes the formation of a (transverse) detonation wave and its propagation along the length of the pipe. By monitoring the temporal evolution of the pipe radial displacement/velocity and its spatial distribution along the pipe length, properties of the explosives can be determined and quantified as the parameters of the postulated EOS. For example, for C-4 and the assumed JWL EOS in the form:

$$p = A\left(1-\frac{\omega}{R_1 V_{HE}}\right)e^{-R_1 V_{HE}} + B\left(1-\frac{\omega}{R_2 V_{HE}}\right)e^{-R_2 V_{HE}} + \omega E_{HE} \qquad (3\text{-}8)$$

where p is the pressure, $V_{HE}=\rho_{HE}/\rho_{0,HE}$, E_{HE}/V is the volumetric internal energy density, there are five JWL EOS material-model parameters (A, B, ω, R_1, R_2). These parameters were determined by Børvik et al. [13] using an optimization algorithm coupled with the combined Lagrangian-Eulerian finite-element analysis of the cylinder test and the experimental cylinder-test data by Souers et al. [19]. A list of the values for these parameters can be found in Table 1 of Ref. [13].

To parameterize the C-4 discrete-particle material model, Børvik et al. [13] carried out combined finite-element/discrete-particle simulations within which the OFHC pipe is treated as a continuum-Lagrangian finite-element discretized component (modeled using the Johnson-Cook linear-elastic/strain-hardening/rate-dependent/thermally-softenable-plastic constitutive equation [21]) while C-4 is represented as an ensemble of 1,000,000 discrete particles. Next, within an optimization study, the discrete-particle model parameters are varied systematically until the resulting temporal evolutions and spatial distributions of the pipe radial displacement/velocity (caused by the explosive detonation initiated at one end of the pipe) match the same experimental results as those used for parameterization of the C-4 JWL EOS. The procedure employed by

Børvik et al. [13] yielded the following C-4 discrete-particle material-model parameters: (i) $\rho_{0,HE}$=1601 kg/m^3; (ii) $E_{0,HE}/V$=8.7 GJ/m^3; (iii) γ_{HE}= 7/5 ; and (iv) b_{HE} = 0.35. It should be noted that the values for $\rho_{0,HE}$ and $E_{0,HE}$ / V, as well as the detonation velocity D = 8190 m/s, were taken directly from the JWL-EOS C-4 parameterization carried out by Souers et al. [19]. In other words, parameter-optimization was carried out only for γ_{HE} and b_{HE}.

Air

Air surrounding the target structure and located above the soil is treated as a diatomic ideal gas initially at the ambient pressure (101.3 kPa) and reference temperature (298 K). Following Børvik et al. [13], the four basic discrete-particle model parameters are assigned the following values: (a) $\rho_{0,air}$ = 1.184 kg/m^3; (b) $E_{0,air}$ / V = 0.25325 MJ/m^3; (c) γ_{air} = 7/5; and (d) b_{air} = 0 (no co-volume effects considered). Following the same procedure as in the case of HE detonation products, these parameters are used to determine, at the onset of simulation, the number of the air discrete particles and partitioning of the total internal energy into its kinetic translational and kinetic rotational/vibrational parts. It should be noted that in this case, $e_{s,air}/e_{t,air} = 2/3$ and $e_{s,air}$ is not zero any longer. However, while in an ideal-gas molecular system, $e_{s,air}/e_{t,air}$ acquires this equilibrium value only in a statistical sense, within the present discrete-particle model, the ratio is imposed on each individual particle to reduce the computational cost. It should be further noted that, within the present discrete-particle model for air, $e_{s,air}$ is treated as a scalar variable, i.e. no explicit consideration is given to the rotational/vibrational degrees of freedom of the particles. Since the collision of two air particles is of an elastic character, the momentum and the total kinetic/internal energy are conserved, as well as the $e_{s,air}/e_{t,air}$ ratio. These conditions are used to determine particle velocities following

collision. As far as the collision between an air particle and a movable/deformable structure is concerned, the exchange of the kinetic translational energy between the particle and the structure causes the $e_{s,air}/e_{t,air}$ ratio to depart from its equilibrium value until the particle in question collides with another particle.

It is important to recognize that the constancy of $e_{s,air}/e_{t,air}$ ratio corresponds to the assumption of thermal equilibrium within air. This assumption is justified for air prior to detonation. However, upon detonation, linear momentum transfer from the HE detonation products to air causes the air-molecules/discrete-particles to acquire very large values of their kinetic translational energy (i.e. the condition of thermal equilibrium does not hold any longer).

Soil

While the soil is also modeled using a discrete-particle approach, the soil discrete-particle model differs from those used for the HE gaseous detonation products and air in that soil particle collisions are modeled using a penalty rather than an elastic (or, more precisely, kinematic-elastic) collision algorithm. This was done in order to account for the effects such as: (i) soil-particle finite stiffness; (ii) rate-dependent dissipative/damping nature of the inter-particle collisions; and (iii) the inter-particle frictional effects.

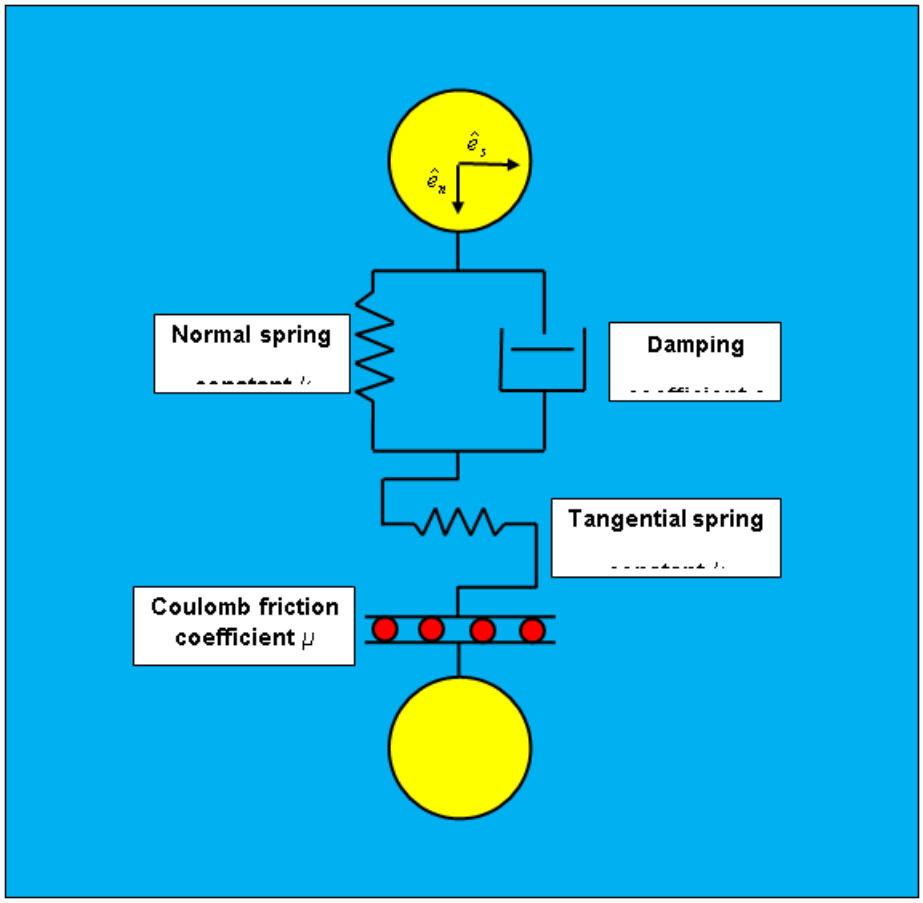

Figure 3–5 A schematic of the contact-mechanics model involving two interacting equal-sized/mass spherical particles of soil.

The essential features of the penalty contact used are depicted schematically in Figure 3-5 which shows a two-particle contact model. Within this model, particle normal interactions are accounted for by a linear spring (with a spring constant k) and a linear dashpot (with a damping coefficient c) connected in parallel. As far as the tangential interactions are concerned, they are modeled using a linear spring (also of stiffness k) and a Coulomb frictional element (which is characterized by a friction coefficient μ and which limits the tangential-spring force). It should be noted that soil-particle fracture processes are not considered since they are associated with minor energy absorption/dissipation effects and, hence, are not expected to significantly affect the computational results. Furthermore, it should be noted that the soil-particle stiffness is not accounted for explicitly since the particles are of a rigid type. Rather, through the proper selection of the stiffness constants of the normal and tangential contact springs, particle stiffness is accounted for implicitly.

As in the case of the HE/air discrete-particle models, only the translational degrees of freedom are considered in the case of the soil discrete-particle model (in order to reduce the computational cost). A limited number of computational analyses in which the rotational degrees of freedom were included show that the results obtained are not greatly affected by the inclusion of soil-particle rotations while the computational cost was greatly increased.

In the present work, both the cases of dry and saturated soil/sand are considered. In the remainder of this section, details are presented regarding the discrete-particle model parameterization for the cases of dry and saturated soil.

Dry Soil: Dry soil is represented using constant radius rigid spherical particles with the particle-material density of 2700 kg/m^3 and the initial particle volume fraction of 0.6 (yielding the soil initial density of 1620 kg/m^3). To fill the soil sub-domain with the particles and to parameterize the contact model, the following three-step procedure is used: (i) the soil sub-domain is first

assumed to be a three-dimensional array of identical unit cells with the periodic boundary conditions being applied across the faces of the unit cells. To determine the initial distribution of the soil particles within the unit cell, the number of particles required to attain a volume fraction of 0.6 are placed in the unit cell while ensuring that no inter-particle penetration takes place. An example of a prototypical soil unit cell is displayed in Figure 3-6; (ii) next, the unit cell is subjected to volumetric compression, and the particle contact stiffness k and the contact damping coefficient c are varied in a systematic manner (while holding the inter-particle friction coefficient at a constant level of μ = 0.15 [22, 23]) until a good match is obtained between the experimentally measured (for prairie sand containing high level of silt and clay) pressure vs. density and the computed pressure vs. density functional relations. More details of this procedure can be found in our recent work [24]. This procedure yielded k = 4 GN/m, c = 0.0 MN.s/m, and μ = 0.15. The hydrostatic pressure within the unit cell is computed by dividing the average force experienced by the unit cell faces by the face surface area; and (iii) the soil sub-domain is constructed by partitioning it into a three-dimensional array of unit cells and filling each cell identically using the particle configuration obtained in (i).

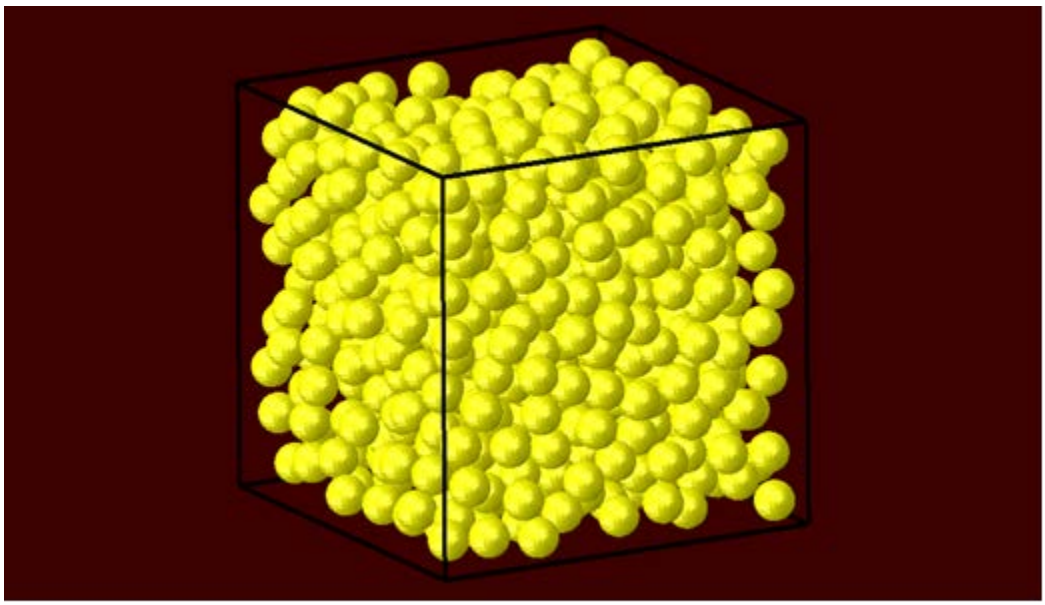

Figure 3–6 Prototypical soil unit cell used in the present combined finite-element/discrete-particle computational analysis of mine detonation and interaction of the detonation products, soil ejecta and air blast with the SBS.

Saturated Soil: In the case of saturated soil, water is not modeled explicitly. Instead, its effect on the distribution and the mechanical response of the soil-particle assembly is accounted for implicitly. Specifically: (a) while keeping the soil-particle size uniform and the particle volume fraction (= 0.6) the same as in the case of the dry soil, the weight of water is accounted for by increasing the saturated-soil density to (0.6 x 2700) + (0.4 x 1000) = 2020 kg/m^3 (yielding the saturated soil-particle effective material density of 2020 / 0.6 = 3367 kg/m^3); (b) to account for an increase in the fully-compacted soil density typically observed in saturated soil, increased particle packing (particle volume fraction = 0.64) was achieved by allowing ±2.5% variations in the soil-particle diameter and by taking advantage of the fact that higher densities are obtained in a system containing particles of non-uniform size. Using the same procedure as above, this yielded the saturated-soil density of (0.64 x 2700) + (0.36 x 1000) = 2088 kg/m^3 and the saturated soil-particle material density of 2088 / 0.64 = 3262 kg/m^3; and (c) inter-particle contact stiffnesses, damping and friction coefficients were adjusted to account for the effect of water by utilizing the aforementioned procedure [24]. Specifically, the damping coefficient

$$c = 2\xi\sqrt{mk} \tag{3-9}$$

is adjusted (by varying the damping ratio ξ, i.e. the ratio of the damping coefficient and the critical damping coefficient) to match the experimental observations [25] that in wet sand, reflection of a compressive shock wave from the soil/air interface does not produce a loose spray of soil particles (an indication of a weaker reflected tensile shock and an increased inter-particle cohesion). This procedure in conjunction with the saturated soil experimental pressure vs. density data [26, 27] yielded k = 40 GN/m, ξ = 0.025 and μ = 0.01.

Selected Discrete-Particle Size-Based Scaling: While keeping the number of soil particles per unit cell constant, the total number of soil particles in the model can be adjusted by changing the

unit cell size. However, it should be noted that the discrete-particle model parameters for soil are particle-/unit-cell-size dependent and, hence, changes in the particle size have to be accompanied by the appropriate changes in the discrete-particle model parameters. Specifically: (a) the particle-particle contact stiffness k scales (linearly) with the particle-/unit-cell-size or dimensions; and (b) under the assumption that the damping ratio is particle-size independent, the damping coefficient c, in accordance with Eq. (3-9), is seen to scale with the squared particle size.

3.3.4. Computational Analysis-Type

The mine blast event and the subsequent interactions between the detonation products, soil ejecta and air blasts with the SBS are analyzed computationally using a finite-element/discrete-particle algorithm. It should be noted that both the discrete-particle and the continuum portions of the computational domain are of a Lagrangian character (i.e. the particle geometry and the finite-element mesh are each attached to the underlying material). Heat dissipation associated with plastic deformation and damage/failure of the SBS is treated as a heat-source. Due to the extremely short duration of the mine-blast detonation event (ca. tens of milliseconds), heat conduction analysis is not carried out. Rather, the purely mechanical analysis is conducted under adiabatic conditions. The effects of local changes in temperature due to adiabatic heating are accounted for through the use of temperature-dependent SBS-material properties.

3.3.5. Initial Conditions

Prior to the beginning of the computational analysis, the continuum-Lagrange sub-domain is occupied by the SBS, while the respective parts of the discrete-particle sub-domain are filled with HE detonation products, soil and the ambient air. The continuum-Lagrangian SBS sub-domain is assumed to be initially stress-free and stationary.

Filling of the discrete-particle sub-domains with air, soil and detonation products was done in the following way: ***Air***: for the selected number of air molecules per discrete particle, $N_{mpp,air}$, and the known values of $\rho_{0,air}$ and V_{air}, the number of air discrete particles, $N_{p,air}$, is computed. These particles are placed randomly within the air computational sub-domain. Next, random velocities are initially assigned to the air particles by sampling the Maxwell-Boltzmann distribution function, Eq. (3-1), with M_{air} = 29 g/mol and T_{air} = 298 K, while ensuring that the v_{rms} of the air discrete-particle model is identical to that found in the ideal gas, ca. 506 m/s, as modeled by the kinetic molecular theory, Eq. (3-2). This condition ensures that the discrete-particle air pressure (=101.3 kPa) is consistent with E_0 / V = 0.25325 MJ/m^3 and γ_{air} = 7/5, in accordance with the ideal gas law; ***Soil***: As far as the soil sub-domain is concerned, it is constructed, as mentioned earlier, by partitioning it into a three-dimensional array of unit cells and filling each unit cell identically while ensuring that no "***penetration***" (other than the one caused by gravity) exists between the neighboring particles; and ***HE detonation products***: In the case of HE, initially stationary particles of undetonated explosive charge are placed randomly within the HE discrete-particle sub-domain following a procedure identical to that used in the case of air particles. Next, the explosive charge is detonated. Within the discrete-particle framework, HE detonation is simulated in the following way. At ***t=0*** (the detonation time), with the exception of the HE located at the detonation point(s), the explosive is assumed to be in the solid state and, as mentioned above, the HE discrete particles are assumed to be at rest (more

precisely, to have a zero average translational velocity). As the detonation front expands, increasingly more HE is detonated, i.e. converted into the gaseous state due to arrival of the detonation front. Once this solid-gas conversion takes place in a region, the HE particles are assigned a velocity by randomly sampling the Maxwell-Boltzmann thermal velocity distribution function, Eq. (3-1) [14], consistent with the $\rho_{C\text{-}4}$ = 1.82 g/cm^3, $M_{C\text{-}4}$ = 222 g/mol and $T_{C\text{-}4}$ = ca. 3500 K, where detonated C-4 is treated as monoatomically decomposed RDX, $C_3H_6N_6O_6$. The sampled velocities are next corrected by dividing them with $(1 - b_{C\text{-}4})^{1/2}$ in order to account for the aforementioned co-volume-induced pressure increase.

3.3.6. Boundary Conditions

Over the portions of the computational-domain external surfaces initially associated with air and soil, an external/ambient pressure of 101.3 kPa is applied so that particles arriving at the boundary and associated with a local pressure exceeding the external pressure are allowed to leave the computational domain. On the other hand, particles which arrive at the external boundary and are associated with a sub-ambient local pressure are reflected back into the domain.

3.3.7. Contact Algorithm(s)

As mentioned earlier, soil/soil particle interactions are modeled using a (viscoelastic/frictional normal/tangential) penalty contact algorithm. On the other hand, HE/HE, air/air, HE/air, soil/HE and soil/air particle interactions are modeled using an elastic/kinematic contact algorithm.

As far as discrete-particle/SBS interactions are concerned, they are modeled using a penalty-contact algorithm. Within this algorithm, contact kinematic constraints are enforced by ensuring that the extent of contact pressure is governed by the local surface penetrations (where the default penalty stiffness parameter is automatically maximized subject to stability limits). As far as the shear stresses are concerned, they are transferred via a "***slip/stick***" algorithm, that is, shear stresses lower than the frictional shear stress are transferred without interface sliding (otherwise interface sliding takes place). The frictional shear stress is defined by a modified Coulomb law within which there is an upper limit to this quantity (set equal to the shear strength of the continuum-Lagrange SBS sub-domain material). The frictional shear stress is then defined as the smaller of the product between the static/kinetic friction coefficient and the contact pressure, on the one hand, and the Lagrangian sub-domain material shear strength, on the other.

3.3.8. Material Model(s)

As mentioned earlier, selected portions of the discrete-particle sub-domain are filled with HE detonation products, soil and air. The constitutive models for these three materials, within the discrete-particle framework, have been presented in Section II.3. It should be recalled that while discrete-particle representation of these three materials is based on rigid particles, material's deformability has been recovered through the use of the appropriate contact algorithms. As far as the continuum-Lagrangian SBS sub-domain is concerned, it was modeled either as a rigid structure or a deformable structure. In the cases when the SBS was modeled as a rigid structure, the material's constitutive model is fully-defined by the mass density (=7850 kg/m^3, for steel). When the SBS was modeled as a deformable structure, it was assumed to be made of conventional AISI 4340 steel whose deformation and failure constitutive response could be represented using the Johnson-Cook material model [28]. A detailed overview of this material model including its AISI 4340 parameterization can be found in our recent work [28, 29].

3.3.9. Computational Algorithm

The governing mass, linear momentum and energy conservation equations are solved with a second-order accurate explicit combined finite-element/discrete-particle algorithm. All the calculations in the present work are carried out by combining a general-purpose mathematical program MATLAB [30] with a customized version of YADE (Yet Another Discrete Element), an extensible, open-source discrete-element method (DEM) computer program [31]. MATLAB was used to create the geometrical/meshed models and Python scripts which control YADE-simulation structure and execution, as well as input/output communications.

3.3.10. Computational Accuracy, Stability and Cost

A standard particle-size and mesh-refinement sensitivity analysis was carried out (the results not shown for brevity) in order to ensure that a convergence of the key results is reached with respect to the further variations of these geometrical/mesh parameters. Due to the conditionally-stable nature of the explicit finite element analysis used, the maximum time increment during each computational step had to be kept lower than the attendant stable time increment. A typical 50 ms computational analysis followed by a detailed post-processing data reduction procedure required on average 24 hours of (wall-clock) time on a 12-core, 3.0 GHz machine with 16 GB of memory.

3.4. Results and Discussion

The three-dimensional combined finite-element/discrete-particle computational model and analysis presented in the previous section are utilized in the present section to reassess the potential of the side channels in lowering the blast momentum/kinetic energy transferred to, and the maximum associated acceleration acquired by, the SBS through the operation of venting and downward-thrust effects. The results obtained are analyzed while comparing them with their combined Eulerian/Lagrangian computational counterparts reported in our recent work [1].

3.4.1. SBS Configurations Analyzed

In order to assess the full blast-mitigation potential of the proposed venting system, and to shed additional light onto the blast-chimney concept, several distinct SBS configurations were examined. The main four among these configurations are shown in Figures 3-7(a)–(d). The SBS configuration shown in Figure 3-7(a) has a V-hull, but no side vent-channels (or the vertical "***through-the-cabin***" vent channel). The V-hulled SBS configuration shown in Figure 3-7(b) contains constant-radius side vent-channels (but no vertical "***through-the-cabin***" vent channel). The V-hulled SBS configuration shown in Figure 3-7(c) is very similar to that shown in Figure 3-7(b) except that the side-vent channels are flared (in their exit section). The V-hulled SBS configuration shown in Figure 3-7(d) has the same side-vent channel configuration as that shown in Figure 3-7(c), but, in addition, contains a vertical vent channel. Comparison of the corresponding results obtained for the four configurations are used to establish the blast-mitigation effects offered by different components of the SBS structure. For example, comparison of the results associated with Figures 3-7(a)–(b) reveals the blast-mitigation effect offered by the side-vent channels, while the corresponding results associated with Figures 3-7(b)–(c) reveal the additional effect provided by channel flaring. Lastly, a comparison of the results associated with Figures 3-7(c)–(d) may offer an insight into the relative blast-mitigation effectiveness of the vertical and side-vent channels. It should also be noted that the configuration displayed in Figure 3-7(c), containing a V-hull and flared side vent channels, is considered as the baseline SBS configuration in the present work.

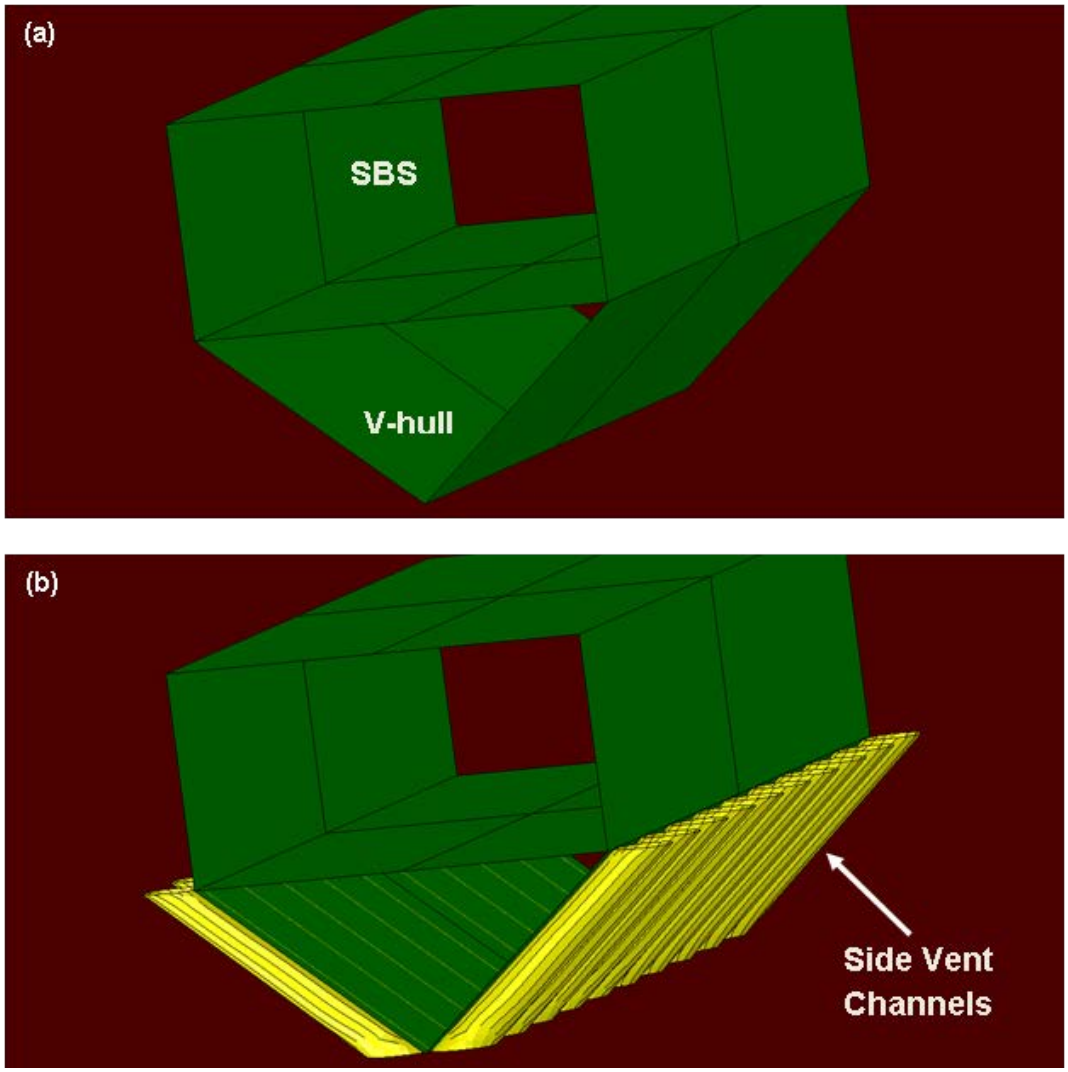

Figure 3–7 Main SBS configurations analyzed in the present work: (a) the plain V-hull configuration; (b) same as (a), but with constant-radius side-vent channels; (c) same as (b), but with channel flaring; and (d) same as (c), but with the addition of a vertical vent channel.

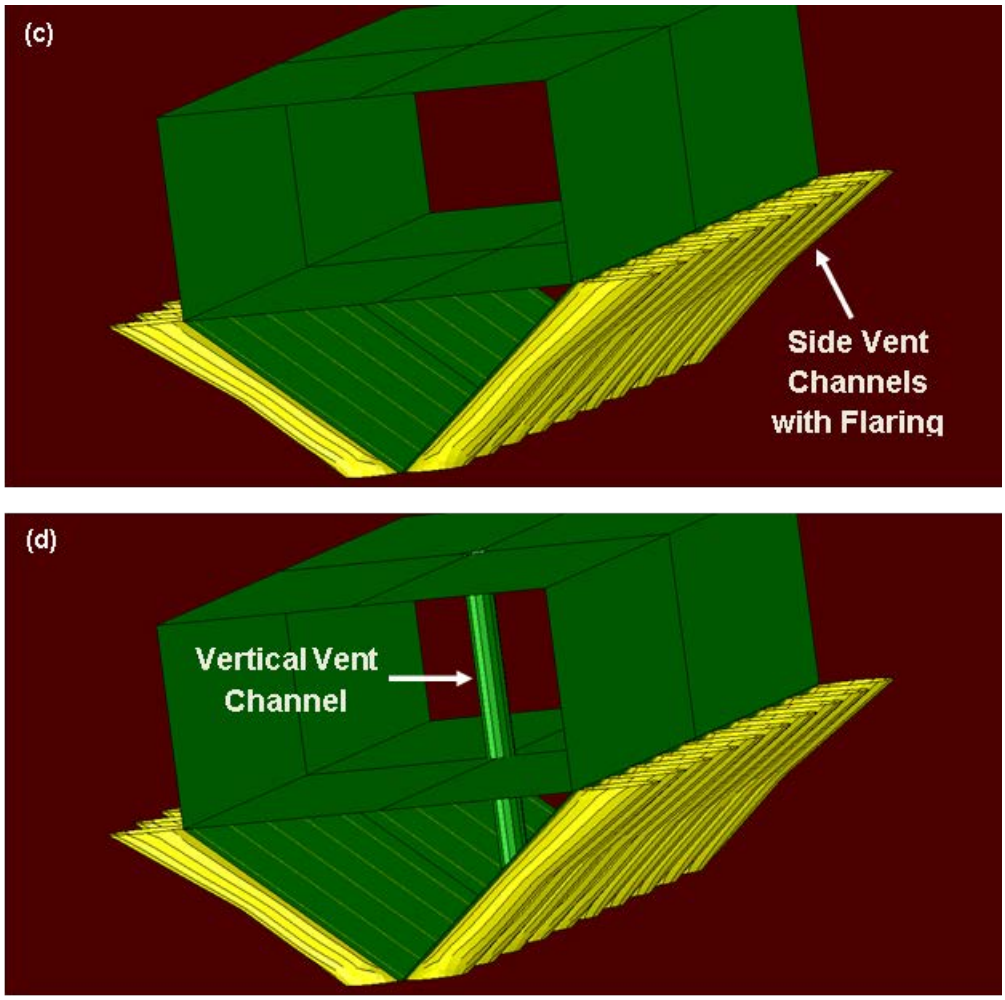

Figure 3-7 Continued.

3.4.2. Prototypical Results

The computational analyses employed yielded the results pertaining to the temporal evolution and spatial distribution of various particle-state and continuum-field quantities such as particles' position, (translational and rotational) particle velocities, particle/particle and particle/continuum-structure interaction forces and moments, etc. In addition, results pertaining to the explosive-charge detonation-induced loading experienced by, and the subsequent response of, the SBS structure were obtained. In the remainder of this section, a few prototypical results are presented and discussed.

Material Distribution and Temporal Evolution - SBS Baseline Case

Spatial distribution of three constituent materials (steel, HE detonation products and soil) at four (2 ms, 4 ms, 6 ms and 8 ms) post-detonation times in the case of the baseline SBS configuration (i.e. the configuration displayed in Figure 3-7(c), containing a V-hull and flared side-vent channels) is shown in Figures 3-8(a)–(d). In these and subsequent figures, for improved clarity, air is removed while the detonation-products and soil-particles are displayed as spheres with the soil-particles having a smaller radius. Furthermore, for the same reason, initial positions of the soil and landmine particles are regularized while the SBS structure is shown as a wireframe. Examination of the results displayed in Figures 3-8(a)–(d) clearly reveals that the presence of side-vent-channels helps guide the flow of the gaseous detonation products and soil-ejecta (as well as air) along the direction parallel with the side of the V-hull. Closer examination of the distribution of the soil and the detonation products within the side-vent-channels reveals that the channels closest to the mine play the dominant role in the blast-venting process. Furthermore, it is seen that the ejected soil initially retains its cohesion and relatively high density, Figure 3-8(a), while at later post-detonation times, ejected soil breaks up into non-bonded particles and acquires a low density, Figures 3-8(c)–(d).

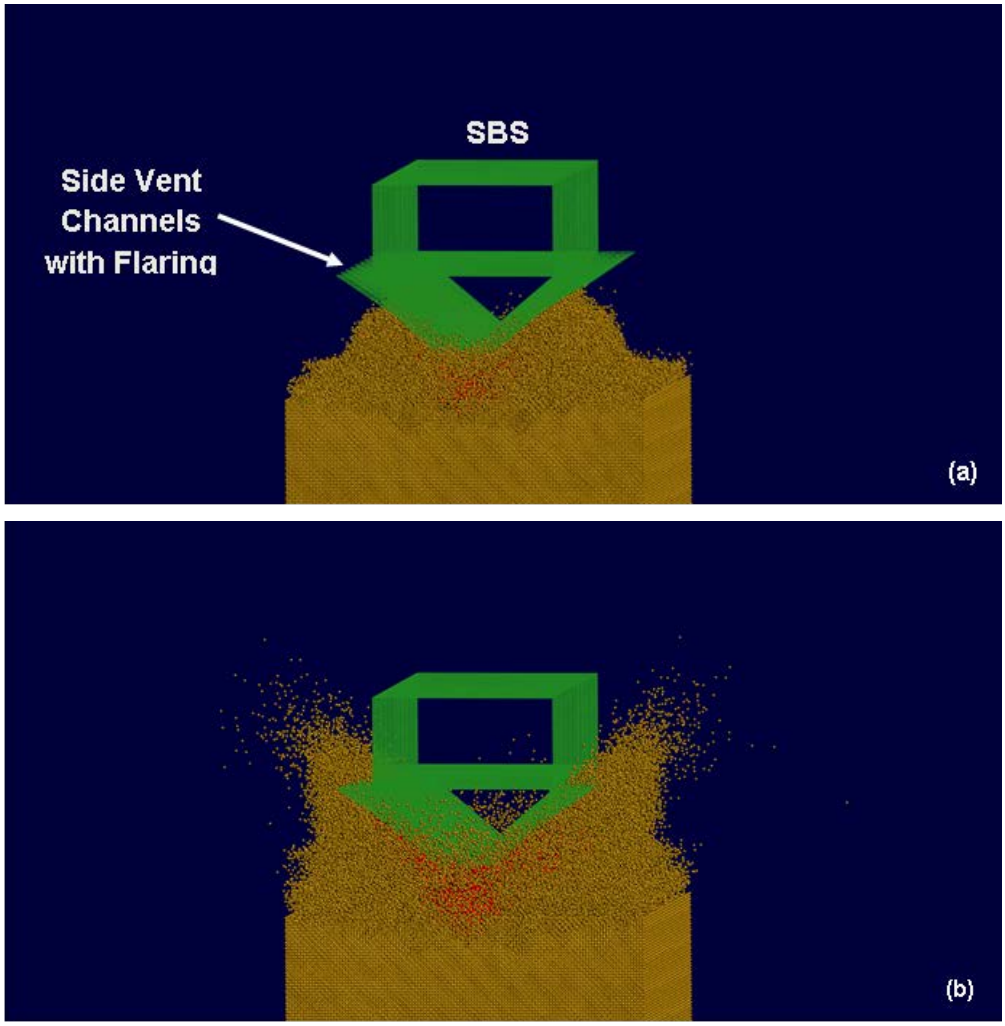

Figure 3–8 Spatial distribution of soil, HE detonation products and steel used to make SBS in the case of the rigid baseline SBS configuration at post-detonation times of: (a) 2 ms; (b) 4 ms; (c) 6 ms; and (d) 8 ms.

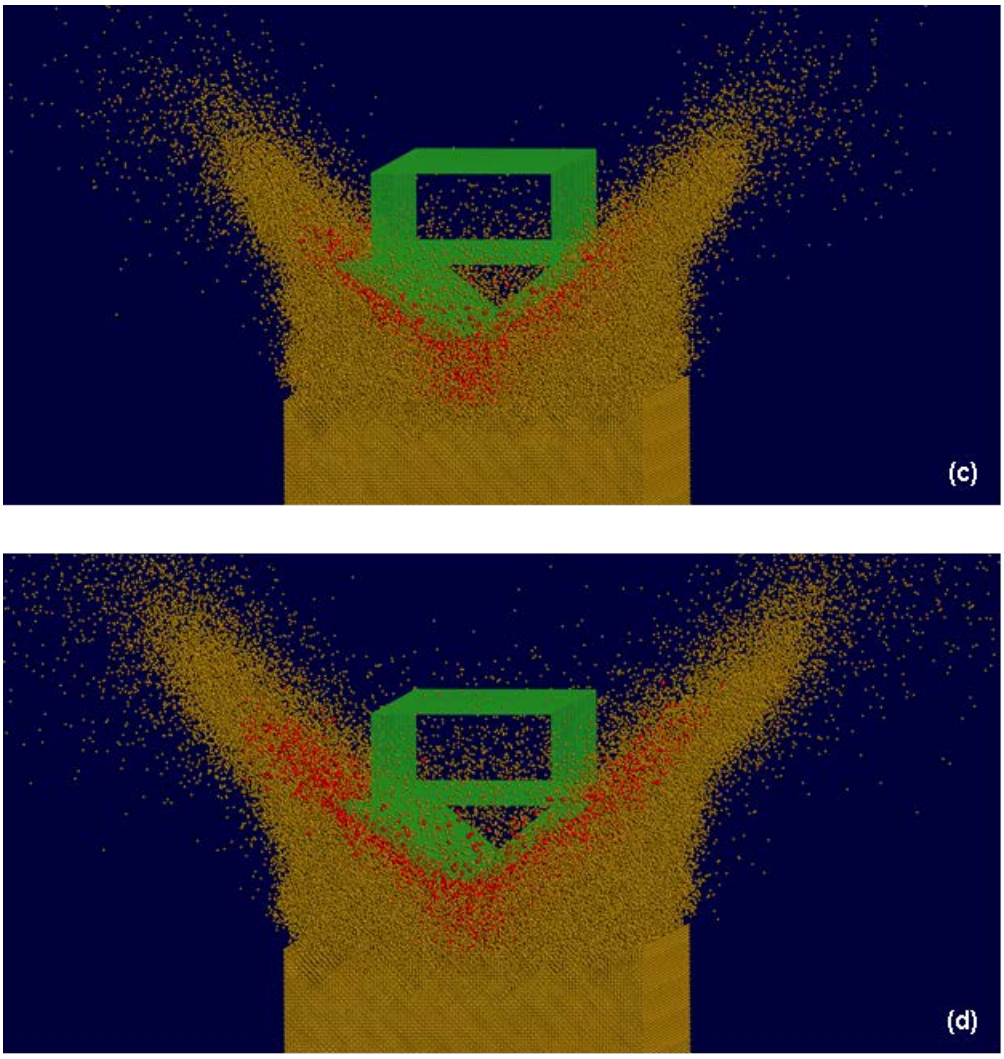

Figure 3-8 Continued.

The Effect of SBS Configuration on Post-Detonation Material Distribution

To further reveal the role of the side-vent channels in mitigating the effect of buried landmine detonation, material spatial distributions at a fixed (12 ms) post-detonation time are shown, respectively, in Figures 3-9(a)–(d) for the case of (a) the SBS configuration without channels; (b) the SBS configuration with constant cross-section channels; (c) the baseline SBS configuration with flared channels; and (d) the SBS configuration with flared channels and a vertical blast-chimney. To help interpretation of the results displayed in these figures, a single double-headed arrow is used in each case to denote a vertical distance of the SBS top from a fixed reference elevation. Examination of the results displayed in Figures 3-9(a)–(d) clearly reveals that the introduction of side-vent-channels, their flaring and ultimate addition of the vertical blast-chimney all help reduce the momentum transferred to the SBS (as visually quantified by the extent of the SBS liftoff). This finding is the result of the increased venting provided by the (flared) side-channels and the blast chimney.

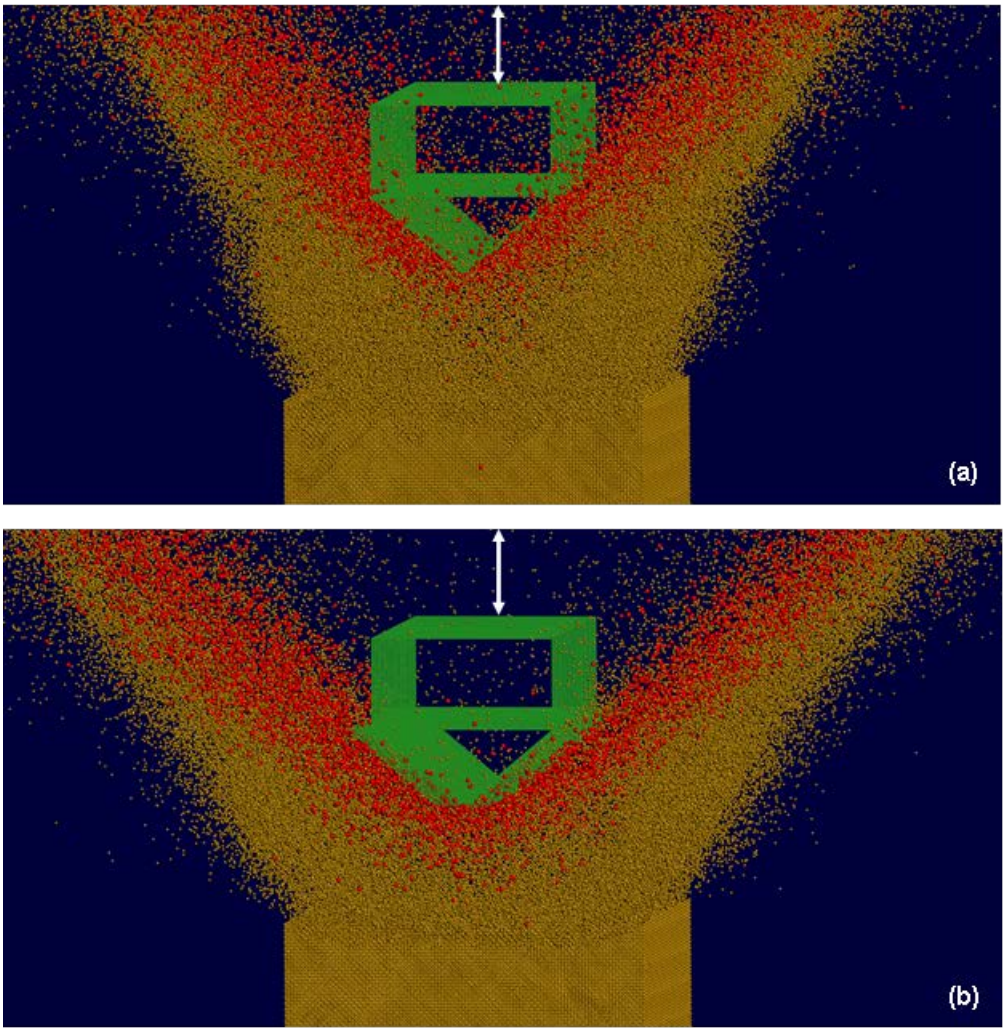

Figure 3–9 Spatial distribution of soil, HE detonation products and steel used to make rigid SBS at a fixed (12 ms) post-detonation time for the case of (a) the SBS configuration without channels; (b) the SBS configuration with constant cross-section channels; (c) the baseline SBS configuration with flared channels; and (d) the SBS configuration with flared channels and a vertical blast-chimney.

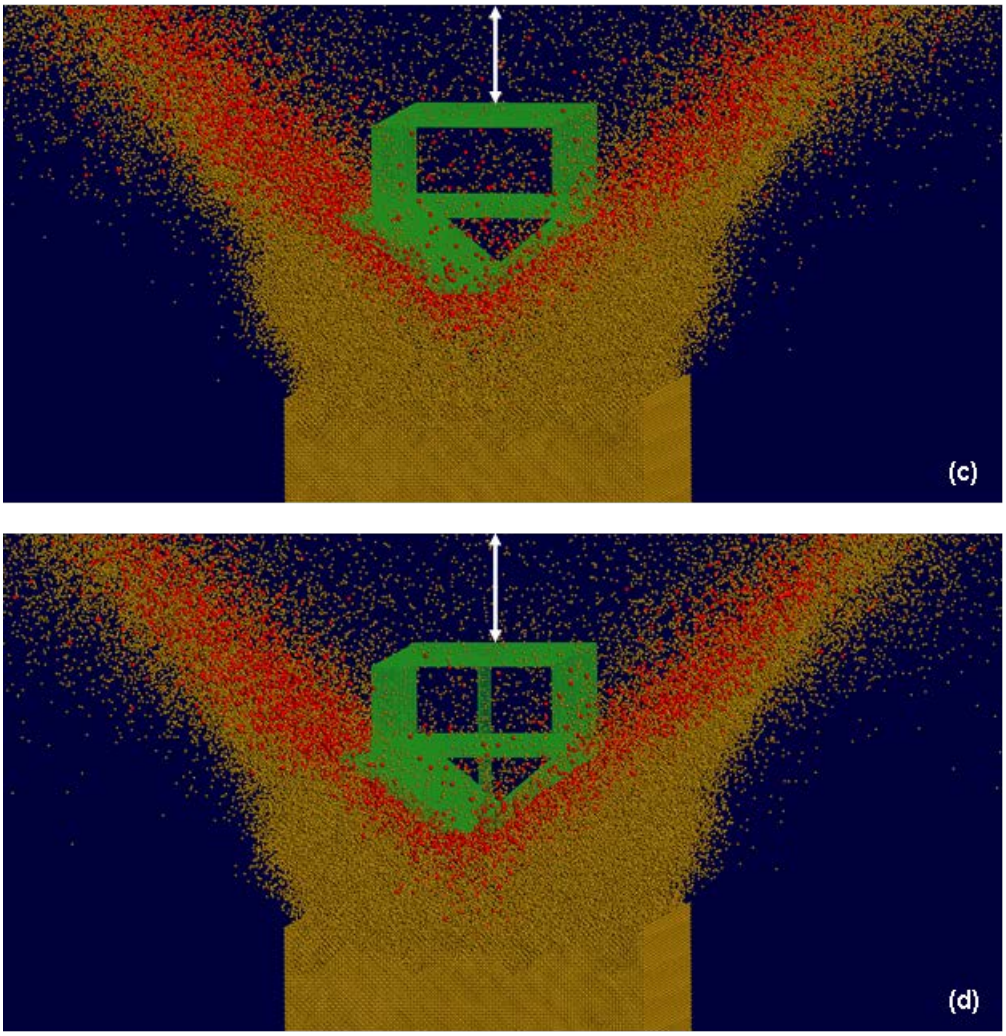

Figure 3-9 Continued.

Particle-Velocity Spatial Distribution and Temporal Evolution - SBS Baseline Case

Spatial distribution of the particle and SBS velocities at four (2 ms, 4 ms, 6 ms and 8 ms) post-detonation times in the case of the baseline SBS configuration is shown in Figures 3-10(a)–(d). Examination of the results displayed in Figures 3-10(a)–(d) clearly reveals: (a) formation of a "***hump***" on the top surface of the soil above the detonated mine, Figure 3-10(a); (b) the onset of formation of a crater within the soil, Figure 3-10(c)–(d); and (c) non-uniform distribution of the particle velocities over the constant-z section of the channels. The velocity non-uniformity is characterized by smaller particle velocities (indicated by the blue or adjacent spectrum colors) in the portions of the channels closer to the V-hull and higher particle velocities (indicated by the red or adjacent spectrum colors) in the portions of the channels farther away from the V-hull. This finding can be rationalized as follows. Interaction of the ejected particles with the portions of the channel walls which are adjacent to the V-hull gives rise to a transfer of upward momentum to the SBS and an associated reduction in the particle (upward) velocities. On the other hand, interaction of the ejected particles with the portions of the channel walls which are away from the V-hull gives rise to a transfer of a downward momentum to the SBS and the associated increase in the particle (upward) velocities.

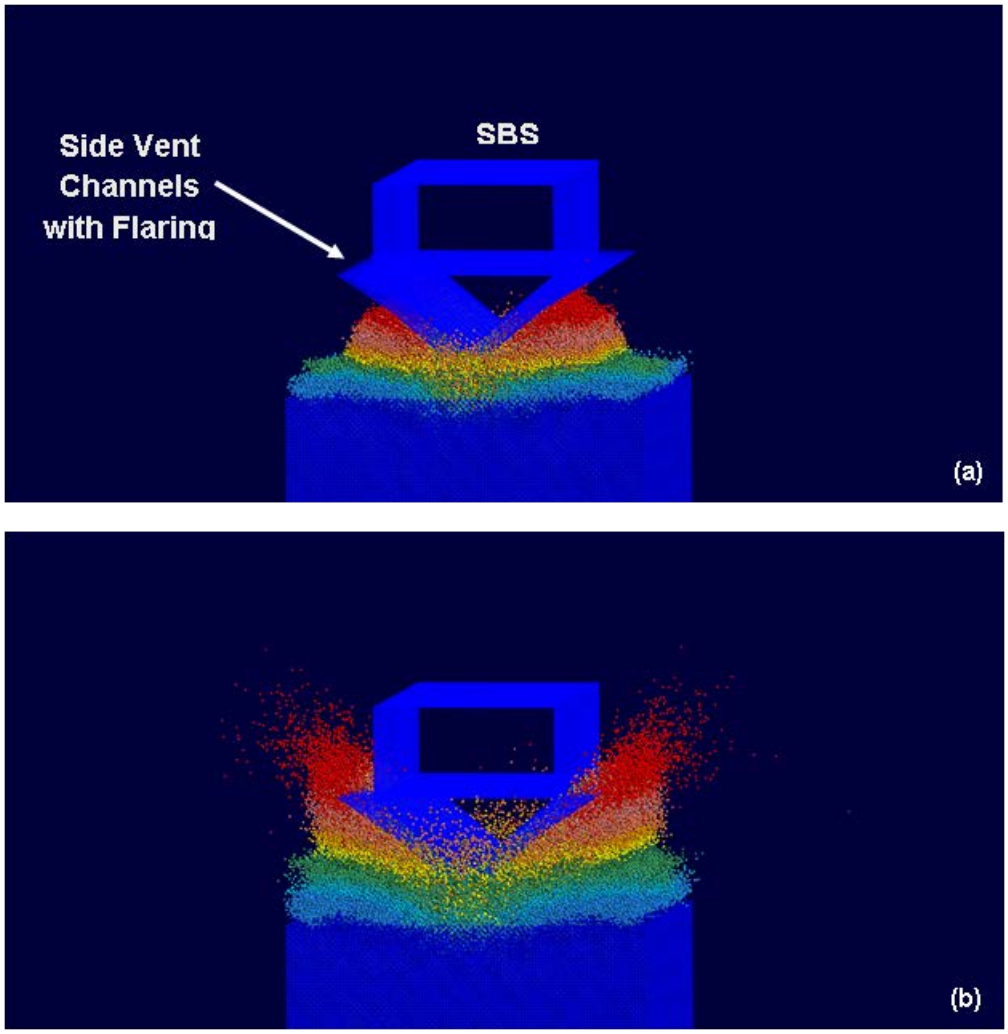

Figure 3–10 Spatial distribution of the velocities of the soil and mine-detonation-product particles and rigidized-SBS in the case of the baseline SBS configuration at post-detonation times of: (a) 2 ms; (b) 4 ms; (c) 6 ms; and (d) 8 ms.

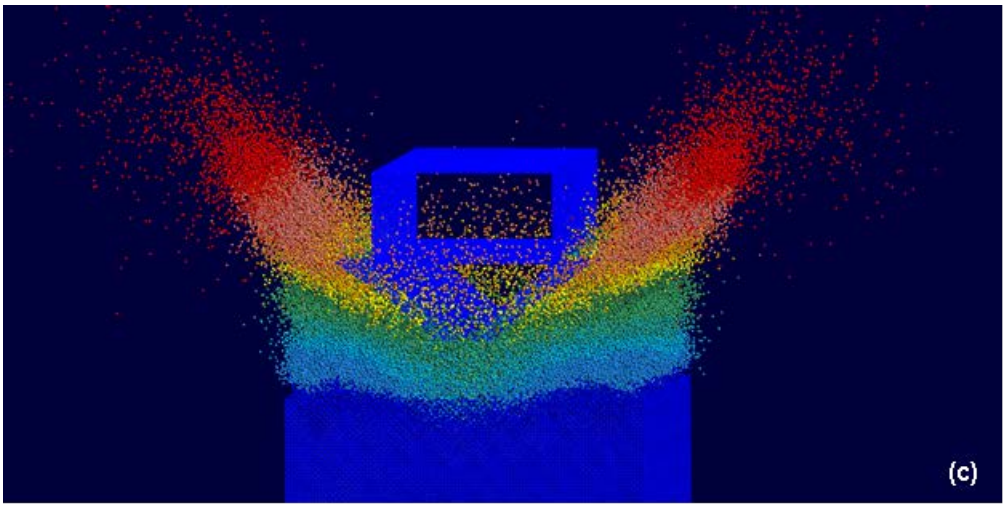

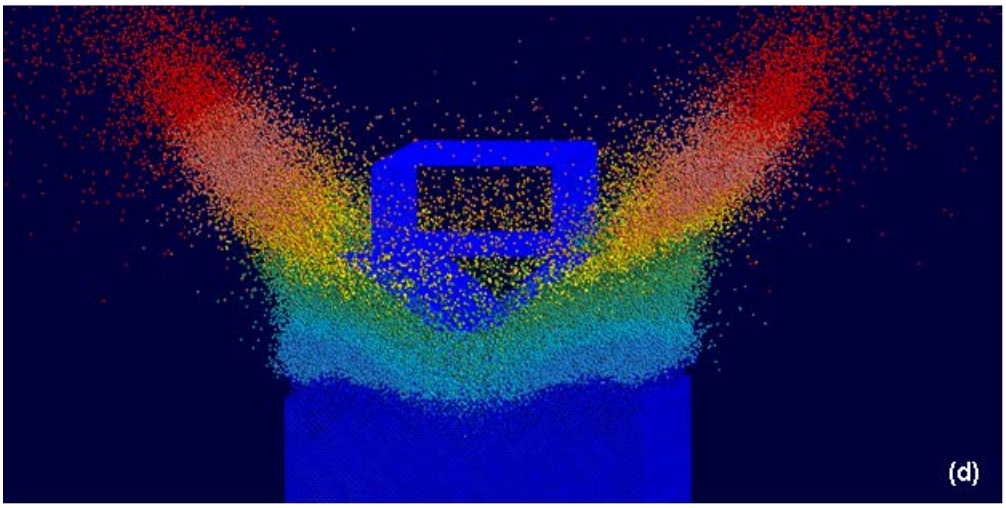

Figure 3-10 Continued.

The Effect of SBS Configuration on Post-Detonation Particle-Velocity Distribution

To further reveal the role of the side vent channels in mitigating the effect of buried landmine detonation, velocity spatial distributions at a fixed (12 ms) post-detonation time are shown, respectively, in Figures 3-11(a)–(d) for the case of (a) the SBS configuration without channels; (b) the SBS configuration with constant cross-section channels; (c) the baseline SBS configuration with flared channels; and (d) the SBS configuration with flared channels and a vertical blast-chimney. Examination of the results displayed in Figures 3-11(a)–(d) clearly reveals that the introduction of side-vent-channels, their flaring and ultimate addition of the vertical blast-chimney all help reduce the momentum transferred to the SBS (as visually quantified by the color-coded SBS velocity). This finding can again be attributed to the increased venting provided by the (flared) side-channels and the blast chimney.

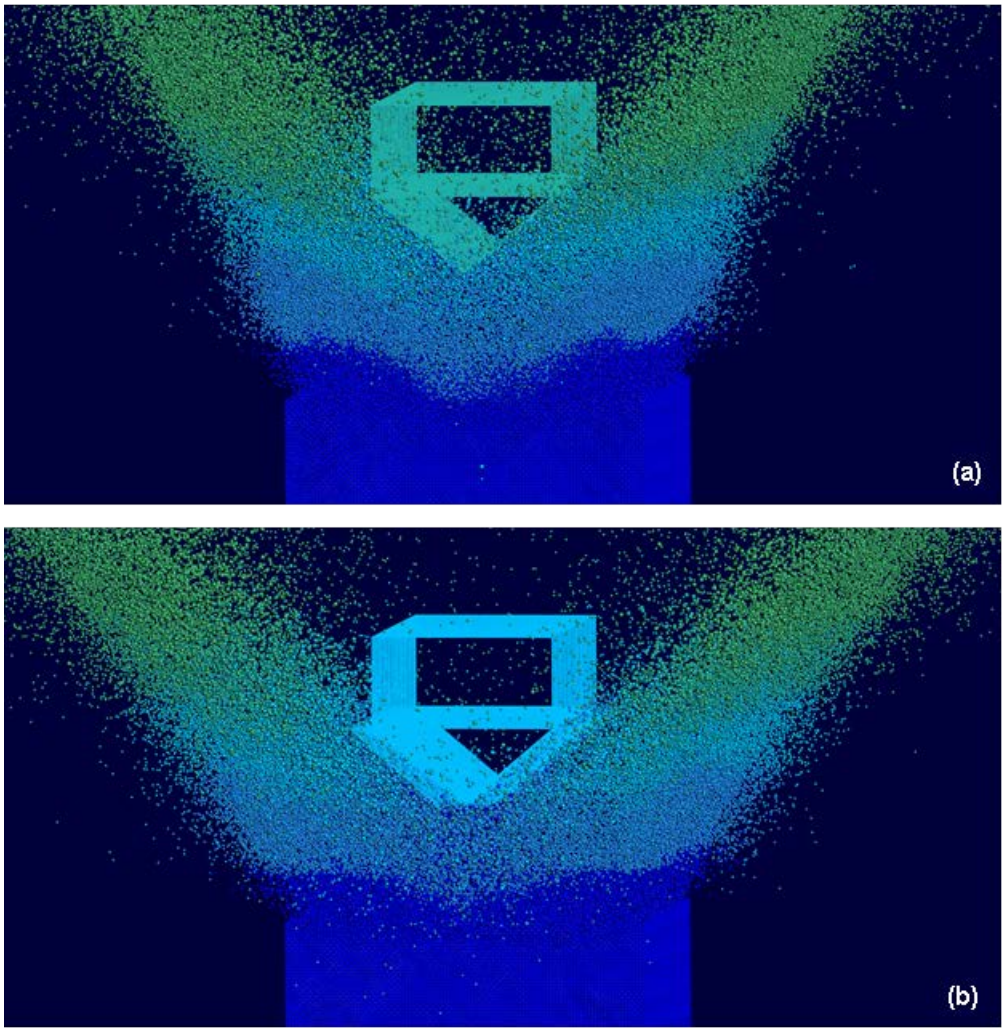

Figure 3–11 Spatial distribution of the velocities of the soil and mine-detonation-product particles and rigidized-SBS at a fixed (12 ms) post-detonation time for the case of (a) the SBS configuration without channels; (b) the SBS configuration with constant cross-section channels; (c) the baseline SBS configuration with flared channels; and (d) the SBS configuration with flared channels and a vertical blast-chimney.

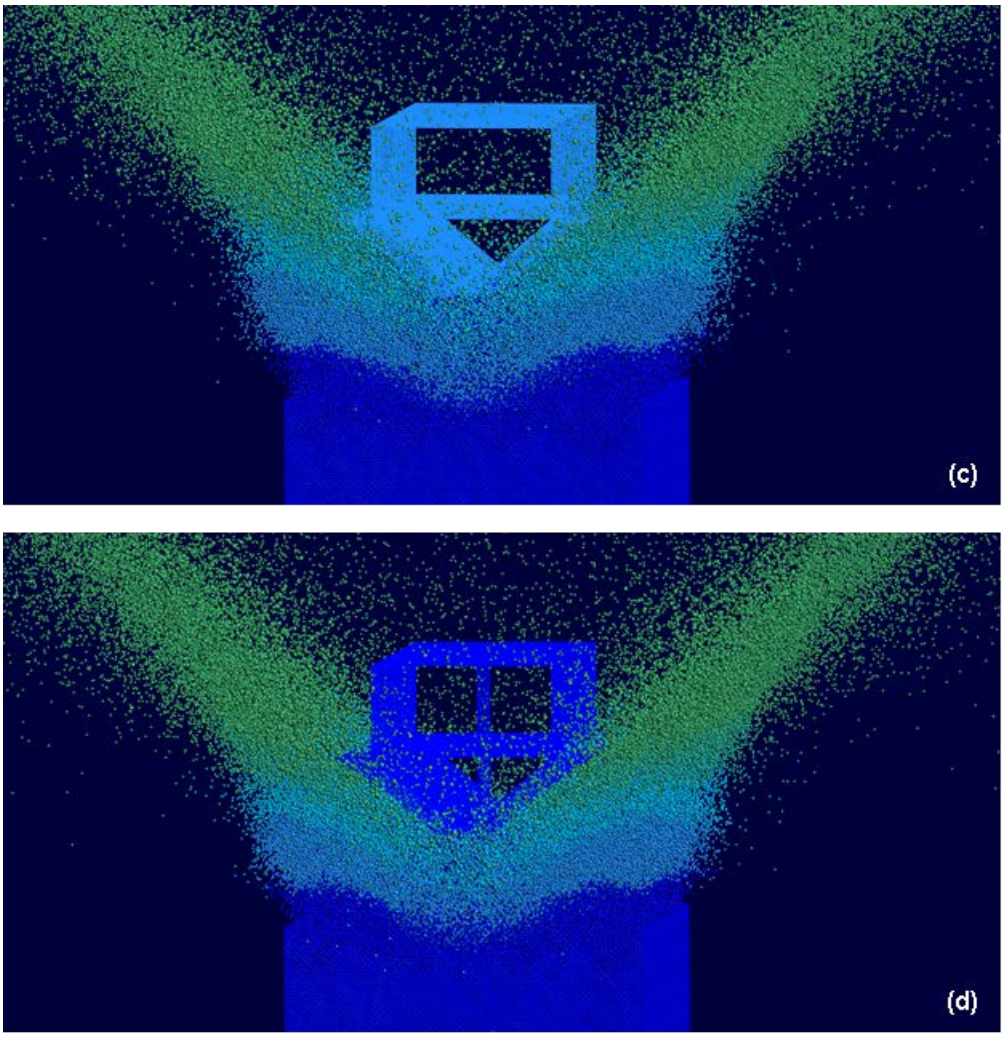

Figure 3-11 Continued.

The Effect of SBS Deformability

All the results presented so far pertain to various cases of rigid SBSs. While the present computational model and simulations enable the inclusion of a deformable SBS, a detailed examination of the effect of the SBS deformability is beyond the scope of the work described in the present manuscript. This topic will be undertaken in our future communication. Nevertheless, in this section we show one of the results that can be obtained by incorporating SBS deformability. Temporal evolutions of the SBS steel material and the associated von Mises stress at four (2 ms, 4 ms, 6 ms and 8 ms) post-detonation times are shown respectively in Figures 3-12(a)–(d). For clarity, discrete particles of the gaseous detonation products, soil and air are not shown in these figures. It is seen that, as a result of the interaction between the gaseous detonation products and soil ejecta with the SBS, the SBS in general and the side-vent-channels, in particular, can undergo severe permanent deformation/distortion and damage/fracture. These phenomena are found to negatively affect the extent of momentum transfer to the SBS and the blast-mitigation efficiency of the side-vent-channel concept and, as mentioned earlier, will be the subject of our future communication.

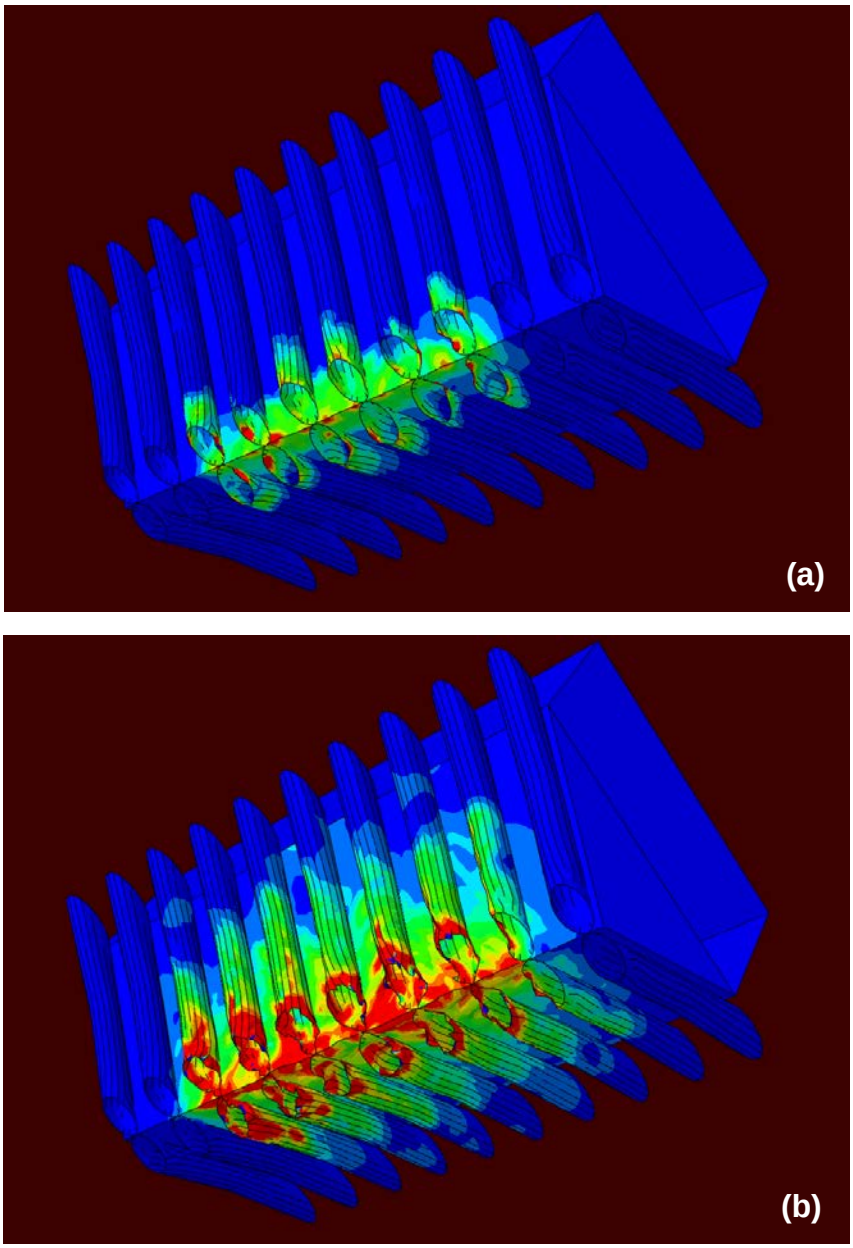

Figure 3–12 Temporal evolutions of the SBS steel material and the associated von Mises stress at post-detonation times of: (a) 2 ms; (b) 4 ms; (c) 6 ms; and (d) 8 ms.

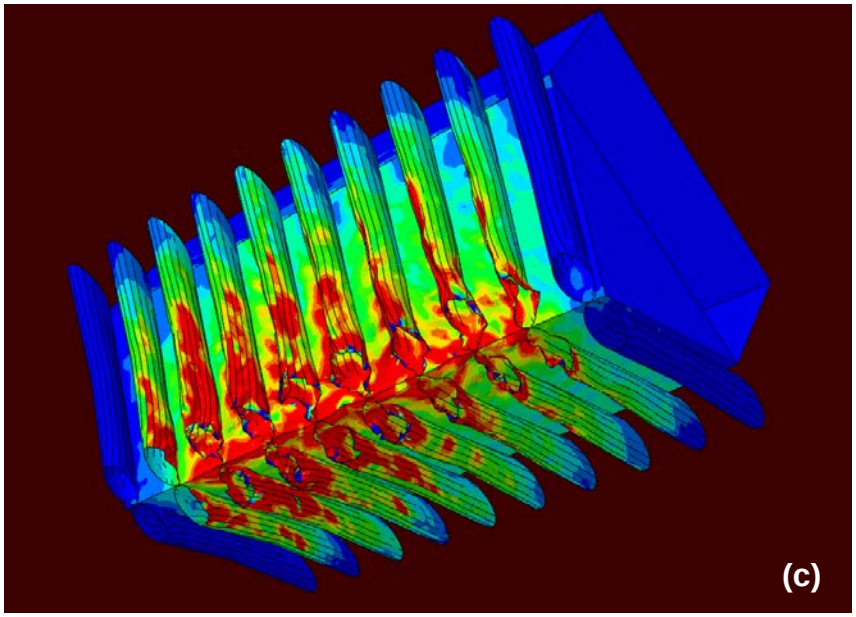

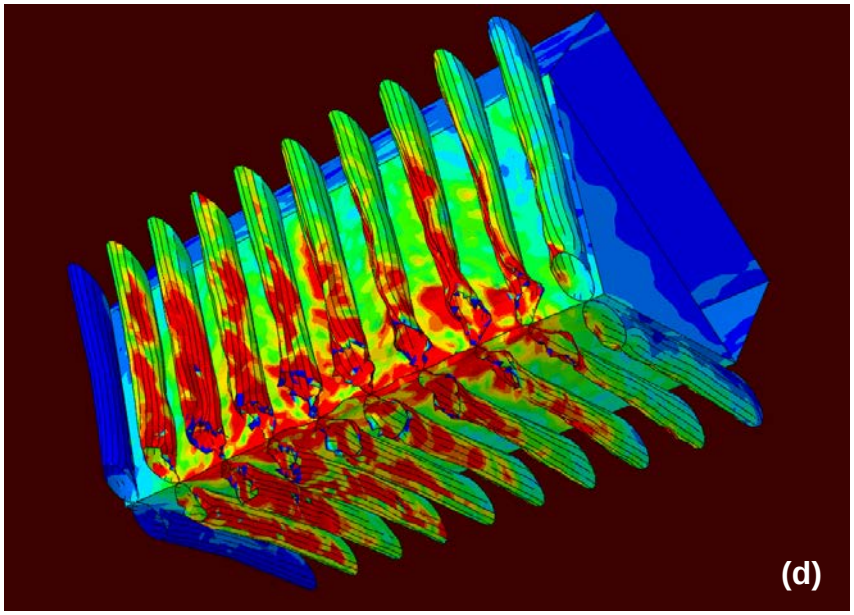

Figure 3-12 Continued.

3.4.3. Blast-Mitigation Efficiency of the Vent-Channel Concept

The results presented in the previous section suggested that the presence of flared side-vent channels may have a positive role in reducing the effect of buried-landmine detonation on the SBS. In this section, more quantitative results pertaining to this blast-mitigation effect of the side-vent channels are presented and discussed.

SBS Velocity and Acceleration Temporal Evolution

Examples of the typical SBS velocity vs. time and SBS acceleration vs. time results obtained in the present work are shown in Figures 3-13(a)–(b), respectively. In both cases, the quantity plotted along the y-axis is normalized by its maximum value while the time is normalized by its value corresponding to the SBS maximum velocity. Examination of the results displayed in these figures shows that the SBS velocity initially experiences a sharp rise, reaches a peak value and then gradually decreases under the influence of gravity. As far as acceleration is concerned, it reaches its peak value much earlier than the velocity and then sharply drops as the additional momentum transfer to the SBS from the detonation products and soil ejecta decreases.

It should be noted that the (non-normalized) results corresponding to the ones displayed in Figures 3-13(a)–(b) are used within a flared-channel design-optimization analysis, presented below, to determine the optimal flared-channel size-geometry which maximizes their blast-venting efficiency.

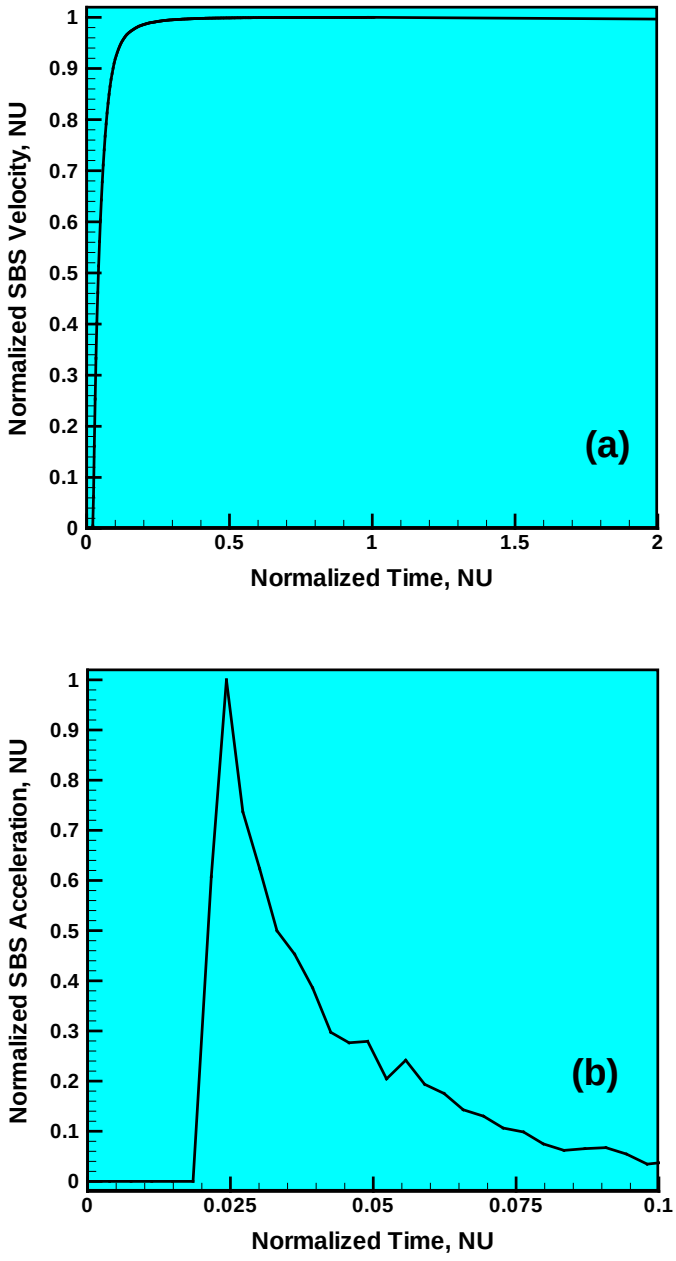

Figure 3–13 Examples of the typical: (a) SBS normalized-velocity vs. time; and (b) SBS normalized-acceleration vs. time results obtained in the present work.

Momentum Transfer

The results of a side-vent channel design-optimization analysis, in which channel inlet area and the channel inlet-to-outlet area ratio are used as design variables, while the total transferred-momentum percent reduction (relative to the SBS case without side channels) is treated as the objective function (to be maximized), are shown in Figures 3-14(a)–(b). The results displayed in Figure 3-14(a) are obtained using the present coupled finite-element/discrete-particle formulation while the ones displayed in Figure 3-14(b) were obtained using the combined Eulerian-Lagrangian formulation, as originally reported in Ref. [1]. The results displayed as contour plots in these figures reveal that: (a) there is a region in the channel inlet area/channel outlet-to-inlet area ratio design space which is associated with positive reductions in the blast momentum transferred to the SBS; (b) both sets of results, however, indicate that these reductions are relatively small (maximum 3.2–3.5%); and (c) the two sets of results are relatively comparable with each other with the present coupled finite-element/discrete-particle formulation predicting somewhat larger (3.5% vs. 3.2%) blast-mitigation effects offered by the side-vent flared-channel concept.

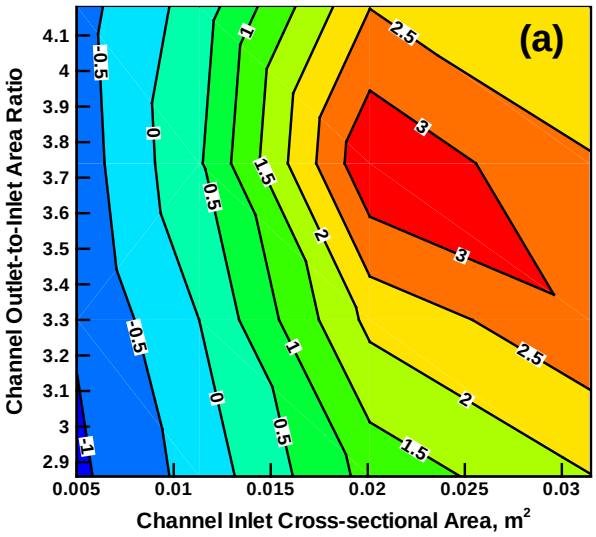

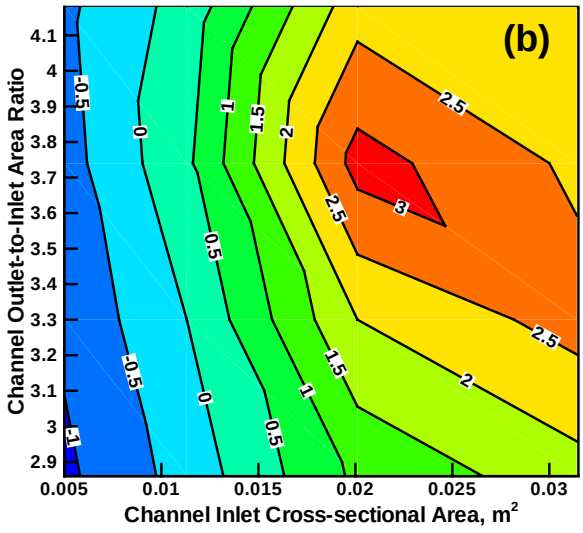

Figure 3–14 Percent reduction (relative to the SBS case without side-vent channels) in total blast momentum for the baseline SBS configuration as a function of channel inlet-area and inlet-to-outlet area ratio: (a) present combined finite-element/discrete-particle analysis; and (b) combined Eulerian/Lagrangian analysis presented in Ref. [1].

It should be noted that, due to the changing geometry and size of the side-vent channels, the SBS mass is not constant within the design space but rather increases both with the channel inlet area and outlet-to-inlet area ratio. Variation of the SBS mass throughout the design space is depicted in Figure 3-15 using a contour plot. A comparison of the results displayed in Figures 3-14(a)–(b) with those displayed in Figure 3-15 reveals that in the portion of the design space in which the transmitted impulse takes on the lowest values, the SBS mass is ca. 9–11% larger than that of the SBS without side channels.

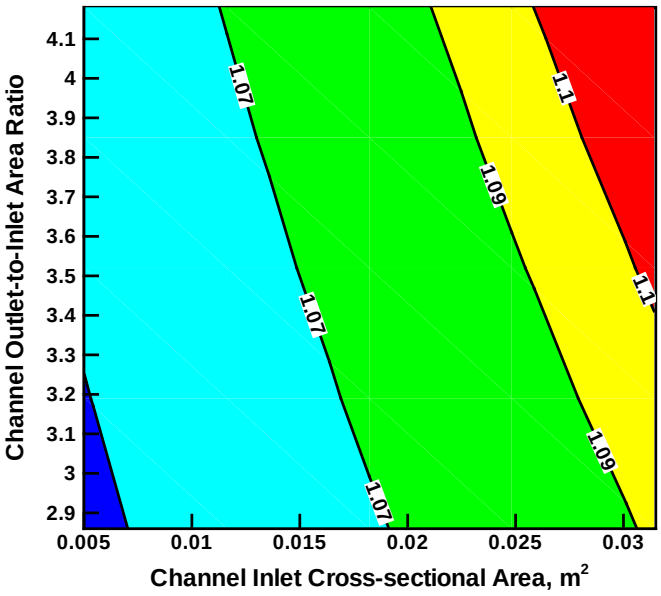

Figure 3–15 Percent increase (relative to the SBS case without side-vent channels) in the mass of the baseline SBS configuration as a function of channel inlet-area and inlet-to-outlet area ratio.

It should be noted that the results displayed in Figures 3-14(a)–(b) correspond to the case of a series of rigid SBSs. In the case of a deformable SBS, the results obtained (but not presented for brevity) show that the fluid-structure interaction effects associated with the SBS deformability initially amplify the blast-mitigation effect. However, the overall reduction in the total momentum transferred to the SBS is not significantly lowered in the case when SBS deformability is taken into account.

Kinetic Energy Transfer

The results of a side-vent channel design-optimization analysis, in which channel inlet area and the channel inlet-to-outlet area ratio are used as design variables, while the total transferred-kinetic energy percent reduction (relative to the SBS case without side channels) is treated as the objective function (to be maximized), are shown in Figures 3-16(a)–(b). The results displayed in Figure 3-16(a) are obtained using the present coupled finite-element/discrete-particle formulation while the ones displayed in Figure 3-16(b) were obtained using the combined Eulerian-Lagrangian formulation, as originally reported in Ref. [1]. The results displayed as contour plots in these figures reveal that: (a) there is a region in the channel inlet area/channel outlet-to-inlet area ratio design space which is associated with positive reductions in the kinetic energy transferred to the SBS; (b) both sets of results, however, indicate that these reductions are relatively small (maximum 5.1–5.5%); and (c) the two sets of results are relatively comparable with each other, with the present coupled finite-element/discrete-particle formulation predicting somewhat larger (5.5% vs. 5.1%) blast-mitigation effects offered by the side-vent flared-channel concept.

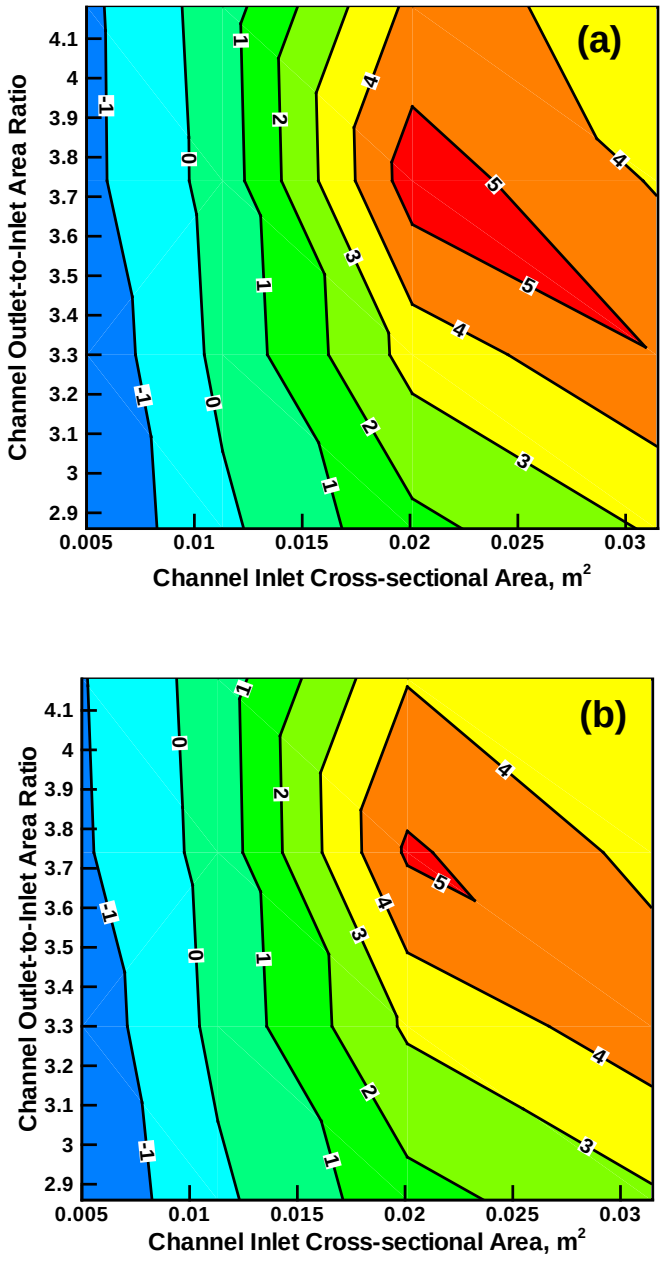

Figure 3–16 Percent reduction (relative to the SBS case without side-vent channels) in total kinetic energy for the baseline SBS configuration as a function of channel inlet-area and inlet-to-outlet area ratio: (a) present combined finite-element/discrete-particle analysis; and (b) combined Eulerian/Lagrangian analysis presented in Ref. [1].

A comparison of the results displayed in Figures 3-14(a)–(b) and Figures 3-16(a)–(b) reveals that regions in the design space that contained maximum reductions in the transmitted impulse and maximum reductions in the kinetic energy, nearly coincide.

It should be again noted that the results displayed in Figures 3-16(a)–(b) correspond to the case of a series of rigid SBSs. The corresponding results (not shown for brevity) obtained for the deformable SBS case show that the overall reduction in the kinetic energy transferred to the SBS, offered by the side-vent channel concept, is not significantly lowered in the case when SBS deformability is taken into account.

SBS Acceleration

The results of a side-vent channel design-optimization analysis, in which channel inlet area and the channel inlet-to-outlet area ratio are used as design variables, while the maximum SBS acceleration percent reduction (relative to the SBS case without side channels) is treated as the objective function (to be maximized), are shown in Figures 3-17(a)–(b). The results displayed in Figure 3-17(a) are obtained using the present coupled finite-element/discrete-particle formulation while the ones displayed in Figure 3-17(b) were obtained using the combined Eulerian-Lagrangian formulation, as originally reported in Ref. [1]. The results displayed as contour plots in these figures reveal that: (a) the largest reduction in the maximum SBS acceleration is obtained in the portion of the design space in which both the channel inlet area and channel outlet-to-inlet area ratio acquire the largest values. This finding is consistent with the fact that: (i) the SBS mass also acquires the largest values in this portion of the design space; and (ii) the SBS acquires a maximum acceleration during the earlier inertia-controlled stages of the blast/SBS interaction; (b) both sets of results, however, indicate that these reductions are relatively small (maximum 1.4–1.6%); and (c) the two sets of results are relatively comparable with each other, with the present coupled finite-element/discrete-particle formulation predicting

somewhat larger (1.6% vs. 1.4%) blast-mitigation effects offered by the side-vent flared-channel concept.

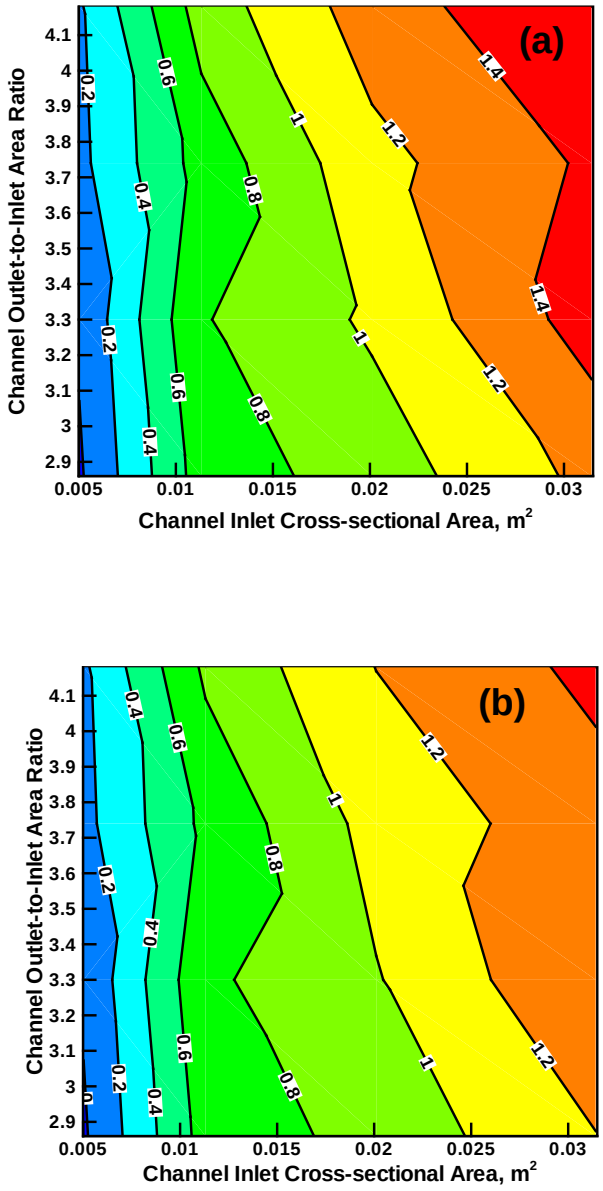

Figure 3–17 Percent reduction (relative to the SBS case without side-vent channels) in maximum acceleration for the baseline SBS configuration as a function of channel inlet-area and inlet-to-outlet area ratio: (a) present combined finite-element/discrete-particle analysis; and (b) combined Eulerian/Lagrangian analysis presented in Ref. [1].

It should be again noted that the results displayed in Figures 3-17(a)–(b) correspond to the case of a series of rigid SBSs. The corresponding results (not shown for brevity) obtained for the deformable SBS case show that the overall reduction in the acceleration transferred to the SBS, offered by the side-vent channel concept, is not significantly lowered in the case when SBS deformability is taken into account.

3.4.4. Additional Effect Offered by Blast Chimney

It should be recalled that the present side-vent channel concept was initially proposed in order to eliminate some of the shortcomings associated with the blast chimney solution. The present results show that relatively small blast-mitigation effects are offered by the side-vent channel concept. On the other hand, some early reports suggested that the blast-chimney concept can yield significant blast-mitigation effects. These reports, however, did not contain technical details and it was not clear to what extent the improved blast-survivability offered by the retro-fitted HMMWV can be attributed to the venting effects offered by the blast chimney and to what extent it is the result of other blast-mitigation solutions (i.e. energy absorbing floor, shock-absorbing seats, a gunner protection system, blast-resistant doors etc.). To assess the blast-mitigation efficacy of the blast chimney, the present coupled finite-element/discrete-particle analysis is extended to the SBS configuration containing a blast chimney, Figure 3-7(d). The results obtained showed that, at a comparable level of the cross-sectional area of the blast chimney and the side-vent channels, reduction in the momentum transferred to the SBS is larger only by a factor of ca. 2 in the case of the SBS configuration shown in Figure 3-7(d), relative to that displayed in Figure 3-7(c). It should be noted that the results reported here correspond to the case when landmine detonation occurred right beneath the blast chimney (the condition which highly favors the blast chimney concept). In a few cases analyzed in which the landmine was not placed right beneath the blast chimney, the blast-mitigation benefits offered by the blast chimney were substantially lower and, in some cases, even lower than those provided by the use of the geometrically optimized flared side-vent-channels. This finding is highly encouraging considering other aforementioned advantages of the side-vent-channel concept over the blast-chimney concept.

3.5. Summary and Conclusions

Based on the results obtained in the present work, the following main summary remarks and conclusions can be drawn:

1. A recently proposed blast mitigation solution based on the use of flared side-vent channels attached to the V-hull is critically assessed using advanced coupled finite-element/discrete-particle computational methods and tools. The solution is motivated by the so-called “blast chimney” concept, which consists of a vertical channel connecting the bottom and the roof and passing through the cabin of a light tactical vehicle.

2. Relative to the blast-chimney concept, the proposed solution offers, at least, the following three advantages: (a) it does not compromise the ease of passenger movement within the cabin space; (b) it does not interfere with the ability of the vehicle occupants to scout their surroundings; and (c) since it does not alter the key structural layout of the vehicle, it is not expected to degrade the vehicle’s structural durability/reliability.

3. To fully assess the blast-mitigation potential of the side-vent channel solution, transient nonlinear dynamics finite-element/discrete-particle analyses of buried landmine detonation and interactions of the soil ejecta, detonation products and air blast with a target structure is combined with a channel-design optimization analysis.

4. The results obtained show that when the side-vent channels are properly optimized (with respect to their inlet area and outlet-to-inlet area ratio) they can increase the reduction in the total momentum transferred to the target structure, and in the total kinetic energy transferred to the target structure, (relative to an identical structure without side-vent channels) by up to 3% and 5%, respectively. As far as the reduction in the maximum acceleration is concerned, it is found to be less sensitive to the design of the side-vent channels, but more sensitive to the overall mass of the target structure.

3.6 References

1. M. Grujicic, B. d'Entremont, J. S. Snipes, and R. Gupta, "***A Novel Blast-Mitigation Concept for Light Tactical Vehicles***," pending approval from sponsor for manuscript submission, February 2012.

2. K. Barry and C. Philpot, "***Humvee for Victory***," Car and Driver, Nov. 2011, 22–23.

3. J. Capouellez, K. Drotleff, G. Wolfe, A. Cichosz, F. Helsel, A. Mikaila, J. R. Pickens , R. W. Semelsberger, S. Kerr, E. Wettlaufer, P. Massoud, J. Wood and B. Barringer, "***Optimized Light Tactical Vehicle***,", 27th Army Science Conference, No. FP-11, 2010, 1–8.

4. K. A. Holsapple and K. R. Housen, "***Crater database and scaling tools***," http://keith.aa.washinton.edu/craterdata, November 2004.

5. P. S. Westine, B. L. Morris, P. A. Cox and E. Polch, "***Development of computer program for floor plate response from land mine explosions***," Contract Report No. 1345, for U.S. Army TACOM Research and Development Center, 1985.

6. B. L. Morris, "***Analysis of Improved Crew Survivability in Light Vehicles Subjected to Mine Blast***," Final Report for Contract No. DAAK70-92-C-0058 for the U.S. Army Belvoir RDEC, Ft. Belvoir, VA, 1993.

7. D. Bergeron, S. Hlady and M. P. Braid, "***Pendulum Techniques to Measure Land Mine Blast Loading***," 17th International MABS Symposium, Las Vegas, USA, June 2002.

8. M. P. Braid, "***Experimental Investigation and Analysis of the Effects of Anti-personnel Landmine Blasts***," Defence R&D Canada, Suffield Special Publication, DRES SSSP 2001-188, December 2001.

9. K. Brannen, "***Blast Chimney Shows Promise, Questions Remain***," Defense News, 22 July 2011, http://www.defensenews.com/story.php?i=7166742

10. K. Brannen, "***'Chimney' Deflects IEDs***," Defense News, 1 November 2010, http://www.defensenews.com/story.php?i=4996368

11. L. Olovsson, A.G. Hanssen, T. Børvik, "***A particle-based approach to close-range blast loading***," European Journal of Mechanics A/Solids, 29, 1–6, 2010.

12. T. Børvik, A.G. Hanssen, M. Langseth, L. Olovsson, "***Response of structures to planar blast loads – A finite element engineering approach***," Computers and Structures, 87, 507–520, 2009.

13. T. Børvik, L. Olovsson, A.G. Hanssen, K.P. Dharmasena, H. Hansson, H.N.G. Wadley, "***A Discrete Particle Approach to Simulate the Combined Effect of Blast and Sand Impact Loading of Steel Plates***," Journal of Mechanics and Physics of Solids, 59, 940–958, 2011.

14. J.C. Maxwell, "***Illustrations of the Dynamical Theory of Gases***," Philosophical Magazine 19, 19–32, 1860.

15. D. Bernoulli, "***Hydrodynamica Sive de Viribus et Motibus Fluidorum Commentarii***," Johannis Reinholdi Dulseckeri. Argentorati, Strasbourg, 1738.

16. D. Bernoulli and J. Bernoulli, "***Hydrodynamics***," Dover Publications, 1968.

17. V.F. Baibuz, V.Y. Zitserman, L.M. Golubushkin, I.G. Malyshev, "***The co-volume and equation of state of high-temperature real gases***," Journal of Engineering Physics and Thermo-physics, 51, 955–956, 1986.

18. Clausius, R. "***Ueber das verhalten der kohlensaüre in bezug auf druck, volume und temperature***," Annalen der Physik und Chemie 3, 337–357, 1880.

19. P.C. Souers, B. Wu, L.C. Haselman Jr., "***Detonation equation of state at LLNL, 1995. Report UCRL-ID119262 Rev 3***," Energetic Materials Center, Lawrence Livermore National Laboratory, Livermore, CA, USA, 1996.

20. P.C. Souers, "***Cylinder test on C-4. Report UCRL-TR-230845***," Energetic Materials Center, Lawrence Livermore National Laboratory, Livermore, CA, USA, 2007. https://e-reports-ext.llnl.gov/pdf/347222.pdf [accessed on November 24, 2012]

21. K.J. Frutschy, R.J. Clifton, "***High-temperature pressure-shear plate impact experiments on OFHC copper***," Journal of the Mechanics and Physics of Solids, 46, 1723–1743, 1998.

22. M. Grujicic, B. Pandurangan, J. D. Summers, B. A. Cheeseman and W. N. Roy, "***Application of the Modified Compaction Material Model to Soil with Various Degrees of Water Saturation***," Shock and Vibration, 15, 79–99, 2008.

23. M. Grujicic, B. Pandurangan, G. M. Mocko, S.T. Hung, B. A. Cheeseman, W. N. Roy and R. R. Skaggs, "***A Combined Multi-Material Euler/Lagrange Computational Analysis of Blast Loading Resulting from Detonation of Buried Landmines***," Multidiscipline Modeling in Materials and Structures, 4, 105–124, 2008.

24. M. Grujicic, R. Yavari, J.S. Snipes, S. Ramaswami, "***Extension of a Current Continuum-Level Material Model for Soil into the Low-Density Discrete-Particle Regime***," Journal of Materials Engineering and Performance, in press. DOI: 10.1007/s11665-012-0429-3

25. V. S. Deshpande, R. M. McMeeking, H. N. G. Wadley and A. G. Evans, "***Constitutive Model for Predicting Dynamic Interactions between Soil Ejecta and Structural Panels***," Journal of Mechanics and Physics of Solids, 57, 1139–1164, 2009.

26. M. Grujicic, B. Pandurangan and B. A. Cheeseman, "***The Effect of Degree of Saturation of Sand on Detonation Phenomena Associated with Shallow-buried and Ground-laid Mines***," Shock and Vibration, 13, 41–62, 2006.

27. M. Grujicic, B. Pandurangan, Y. Huang, B. A. Cheeseman, W. N. Roy and R. R. Skaggs, "***Impulse Loading Resulting from Shallow Buried Explosives in Water-saturated Sand***", Journal of Materials: Design and Applications, 221, 21–35, 2007.

28. M. Grujicic, W. C. Bell, G. Arakere, I. Haque, "***Finite Element Analysis of the Effect of Up-armoring on the Off-road Braking and Sharp-turn Performance of a High-Mobility Multi-purpose Wheeled Vehicle (HMMWV)***", Journal of Automobile Engineering, 223, D11, 1419–1434, 2009.

29. M. Grujicic, V. Sellappan, M. A. Omar, N. Seyr, A. Obieglo, M. Erdmann and J. Holzleitner, "***An Overview of the Polymer-to-Metal Direct-Adhesion Hybrid Technologies for Load-Bearing Automotive Components***", Journal of Materials Processing Technology, 197, 363–373, 2008.

30. MATLAB, ***The Language of Technical Computing***, Version 8.0.0.783, R2012b (The MathWorks Inc., MA).

31. Yade: V. Šmilauer, E. Catalano, B. Chareyre, S. Dorofeenko, J. Duriez, A. Gladky, J. Kozicki, C. Modenese, L. Scholtès, L. Sibille, J. Stránský, and K. Thoeni, ***Yade Documentation*** (V. Šmilauer, ed.), The Yade Project, 1st ed., 2010. http://yade-dem.org/doc/

CHAPTER 4: SHAPE/SIZE OPTIMIZATION OF SIDE-VENT-CHANNELS SOLUTION FOR IMPROVED LIGHT-TACTICAL-VEHICLE SURVIBABILITY TO BENEATH-UNDERBDY SHALLOW-BURIED MINE DETONATION

4.1. Abstract

The subject of the present work is a design-optimization analysis of our recently proposed side-vent-channel concept/solution for mitigation of the blast-loads resulting from a shallow-buried mine detonated underneath a light tactical vehicle. The concept/solution involves the use of side-vent-channels attached to the V-shaped vehicle underbody, and was motivated by the ideas and principles of operation of the so-called "***pulse detonation***" rocket engines. By proper shaping and sizing of the side-vent-channels, venting of ejected soil and supersonically-expanding gaseous detonation products is promoted in order to generate a downward thrust on the targeted vehicle. The utility and the blast-mitigation capacity of this concept were examined in our prior work using different (i.e. coupled Eulerian/Lagrangian and coupled finite-element/discrete-particle) computational methods and tools. In the present work, an attempt is made to optimize the geometry and size of the side-vent-channel solution for the maximum blast-mitigation performance (as defined by a tradeoff between the maximum reductions in the detonation-induced total momentum transferred to, and the acceleration acquired by, the target vehicle).

4.2. Introduction

In the present work, the recently proposed side-vent-channel-based solution [1, 2] for improved survivability of light tactical military vehicles to beneath-underbody shallow-buried mine detonation has been analyzed within a design-optimization framework. Therefore, the main topics to be overviewed in the remainder of this section include: (a) identification of the main limitations of recently and currently employed light tactical vehicles; (b) examination of the phenomena and processes associated with the interaction of the soil ejecta and gaseous detonation products, resulting from the detonation of shallow-buried mines, with the target structure, and elucidation/quantification of the resulting impulse loading; and (c) a brief overview of the side-vent-channel-based blast-mitigation concept, and of the computational methods and tools used in our prior work [1, 2] in order to establish the blast-mitigation utility and capacity of the solution. As far as the engineering-analysis and design-optimization methods and tools used during identification of an optimal design of the side-vent-channels solution are concerned, they will be presented in Sections II and III, respectively.

Limitations of the Current Tactical Vehicles: The High Mobility Multipurpose Wheeled Vehicle (HMMWV), Figure 4-1(a) [3], is the prototypical light tactical vehicle which has been used by the US military for over 20 years. This vehicle was originally developed and deployed for conventional military conflict with well-defined frontlines, and was intended for use behind the frontline. Consequently, and not surprisingly, the recent and the ongoing asymmetric warfare, in which the distinction between frontline combat and transportation convoys has been severely blurred [4, 5], has revealed the lack of necessary blast and ballistic resistance of the HMMWV. These shortcomings of the HMMWV are the reason that bigger, heavier MRAP (Mine Resistant Ambush Protected) vehicles, Figure 4-1(b) [6] have mostly replaced HMMWVs in the past

conflict in Iraq and the ongoing conflict in Afghanistan. However, the improvements in IED (Improvised Explosive Devices) blast-resistance of MRAP vehicles have come with new limitations, including: (a) reduced tactical mobility/utility; (b) limited maneuverability on crowded city streets; (c) inferior fuel economy; and (d) significantly reduced deployability (these vehicles are too heavy to be driven over 70% of the world's bridges [7]) and transportability (the MRAP vehicle weight typically exceeds the payload capacity of the CH-47 Chinook helicopter).

Figure 4–1 Typical light tactical vehicles currently used by the US military: (a) High Mobility Multipurpose Wheeled Vehicle (HMMWV) [3]; and (b) Mine Resistant Ambush Protected (MRAP) vehicle [6].

Mine-Detonation-Induced Impulse Loading on Target Structures: Landmines buried in or near roads have resulted in numerous instances of tactical vehicle destruction and soldier casualties incurred by the U.S. military during the recent/ongoing campaigns in Iraq and Afghanistan. When these landmines detonate, the impact of the resulting blast waves, ejected soil, mine casing/shrapnel, and expanded gaseous detonation products produces large impulsive loads on the targeted vehicle/personnel. Development of military vehicles (and general structural platforms) with a high-level of resistance/survivability to landmine-/IED-detonation entails at least the following: (a) the understanding of and ability to quantify the impulsive loads associated with the detonation of landmines buried/deployed in soil of differing compositions/constitutions [8–14]; and (b) the ability to predict the kinematic and structural (including failure) response of the targeted vehicles/platforms [15–19]. Acquiring such understanding and predictive ability, however, is typically quite challenging since the detonation-induced loads depend strongly on the deployed mine's shape, size and depth of burial (DOB), the distance between the soil surface and the target (the so-called stand-off distance, SOD), and the soil properties (density, particle mean size and distribution, presence of inorganic/organic matter, water content, etc.).

Due to the sensitive nature of the subject matter, only a few scientific papers and technical reports dealing with the problem of detonation of buried (explosive) charges and the resulting impulse loading experienced by the target structure are publicly available. Among these reports, the following appear to be the most closely related to the work described in the present manuscript: (a) Westine et al. [17] conducted a series of experiments in which an anti-tank landmine was simulated using a buried charge, above which a plate was fixtured and centered. The plate was perforated at different radial distances and plugs of known mass were placed in the holes. These plugs were expelled under blast-loading resulting from detonation of the charge,

with the local impulsive loading on the plate determined from the plug (maximum) velocity; (b) the experimental approach and findings of Westine et al. [17] were used by Morris [18] as a basis for the development of a computer code aimed at assisting the design of mass-efficient, blast-survivable vehicles/structures; (c) Bergeron et al. [19] constructed an instrumented ballistic pendulum and employed it to quantify mine-detonation-induced loads experienced by a target structure as a function of the detonation-event parameters such as: (i) mine size and shape; (ii) detonator location/type; (iii) DOB; (iv) SOD; and (v) soil constitution/moisture-content, etc. In the work of Bergeron et al. [19], the following impulse-loading-related quantities were determined/quantified: (i) the time-dependent pressure and impulse at several locations in air directly above the mine; (ii) the time-dependent pressure and impulse at several locations in the soil surrounding the mine; and (iii) the time-evolution of the associated soil cratering and ejection phenomena (as revealed by the use of x-radiographs and high speed photographs); (d) Braid [20] improved the instrumented ballistic pendulum of Bergeron et al. [19], and used it to quantify impulse loading over substantially larger ranges of the aforementioned detonation-event parameters; (e) Taylor et al. [21] employed the so-called vertical impulse measurement fixture (VIMF) to carry out large-scale experiments aimed at accurately measuring the vertical impulse-loads produced by the detonation of explosive charges (weighing up to 8 kg) buried, to different DOB, in soil of different constitution/moisture-content. The VIMF is a structural mechanical device that enables direct experimental determination of the imparted blast-loading impulse via measurements of the vertical displacement of a known fixed-mass vertical guide rail that is capped with a witness plate, which serves as a momentum trap (i.e. a trap which captures the blast loading of the buried charge); and (f) Wenzel and Hennessey [22] carried out a multi-scale experimental investigation of models of military-vehicle-hull floor-plates (of various sizes)

subjected to impulse and high-pressure loads associated with detonation of charges shallow-buried in soil under the (properly-scaled) vehicle hull. The results obtained were used by Wenzel and Hennessey [22] to conduct a dimensional analysis based on the so-called Buckingham Π-theorem [23]. This type of analysis is commonly employed in situations in which full-scale structures/prototypes are designed and sized based on the results yielded by small-scale model tests.

The Side-Vent-Channel Blast-Mitigation Concept: To address the limitations of light tactical vehicles mentioned above, the US military continues to seek innovative concepts and solutions which: (a) can improve blast-survivability of these vehicles; and (b) do so without compromising vehicle mobility/maneuverability, transportability, deployability or fuel economy. One of the concepts currently being used in the light tactical vehicles is the V-shaped vehicle hull (or simply V-hull). The two most common renditions of the V-hull are depicted schematically in Figures 4-2(a)–(b). In the case of the standard V-hull solution, Figure 4-2(a), the blast-mitigation performance (as measured by the reduction in the momentum transferred to the vehicle by the gaseous detonation products, soil ejecta and mine casing) is improved as the V-hull is made steeper. However, the maximum steepness is constrained by the requirements related to the minimum acceptable vehicle ground clearance and the maximum acceptable cabin-floor height. In the case of the truncated V-hull design, Figure 4-2(b), V-hull steepness is increased at the expense of introducing a flat bottom portion of the V-hull. Due to the tradeoff between the benefits (i.e. decreased blast impulse) offered by the increased steepness of the V-hull and the penalty (i.e. increased blast impulse) incurred due to the introduction of a small flat section, and depending on the location of the detonated mine or IED, this design may or may not result in an

improved blast-mitigation performance relative to that offered by the standard V-hull design (both associated with the same vehicle ground clearance and cabin-floor height).

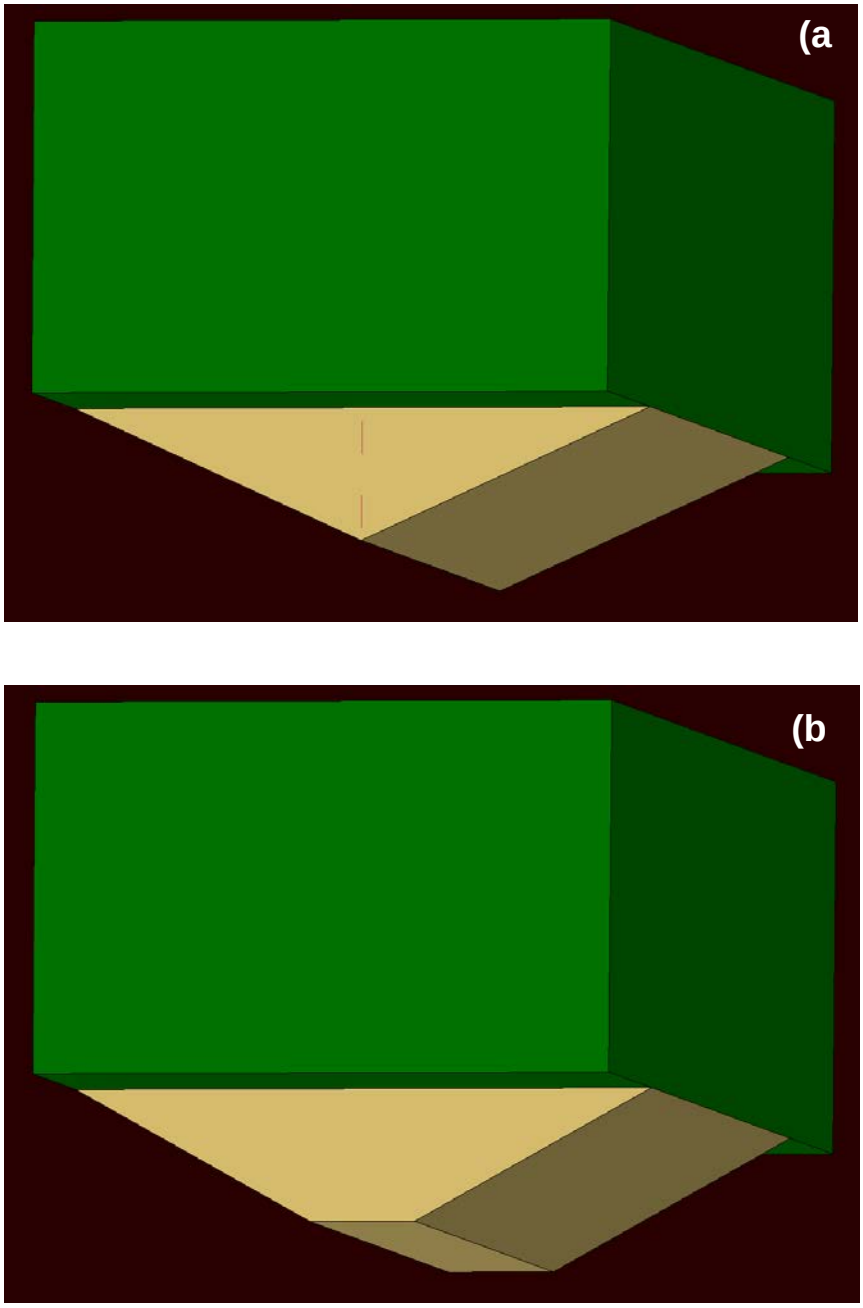

Figure 4–2 Two most common renditions of the V-shaped hull concept/solution: (a) standard V-shaped hull; and (b) truncated V-shaped hull.

The V-hull concept was further advanced in our recent work [1, 2] by attaching to it a series of side-vent-channels. The resulting so-called side-vent-channel solution was subsequently analyzed computationally in order to establish its blast-mitigation potential. As shown schematically in Figure 4-3, this solution utilizes flared tubular side-vent-channels (of the appropriate cross-sectional shape and wall thickness) open at both ends. (It should be noted that in order to prevent potential misuse of the ideas proposed and the results obtained in the present work, the term "***vehicle***" has been replaced in Figure 4-3 as well as in the remainder of the manuscript with the term "***surrogate box structure***," SBS.) The bottom end of each tube is cut parallel to the ground (to promote inflow of the detonation by-products and soil ejecta, and to prevent crushing/crumpling of the tube inlet under blast loads) and flush with the V-hull bottom. The channels/tubes are intended to function as exhaust nozzles as in the case of the pulse-detonation engine and, thus, provide a downward thrust to the SBS (through the gaseous-detonation products supersonic-expansion effects). The additional role of the side-vent-channels is to reduce the blast momentum transferred to the targeted SBS by improving the venting of the gaseous detonation products, soil ejecta and mine-casing fragments. To validate the side-vent-channel concept, detailed computational analyses involving detonation of a landmine (of a prototypical shape, size and DOB) buried underneath the vent-channel-equipped SBS, and the interaction of the air-blast, soil ejecta, and mine-casing fragments with the SBS have been conducted in Refs. [1, 2].

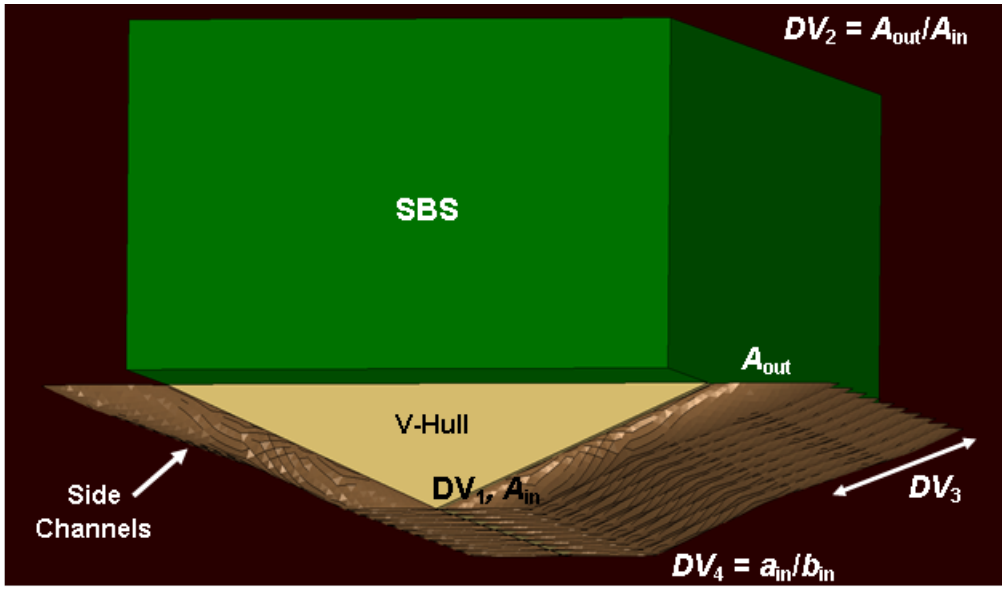

Figure 4–3 Side channels/tubes-based blast-mitigation concept originally proposed in Ref. [1]. Note that the abbreviation SBS stands for "*surrogate box structure*." The four design variables used in the SBS shape/size optimization analysis are defined; ain and bin are the semi-major and semi-minor axes of the channel inlet.

The computational analysis employed in Ref. [1] was of a combined Lagrangian/Eulerian fluid-structure interaction (FSI) type, within which both the gaseous materials (i.e. air and detonation products) and non-SBS solid materials (i.e. soil and mine fragments) are modeled as a multi-component Eulerian material. Consequently, this type of analysis suffered from at least the following two major deficiencies: (a) inaccuracies/uncertainties related to the definition of the boundaries between different components of the Eulerian material, and between the Eulerian and SBS-Lagrangian materials; and (b) inability to take into account the granular/discrete character of the soil ejecta. Despite these deficiencies, the computational analyses carried out in Ref. [1] established, at least in semi-quantitative terms, that the side-vent-channels: (i) lower the blast impulse transferred to the vehicle, by promoting venting of soil ejecta, gaseous detonation products and mine-casing fragments resulting from a mine-blast underneath the vehicle; (ii) lower the possibility for the vehicle lift-off from the ground, by promoting supersonic expansion of gaseous detonation products exiting the channel, and thereby helping to create a downward thrust on the vehicle; (iii) do not limit the mobility of the occupants within the vehicle and their ability to survey the surroundings, since the vent-channels do not pass through the SBS cabin; and (iv) do not compromise SBS off-road structural reliability and durability, since the side-vent-channels attached to the V-hull do not considerably increase SBS-frame rigidity and, thus, do not significantly increase the rate of vehicle-frame fatigue-induced failure.

The aforementioned deficiencies of the combined Eulerian/Lagrangian analysis employed in the computational investigation of the side-vent-channel concept in Ref. [1] were addressed in our subsequent paper [2]. In Ref. [2], the side-vent-channel concept/solution was re-examined using combined finite-element/discrete-particle computational methods and tools. Within this approach, all non-SBS materials are treated as assemblies of discrete particles. The combined

finite-element/discrete-particle analysis reconfirmed the aforementioned findings (yielded by the combined Eulerian/Lagrangian computational analysis) regarding the blast-mitigation utility and efficacy of the side-vent-channel solution. In addition, a parametric study for the geometry of the side-vent-channels was conducted in Ref. [2] in order to assess the sensitivity of the downward thrust on the vehicle (the performance function) to changes in the side-vent-channel geometrical parameters. Examples of the results yielded by the parametric study are depicted in Figures 4-4(a)–(b).

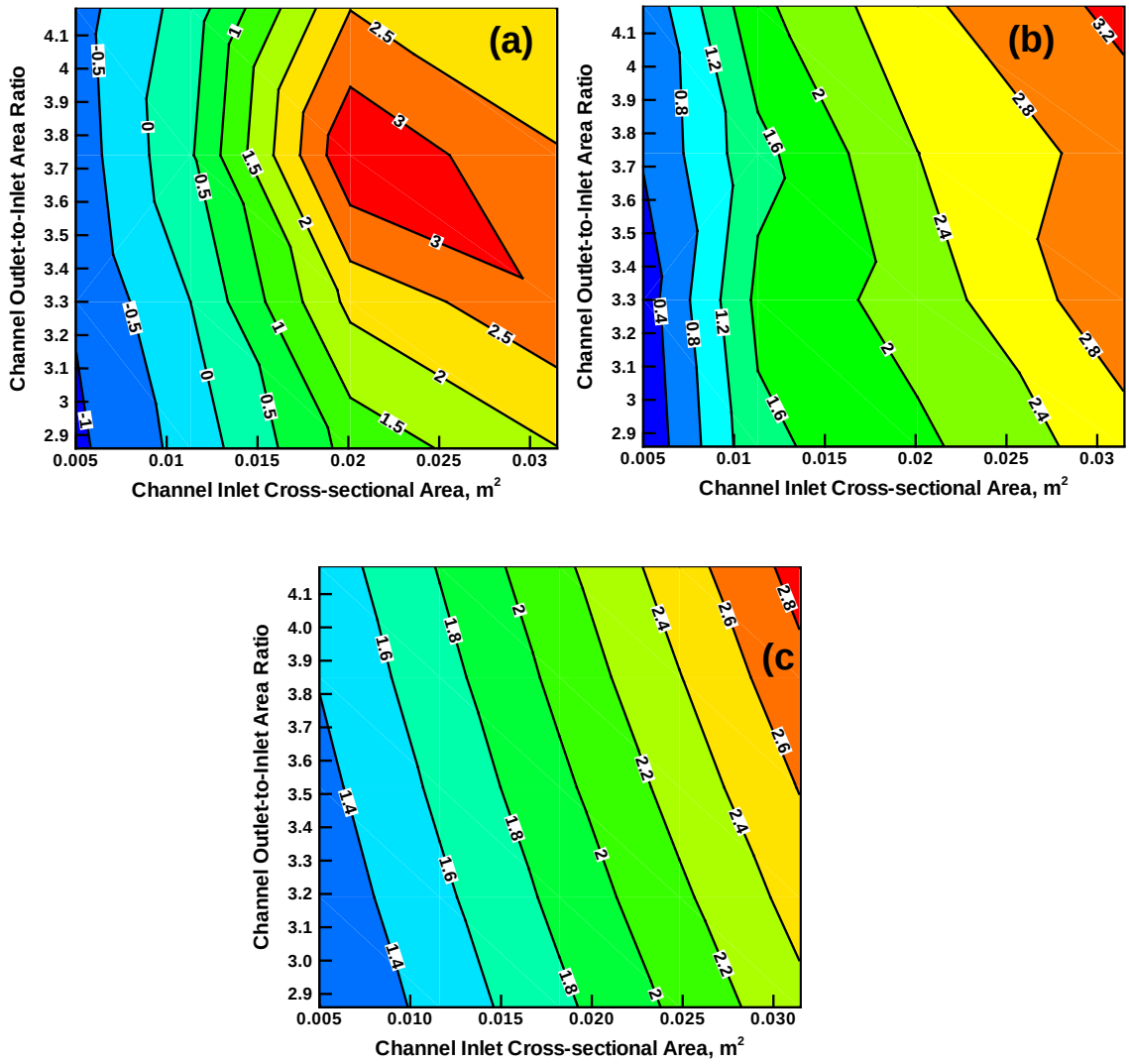

Figure 4–4 Percent reduction (relative to the SBS case without side-vent-channels) in: (a) total detonation-induced momentum transferred to the SBS; and (b) maximum SBS acceleration for the SBS configuration containing flared side-vent-channels, as a function of channel inlet-area and inlet-to-outlet area ratio [2]. The results are obtained using a combined finite-element/discrete-particle computational analysis. (c) The associated percent increase in the SBS mass in the same SBS design space.

In the side-vent-channel parametric study, circular-cross-section channel-inlet area and the channel outlet-to-inlet area ratio are used as design variables, while the percent reduction in: (a) the total momentum transferred to the SBS, Figure 4-4(a); and (b) the maximum acceleration acquired by the SBS, Figure 4-4(b) (relative to the SBS case without side channels) are treated as the performance functions (to be maximized).

The results displayed in Figure 4-4(a) reveal that: (a) there is a region in the channel inlet area/channel outlet-to-inlet area-ratio design space which is associated with positive reductions in the blast momentum transferred to the SBS; (b) however, the maximum transferred-momentum reduction (ca. 3.5%) is relatively small.

It should be noted that, due to the changing geometry and size of the side-vent-channels, the SBS mass is not constant throughout the design space but rather increases both with the channel inlet area and outlet-to-inlet area ratio. Variation of the SBS mass throughout the design space is depicted in Figure 4-4(c) using a contour plot. A comparison of the results displayed in Figure 4-4(a) with those displayed in Figure 4-4(c) reveals that in the portion of the design space in which the transmitted impulse takes on the lowest values, the SBS mass is ca. 2.2% larger than that of the SBS without side-vent-channels. This finding is important since an increase in the SBS mass (without any change in the SBS configuration) gives rise to an increase in the magnitude of the transferred momentum. This increase, for the estimated mass-range of the ejected soil interacting with the SBS, has been estimated to be ca. 0.4%. Hence, if the changes in the SBS configuration involving the introduction of side-vent-channels and their flaring can be accomplished without an increase in the SBS mass (e.g. through the use of armor materials with an increased blast efficiency), further reductions in the momentum transferred to the SBS can be expected.

The results displayed in Figure 4-4(b) reveal that: (a) the largest reduction in the maximum SBS acceleration is obtained in the portion of the design space in which both the channel inlet area and channel outlet-to-inlet area-ratio acquire the largest values. This finding is consistent with the fact that: (i) the SBS mass also acquires the largest values in this portion of the design space; and (ii) the SBS acquires a maximum acceleration during the earlier inertia-controlled stages of the blast/SBS interaction; (b) however, as in the case of the momentum transfer, the largest reductions in the SBS maximum acceleration are found to be quite small (ca. 3.3%).

It should be recognized that a mere increase in the SBS mass results in an acceleration reduction. Since SBS configuration modifications involving the introduction of side-vent-channels and their flaring are accompanied by mass increases, it is important to separate the contributions of the increased mass and the lowered transferred momentum to the observed reductions in the SBS acceleration. Towards that end, the results displayed in Figure 4-4(b) are combined with the results displayed in Figure 4-4(c), in order to first assess the portion of the percentage reduction in the maximum SBS acceleration which is the result of the associated mass increase. This procedure revealed that the SBS mass increase reduces the SBS maximum acceleration by a maximum amount of ca. 2.9%. This finding is fully consistent with the fact that the maximum SBS mass increase due to the introduction of flaring of the side-vent-channels is ca. 2.9%. The remainder in the maximum acceleration reduction (3.3% – 2.9%) can be attributed to the reduced momentum transferred to the SBS structure resulting from the introduction and flaring of the side-vent-channels.

It should be recognized that SBS maximum acceleration is a key blast-variable which must be monitored/controlled since it is believed to correlate with the extent of occupants' injury.

Consequently, further reductions in the SBS maximum acceleration are needed through the side-vent-channel concept refinement and solution optimization.

Main Objectives: The main objective of the present work is to carry out a geometrical design-optimization analysis of the side-vent-channels solution with respect to maximum combined reductions in the momentum transferred to, and the maximum acceleration acquired by, the SBS subjected to detonation of a mine buried underneath the SBS. Towards that end, the combined finite-element/discrete-particle computational method developed and used in [2] to analyze the blast-mitigation potential of the side-vent-channel concept will be combined with an optimization algorithm.

Paper Organization: A brief description of the problem analyzed in the present work and a brief overview of the computational methods and tools used to analyze the interaction of the air-blast-ejected soil and detonation products with the target SBS are provided in Section II. The optimization algorithm used in the side-vent-channel shape/size optimization analysis, as well as the definition of the design variables, constraining relations, and the objective functions, are presented in Section III. The main results obtained in the current work are presented and discussed in Section IV. The key conclusions yielded by the present work are summarized in Section V.

4.3 Problem Description and Computational Analysis

As mentioned earlier, the main objective of the present work is to carry out a geometrical optimization analysis of the side-vent-channel solution for the largest combined reductions in the transferred momentum and maximum acceleration (the objective function) of the SBS subjected to blast-loads resulting from the detonation of a mine buried underneath the SBS. To evaluate the objective function, the novel coupled finite-element/discrete-particle computational analysis reported in [2] is utilized. In this section, details are presented regarding the basic problem formulation and a brief description is provided of the computational procedure used for the objective function evaluation. In Section III, details will be presented regarding the optimization method used to determine optimum size and shape of the side-vent-channel solution.

4.3.1. Problem Description

The basic problem analyzed in the present work involves detonation of a shallow-buried mine underneath the targeted SBS (equipped with the V-shaped hull, with or without side-vent-channels), and the subsequent interaction of gaseous detonation products, soil ejecta and blast waves with the SBS underbody. Details regarding the recasting of this physical problem into the corresponding mathematical model and the computational techniques used to investigate this problem and to establish blast-mitigation potential of the side-vent-channel solution are presented in the following sub-sections.

4.3.2. Computational Domain

The computational domain used consists of two separate sub-domains, one of the continuum Lagrangian-type and the other of a discrete-particle (also Lagrangian) type. The initial configuration of the prototypical computational domain analyzed is depicted in Figure 4-5. The continuum sub-domain comprises the SBS equipped with the V-hull and, in most cases, side-vent-channels, and is modeled as a finite-element structure consisting of between 60,000 and 80,000 three-noded shell elements (depending on the SBS configuration). While both the cases of rigid SBS and deformable SBS were analyzed under the present effort, only the results pertaining to the rigid-SBS case will be presented and discussed in this manuscript.

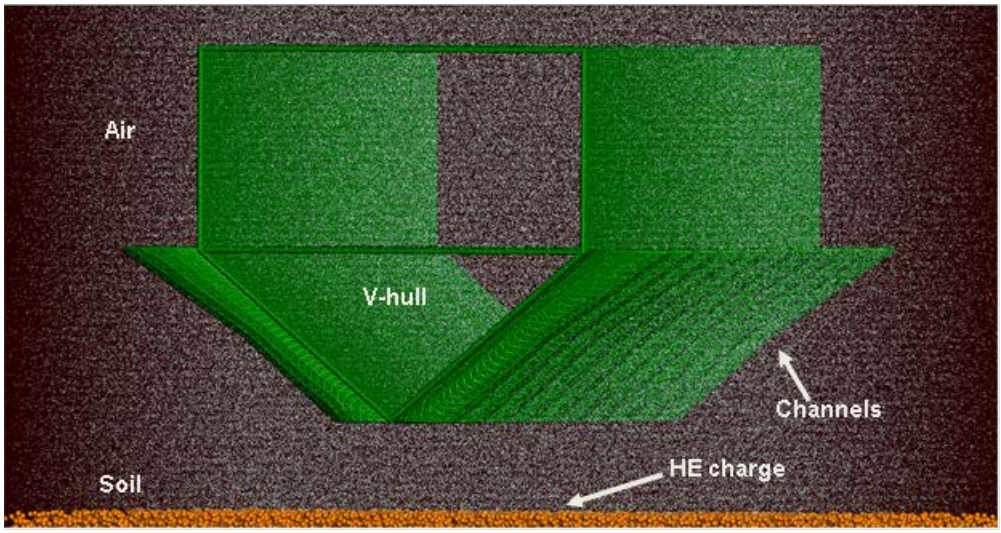

Figure 4–5 A prototypical computational domain used in the combined three-dimensional finite-element/discrete-particle analysis of the buried-mine detonation event and the subsequent interactions of the detonation products, soil ejecta and air blast with the SBS equipped with a V-hull and side vent channels. Please note that the mine is shallow-buried and its view is obstructed by the surrounding soil.

As far as the discrete-particle sub-domain is concerned, it comprises mine/detonation-products, sand/soil, and the ambient air. The discrete-particle sub-domain is confined within a rectangular parallelepiped-shaped region which also encloses the SBS. Details regarding the discrete-particle modeling and simulations will be presented in the next sub-section.

It should be noted that the SBS structure (as well as the discrete sub-domain) possesses two vertical planes of symmetry, suggesting that only one-quarter of the computational domain has to be analyzed explicitly. However, since following detonation, discrete particles acquire a non-symmetric distribution of their velocities; the entire computational domain was analyzed. By analyzing the entire computational domain, rather than one of its quarters, potential lateral components of the translation and rotation of the SBS are also enabled.

4.3.3. Discrete-Particle Formulation

Since this computational procedure was described in great detail in Ref. [2], only a brief overview of it will be provided in the remainder of this section. Within this formulation (also known as the "***corpuscular***" approach [24]), high explosive (HE) gaseous detonation products, soil and air are all represented as assemblies of discrete, rigid, spherical, interacting particles which exchange momentum and kinetic energy during their collisions/contact among themselves or with the SBS. To make the computational cost manageable, each particle is defined to represent a collection of 10^{15}–10^{20} molecules.

Being of a Lagrangian character, this discrete-particle formulation offers several advantages such as: (a) calculation of the material advection through the mesh (one of the main sources of numerical inaccuracy) is not required; and (b) there are no major challenges associated with locating contact interfaces between HE detonation products, soil and air and (complex-geometry) Lagrangian targeted-SBS.

In the remainder of this section, a brief overview is given of the discrete-particle models for the HE detonation products, air and soil. It should be noted that, as explained by Olovsson et al. [24], discrete-particle models for the HE detonation products and air are essentially an extension of the kinetic molecular theory of gases [25]. Specifically, as in the case of the kinetic molecular theory, collisions between HE and air particles are assumed to be of a purely elastic (i.e. kinetic-energy-preserving) character. However, in contrast to the kinetic molecular theory, the HE and air particles used are not single molecules but rather assemblies of molecules. In the case of soil particles, on the other hand, particle collisions are not of an elastic type but rather accompanied by energy dissipation due to operation of time-dependent viscous and frictional-sliding energy-dissipation processes.

Kinetic Molecular Theory of Gases

The kinetic molecular theory is a theory which successfully relates molecular-level events such as collisions to the macroscopic properties, e.g. pressure or temperature of an ideal gas. Within the theory, the system of interacting gas molecules is assumed to have the following four characteristics: (a) the size of the molecules is much smaller than the average inter-molecular distance. Consequently, the volume of the molecules is negligible in comparison to the volume of the space within which the gas resides; (b) the system is in the state of thermodynamic equilibrium, i.e. there is no net flux of mass, linear momentum or energy through the system; (c) particle dynamics is governed by Newton's laws of motion; and (d) inter-molecular and molecule/structure interactions are perfectly elastic and, thus, not only the linear momentum but also the total kinetic energy is preserved.

Through a detailed statistical analysis of molecular-level interactions carried out within the kinetic molecular theory, the basic functional relationships are defined for: (a) equilibrium molecular velocity Maxwell-Boltzmann distribution function; (b) root-mean-square (rms) molecular velocity, which scales with the square root of the temperature; (c) mean-free-path of the molecules (i.e. the mean distance traveled by a molecule between collisions); (d) frequency of collisions; and (e) pressure (defined as an average rate of change of the momentum, during collisions, per unit area of the surroundings). These functional relations, which can be found in Ref. [2], serve as a basis for the corresponding (appropriately modified) functional relationships for HE and air.

High-Explosive Gaseous Detonation Products

The constitutive and the dynamic response of HE gaseous detonation products is represented using the discrete-particle material model proposed by Olovsson et al. [24]. Since a detailed overview of this model could be found in Ref. [24], only a brief account of it is given

below. Complete parameterization of the HE discrete-particle model requires specification of the following four quantities: (i) initial mass density, $\rho_{0,HE}$. Once the number of molecules per particle is selected, $\rho_{0,HE}$ controls the number of particles per unit volume; (ii) initial volumetric internal energy density, $E_{0,HE}/V$, a quantity which defines the sum of the initial translational and rotational kinetic energies of the HE discrete-particle system; (iii) constant-pressure to constant-volume heat-capacity ratio $\gamma_{HE} = C_{p,HE} / C_{v,HE}$. This quantity controls initial partitioning of the specific kinetic energy into its translational and rotational/vibrational components; and (iv) fraction of the total volume occupied by the discrete particles, b_{HE} (the so-called "***co-volume effect***"). This term is used to correct the pressure relationship, as defined by the kinetic molecular theory in the high-pressure regime (the regime in which the ideal-gas assumption regarding the negligible volume of the particles is no longer valid).

The four aforementioned HE discrete-particle model parameters were determined by Børvik et al. [26], within an optimization procedure, by matching the model predictions to the experimental results of Souers et al. [27], for the so-called "***cylinder test***". Within this test, an oxygen free high conductivity (OFHC) copper pipe is filled with an HE and the explosive is detonated at one end. This causes the formation of a (transverse) detonation wave and its propagation along the length of the pipe. During parameterization of the C-4 discrete-particle material model, Børvik et al. [26] carried out combined finite-element/discrete-particle simulations within which the OFHC pipe is treated as a continuum-Lagrangian finite-element discretized component (modeled using the Johnson-Cook linear-elastic/strain-hardening/rate-dependent/thermally-softenable-plastic constitutive equation [28]) while C-4 is represented as an ensemble of 1,000,000 discrete particles. Next, within an optimization study, the discrete-particle model parameters are varied systematically until good agreement is obtained between the

computed temporal evolutions and spatial distributions of the pipe radial displacement/velocity (caused by the explosive detonation initiated at one end of the pipe) and the corresponding experimental results. The procedure employed by Børvik et al. [26] yielded the following C-4 HE discrete-particle material-model parameters: (i) $\rho_{0,HE}$ = 1601 kg/m3; (ii) $E_{0,HE}$ / V = 8.7 GJ/m^3; (iii) γ_{HE} = 7/5 ; and (iv) b_{HE} = 0.35.

Air

Air surrounding the target structure and located above the soil is treated as a diatomic ideal gas initially at the ambient pressure (101.3 kPa) and reference temperature (298 K). Following Børvik et al. [26], the four basic discrete-particle model parameters are assigned the following values: (a) $\rho_{0,air}$ = 1.184 kg/m^3; (b) $E_{0,air}$ / V = 0.25325 MJ/m^3; (c) γ_{air} = 7/5; and (d) b_{air} = 0 (no co-volume effects considered). Since the collision of two air particles (as well as between two C-4 HE particles, or between air/HE particles and the rigid SBS) is of an elastic character, the momentum and the total kinetic/internal energy are conserved. These conservation conditions are used to determine particle and SBS velocities following collision. As far as the collision between an air or HE particle and a movable/deformable SBS is concerned, it is associated with an exchange of kinetic translational energy between the particle and the SBS. Also, it should be noted that particle/particle and particle/SBS interactions are associated with momentum transfer, which causes a change in the translational/rotational kinetic-energy-components ratio, i.e. the system analyzed is not in thermal equilibrium.

Soil

The soil discrete-particle model differs from those used for the HE gaseous detonation products and air in that soil particle collisions are modeled using a penalty algorithm rather than an (kinematic) elastic collision algorithm used in conjunction with HE and air particles. This was

done in order to account for the effects such as: (i) soil-particle finite stiffness; (ii) rate-dependent dissipative/damping nature of the inter-particle collisions; and (iii) the inter-particle frictional effects.

The essential features of the penalty contact method used are depicted schematically in Figure 4-6 which shows a two-particle contact model. Within this model, particle normal interactions are accounted for by a linear spring (with a spring constant k) and a linear dashpot (with a damping coefficient c) connected in parallel. As far as the tangential interactions are concerned, they are modeled using a linear spring (also of stiffness k) and a Coulomb frictional element (which is characterized by a friction coefficient μ and which limits the tangential-spring force). It should be noted that, in the present formulation, the soil-particle stiffness is not accounted for explicitly since the particles are of a rigid type. Rather, through the proper selection of the stiffness constants of the normal and tangential contact springs, particle stiffness is accounted for implicitly. Also, soil-particle fracture processes are not considered (explicitly or implicitly) since they are associated with minor energy absorption/dissipation effects and, as shown in our prior work [29], do not significantly affect the computational results.

According to Figure 4-6, the discrete-particle model of soil is characterized by three parameters: k, c and μ. To this list should be added the mean particle-mass m (particles are considered to be rigid and spherical, with a relatively narrow size distribution [2]). For the selected particle-size mean and standard deviation, m is determined from the knowledge of the soil particle-material density (= 2700 kg/m^3) and initial particle volume-fraction/packing-density (=0.6). The values of k, c and μ are determined using an optimization procedure within which the model predictions pertaining to the unconstrained and laterally constrained compression of a soil sample are matched with their experimental counterparts [2, 30]. This procedure yielded the

following soil-saturation-dependent values of the soil discrete-particle model parameters: (a) dry soil: k = 4 GN/m, c = 0.0 MN.s/m, and μ = 0.15; and (b) saturated soil: k = 40 GN/m, $\xi = c/2\sqrt{mk}$ = 0.025 and μ = 0.01.

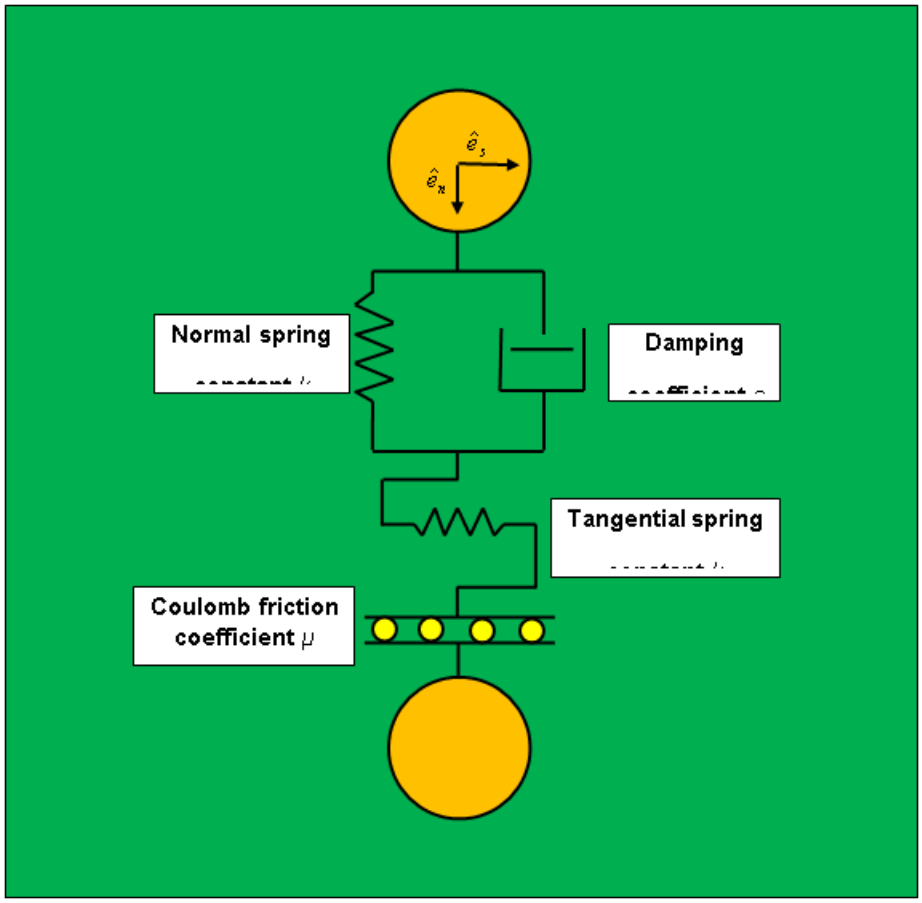

Figure 4–6 A schematic of the contact-mechanics model involving two interacting equal-sized/mass spherical particles of soil.

4.3.4. Computational Analysis-Type

The mine-detonation event and the subsequent interactions between the detonation products, soil ejecta and air blasts with the SBS are analyzed computationally using a finite-element/discrete-particle algorithm. As mentioned earlier, both the discrete-particle and the continuum portions of the computational domain are of a Lagrangian character (i.e. the particle geometry and the finite-element mesh are each attached to the underlying material). In the analysis in which the SBS was modeled as a deformable structure, energy dissipation associated with plastic deformation and damage/failure of the SBS is treated as a heat-source. Due to the extremely short duration of the mine-blast detonation event (ca. tens of milliseconds), heat conduction analysis is not carried out. Rather, the purely mechanical analysis is conducted under adiabatic conditions. The effects of local changes in temperature due to adiabatic heating are accounted for through the use of temperature-dependent material properties.

4.3.5. Initial Conditions

Prior to the beginning of the computational analysis, the continuum-Lagrange sub-domain is occupied by the SBS, while the respective parts of the discrete-particle sub-domain are filled with HE detonation products, soil and the ambient air. The continuum-Lagrangian SBS sub-domain is assumed to be initially stress-free and stationary.

Filling of the discrete-particle sub-domains with air, soil and detonation products was done in the following way: ***Air***: for the selected number of air molecules per discrete particle, $N_{mpp,air}$, and the known values of $\rho_{0,air}$ and V_{air}, the number of air discrete particles, $N_{p,air}$, is computed. These particles are placed randomly within the air-portion of the discrete-particle sub-domain. Next, random initial velocities are assigned to the air particles by sampling the Maxwell-Boltzmann distribution function, with the molecular weight of air set to 29 g/mol and the temperature set to 298 K, while ensuring that the root-mean-square velocity of the air discrete-particle model is identical to that found in the ideal gas, ca. 506 m/s, as modeled by the kinetic molecular theory. This condition ensures that the discrete-particle air pressure (=101.3 kPa) is consistent with E_0 / V = 0.25325 MJ/m3 and γ_{air} = 7/5, in accordance with the ideal gas law; ***Soil***: As far as the soil sub-domain is concerned, it is constructed by partitioning it into a three-dimensional array of unit cells and filling each unit cell identically while ensuring that no "***penetration***" (other than the one caused by gravity) exists between the neighboring particles; and ***HE detonation products***: In the case of HE, initially stationary particles of undetonated explosive charge are placed randomly within the HE portion of the discrete-particle sub-domain following a procedure identical to that used in the case of air particles. Next, the explosive charge is detonated. Within the discrete-particle framework, HE detonation is simulated in the following way. At t=0 (the detonation time), with the exception of the HE located at the detonation point(s),

the explosive is assumed to be in the solid state and, as mentioned above, the HE discrete particles are assumed to be at rest (more precisely, to have a zero average translational velocity). As the detonation front expands, increasingly more HE is detonated, i.e. converted into the gaseous state due to arrival of the detonation front. Once this solid-gas conversion takes place in a region, the HE particles are assigned a velocity by randomly sampling the Maxwell-Boltzmann thermal velocity distribution function, [25], consistent with the $\rho_{C\text{-}4}$ = 1.82 g/cm^3, $M_{C\text{-}4}$ = 222 g/mol and $T_{C\text{-}4}$ = ca. 3500 K, where detonated C-4 is treated as mono-atomically decomposed RDX, $C_3H_6N_6O_6$. The sampled velocities are next corrected by dividing them with $(1 - b_{C\text{-}4})^{1/2}$ in order to account for the aforementioned co-volume-induced pressure increase.

4.3.6. Boundary Conditions

Over the portions of the computational-domain external surfaces initially associated with air and soil, an external/ambient pressure of 101.3 kPa is applied so that particles arriving at the boundary and associated with a local pressure exceeding the external pressure are allowed to leave the computational domain. On the other hand, particles which arrive at the external boundary and are associated with a sub-ambient local pressure are reflected back into the domain.

4.3.7. Contact Algorithm(s)

As mentioned earlier, soil/soil particle interactions are modeled using a (viscoelastic/frictional normal/tangential) penalty contact algorithm. On the other hand, HE/HE, air/air, HE/air, soil/HE and soil/air particle interactions are modeled using an (kinematic) elastic contact algorithm.

As far as discrete-particle/SBS interactions are concerned, they are modeled using a penalty-contact algorithm. Within this algorithm, contact kinematic constraints are enforced by ensuring that the extent of contact pressure is governed by the local surface penetrations (where the default penalty stiffness parameter is automatically maximized subject to stability limits). As far as the shear stresses are concerned, they are transferred via a "***slip/stick***" algorithm, that is, shear stresses lower than the frictional shear stress are transferred without interface sliding (otherwise interface sliding takes place). The frictional shear stress is defined by a modified Coulomb law within which there is an upper limit to this quantity (set equal to the shear strength of the continuum-Lagrange SBS sub-domain material). The frictional shear stress is then defined as the smaller of the product between the static/kinetic friction coefficient and the contact pressure, on the one hand, and the continuum-Lagrangian sub-domain SBS-material shear strength, on the other.

4.3.8. Material Model(s)

The constitutive models for the three discrete-particle materials (i.e. HE detonation products, soil and air) have been presented in Section II.3. It should be recalled that while discrete-particle representation of these three materials is based on rigid particles, the materials' deformability has been recovered through the use of the appropriate contact algorithms. As far as the continuum-Lagrangian SBS sub-domain is concerned, it was modeled either as a rigid structure or a deformable structure. In the cases when the SBS was modeled as a rigid structure, the material's constitutive model is fully-defined by the mass density (=7850 kg/m^3, for steel). When the SBS was modeled as a deformable structure, it was assumed to be made of conventional AISI 4340 steel whose deformation and failure constitutive response could be represented using the Johnson-Cook material model [31]. A detailed overview of this material model including its AISI 4340 parameterization can be found in our recent work [31, 32].

4.3.9. Computational Algorithm

The governing mass, linear momentum and energy conservation equations are solved with a second-order accurate explicit combined finite-element/discrete-particle algorithm. All the calculations in the present work are carried out by combining a general-purpose mathematical program MATLAB [27] with a customized version of YADE (Yet Another Discrete Element), an extensible, open-source discrete-element method (DEM) computer program [28]. MATLAB was used to create the geometrical/meshed models and Python scripts which control YADE-simulation structure and execution, as well as input/output communications.

4.3.10. Computational Accuracy, Stability and Cost

A standard particle-size and mesh-refinement sensitivity analysis was carried out (the results not shown for brevity) in order to ensure that a convergence of the key results is reached with respect to the further variations of these geometrical/mesh parameters. Due to the conditionally-stable nature of the explicit finite element analysis used, the maximum time increment during each computational step had to be kept lower than the attendant stable time increment. A typical 50 ms computational analysis followed by a detailed post-processing data reduction procedure required on average 24 hours of (wall-clock) time on a 12-core, 3.0 GHz machine with 16 GB of memory.

4.4. Shape/Size Optimization of Side-Vent-Channel

In this section, first a brief description is given of the procedure (known as the genetic algorithm) used to optimize the side-vent-channel geometrical parameters. Then a list of the side-vent-channel geometrical parameters (and their constraints) used in the optimization procedure (i.e. the design variables) and the goal of optimization (i.e. the objective function) are presented.

4.4.1. Genetic Algorithm

A review of the literature carried out as part of the present work identifies three main types of search methods: (a) calculus-based; (b) enumerative, and (c) random methods. While generally very fast, calculus-based methods suffer from two main drawbacks: (i) they are local in scope, i.e. they typically locate the maximum in the neighborhood of the current search point; and (ii) they entail the knowledge of derivatives of the objective function whose evaluation (even through the use of numerical approximations) in multimodal and potentially discontinuous search/design spaces represents a major limitation. In addition, the objective function is often evaluated using numerical procedures and, hence, the use of a calculus-based method does not generally offer any significant advantage. Within enumerative search methods, values of the objective function are evaluated at numerous preselected points in the search space. Consequently, this class of methods may become prohibitively expensive computationally for problems of even moderate size and complexity.

Within the random methods, one or more points in the design space are initially selected (at random) and the objective function evaluated at each point. Examination of the objective-function values is then used to guide subsequent selection of the points within the search space. Since many of the random optimization methods also suffer from the problem of locating the local maximum (rather than the global maximum within the design space), and are not suitable for multimodal (i.e. multiple maxima) and potentially discontinuous and/or mixed real/integer-type design spaces, the so-called genetic algorithm [33] (a method which does not suffer from these limitations) is used in the present work. In brief, the genetic algorithm creates a parameter string (a chromosome set), through (binary) coding, for each considered point (individual) in the search space and utilizes the Darwinian principle of "***Survival of the Fittest***" to ensure that

chromosomes of the fittest individuals are retained (with a higher probability) in subsequent generations.

At the beginning of the Genetic Algorithm search procedure, a random selection of the parameters is used to create an initial population of individuals (parameter sets) of size n in the search space. The fitness (i.e. the objective function) is next computed for each of the individuals based on how well each individual performs (in its environment). To generate the next generation of individuals of the same population size, the Genetic Algorithm performs the following three operations: (1) selection; (2) crossover, and (3) mutation. Within the selection process, fitter individuals are selected (as parents) for mating, while weak individuals die off. Through mating, the parents create a child with a chromosome set that is some mix of the parents' chromosomes. The mixing of parents' chromosomes during child creation is referred to as crossover. To promote evolution, a small probability is used to enable one or more child's chromosomes to mutate (change). The process of child creation and mutation are continued until an entirely new population (of children) of size n is generated. The fitness of each child is determined and the processes of selection, crossover and mutation repeated resulting in increasingly fitter generations of individuals. A logic flow chart of the genetic algorithm is shown in Figure 4-7. A few important details regarding parameter coding, selection, crossover and mutation are given below.

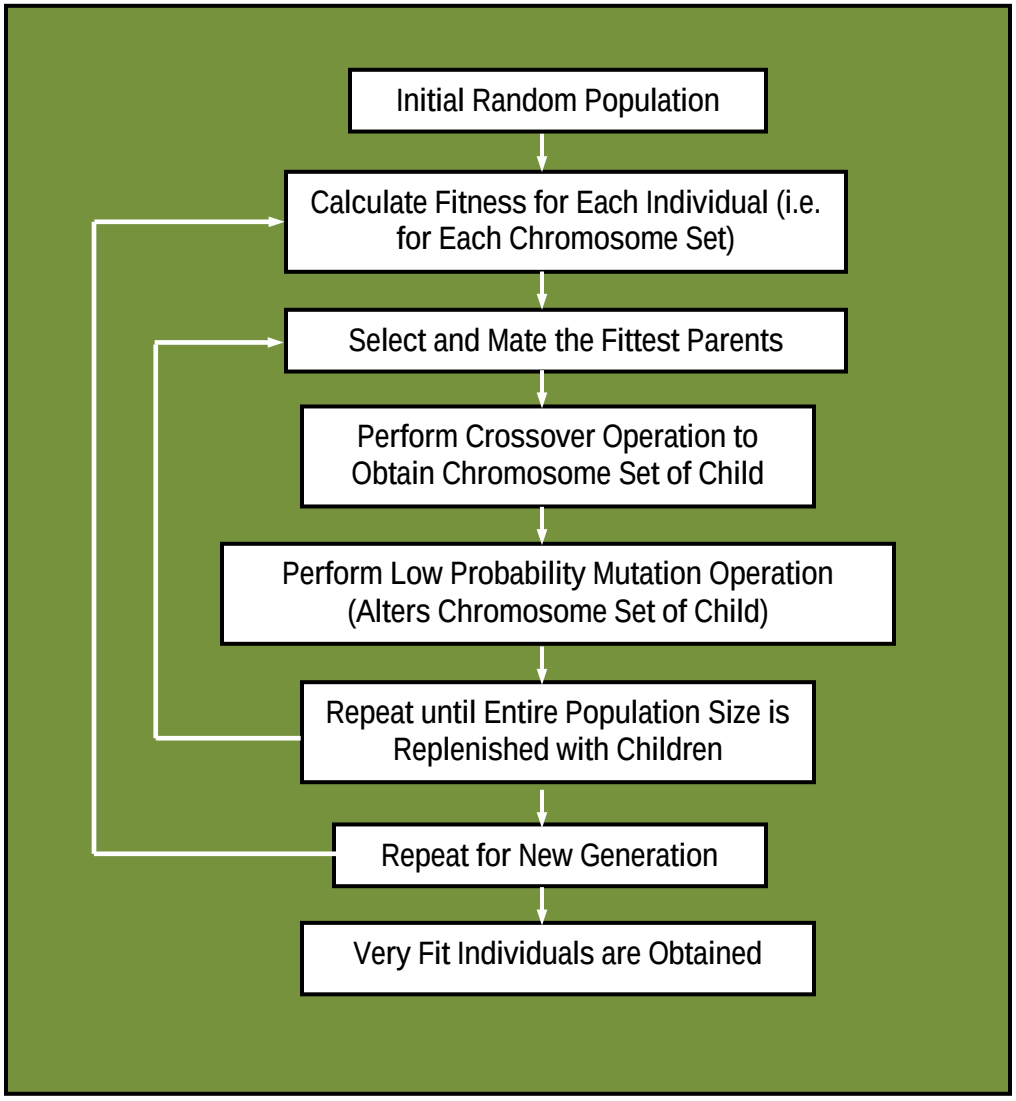

Figure 4–7 A flow chart for the genetic-algorithm optimization method.

Binary Parameter Coding: The total number of possible equally-spaced values of each parameter (within the selected range) is first defined. The number of possible values is typically set to 2^{nm}, where *nm* is a positive integer. Each possible value of a parameter is next coded using a binary format. For example, when the total number of possible values of a parameter is 2^{15} = 32,768, that parameter is coded using a string of fifteen 0's and 1's. Binary representations of all the parameters of an individual (a point in the search space) are then attached to form a long string (chromosome set).

Tournament Selection: Random pairs are selected from the population and the stronger individuals of each pair are allowed to mate and create a child. This process is continued until a new generation of size *n* is repopulated.

Single-Point Crossover: Within this process the chromosome set of the first (fitter) parent (e.g. 10101010) is mapped into that of the child. Then a crossover point is randomly chosen to the right of which the chromosome set of the second parent (e.g. *11001100*) overwrites the chromosome of the first parent. For example, if the crossover point is exactly in the middle of the chromosome, the child's chromosome set for the case at hand is 1010*1100*. The probability for the occurrence of crossover P_{cross} is typically set to 0.6. This implies that the probability that the child would retain the entire chromosome set of the first parent is $1.0 - P_{cross} = 0.4$.

Uniform Crossover: In this case, the crossover can take place at any (and all) points of the parents' chromosome sets and the child can end up with any combination of its parents' chromosomes. The probability for uniform crossover is also typically set to 0.6. It should be noted that, in this case, it is quite unlikely that the child would inherit the entire chromosome set of either of its parents.

Jump Mutation: In this process, one or more child's chromosomes can mutate. If the mutation takes place, the child will end up with a chromosome not present in either parent. Consequently, the jump mutation can cause one or more parameters to jump from one side of the range to the other. The probability of jump mutation is generally set equal to the inverse of the population size, $P_{mut}=1.0/n$.

Creep Mutation: In this type of mutation, the value of one or more (design) parameters of the child is changed by a single increment but must remain within the prescribed range. The probability for creep mutation is also typically set equal to the inverse of the population size.

Elitism: This operator is used to prevent a random loss of good chromosome strings during evolution. This is accomplished by ensuring that the chromosome set of the best individual generated to date is reproduced. If after the entire population of a new generation is generated through the processes of selection, crossover and mutation, the best individual is not replicated, then the chromosome set of the best individual is mapped into a randomly selected child in the new generation.

4.4.2. Design Variables, Constraints and the Objective Function

All the SBS configurations analyzed in the present work were associated with the following geometrical dimensions: (a) box-shaped extended cabin – L x W x H = 4.85 m x 2.2 m x 1.4 m; and (b) triangular-prism-shaped V-hull – L x W x H = 3.0 m x 2.2 m 0.5 m. Since the width of the cabin and the height of the V-hull are fixed, and side-vent-channels are cut flush with the V-hull bottom and top, the total length of the side-vent-channels is also fixed at $\sqrt{(1.1)^2 + (0.5)^2} = 1.21\,\text{m}$. Furthermore, the side-vent-channels are allowed to possess an elliptical cross-section, with a non-constant area (due to flaring). Thus, for a single side-vent-channel, there are four geometrical parameters (design variables): (a) the side-vent-channel inlet area, DV_1; (b) the outlet-to-inlet area ratio, DV_2; (c) the fraction of the channel length along which flaring is carried out, DV_3; and (d) the major-to-minor-axes ratio at the side-vent-channel inlet, DV_4. It should be noted that for the case of side-vent-channels with a circular cross-section, DV_4 takes on a value of $1/\cos(\alpha)$, where α (=67.75°) is the V-hull-apex half-angle. Furthermore, it should be noted that the terms "***major axis***" and "***minor axis***" are used to denote the elliptical cross-section axes which are respectively orthogonal and parallel to the V-hull. Consequently, the major axis will be allowed to take values smaller than those of the minor axis. For clarity, the four design variables are depicted in Figure 4-3.

The design variables are subjected to the following nonlinear constraints: (a) the values of the vent-channel inlet area and major-to-minor-axes ratio are constrained by the condition that the maximum channel minor axis must not exceed a maximum value beyond which channel overlap begins to take place; and (b) the side-vent-channel inlet area, the outlet-to-inlet area ratio, and the inlet major-to-minor-axes ratio are constrained by the fact that the increase in the SBS

width (due to introduction of the side-vent-channels and their flaring) does not exceed a maximal allowable value.

As far as the objective function is concerned, it is defined as a weighted average of the percent reductions in the detonation-induced momentum transferred to, and the maximum acceleration acquired by, the SBS. The two weighting factors used in the definition of the objective function are not independent, but rather sum to 1.0. Thus, only one weighting factor, the weighting factor for transferred momentum, had to be defined and its value varied between 1.0 (the optimization case in which only the minimization of the momentum transferred is considered) and 0.0 (the case in which the optimization is carried out only with respect to minimization of the maximum acceleration acquired by the SBS).

4.5. Results and Discussion

In this section, the key results obtained in this work are presented and discussed. First, some prototypical results yielded by the employed three-dimensional combined finite-element/discrete-particle computational model and analysis are presented and discussed. When discussing these results, particular attention is paid to providing insight into the ability of the side-vent-channels to lower the blast momentum transferred to, and the maximum associated acceleration acquired by, the SBS through the operation of venting and downward-thrust effects. In the second portion of this section, the results of the genetic-algorithm-based optimization analysis are reviewed and critically assessed.

4.5.1. Prototypical Results

The computational analyses employed yielded the results pertaining to the temporal evolution and spatial distribution of various particle-state and continuum-field quantities such as particles' position, (translational and rotational) particle velocities, particle/particle and particle/continuum-structure interaction forces and moments, etc. In addition, results pertaining to the explosive-charge detonation-induced loading experienced by, and the subsequent response of, the SBS structure were obtained. In the remainder of this section, a few prototypical results are presented and discussed.

Material Distribution and Temporal Evolution for a Typical SBS

Spatial distribution of three constituent materials (steel, HE detonation products and soil) at four (2 ms, 4 ms, 6 ms and 8 ms) post-detonation times in the case of a prototypical SBS equipped with flared side-vent-channels is shown in Figures 4-8(a)–(d). In these and subsequent figures, for improved clarity, air is removed while the detonation-products and soil-particles are displayed as spheres with the soil-particles having a smaller radius. Furthermore, for the same reason, initial positions of the soil and landmine particles are regularized while the SBS structure is shown as a wireframe. Examination of the results displayed in Figures 4-8(a)–(d), as well as their comparison with the corresponding results (not shown for brevity) for the SBS configuration with the V-hull but no side-vent-channels, established that the presence of side-vent-channels helps guide the flow of the gaseous detonation products and soil-ejecta (as well as air) along the direction parallel with the side of the V-hull. Closer examination of the distribution of the soil and the detonation products within the side-vent-channels reveals that the channels closest to the mine play the dominant role in the blast-venting process. Furthermore, it is seen that the ejected soil

initially retains its cohesion and relatively high density, Figure 4-8(a), while at later post-detonation times, ejected soil breaks up into non-bonded particles and acquires a low density, Figures 4-8(c)–(d).

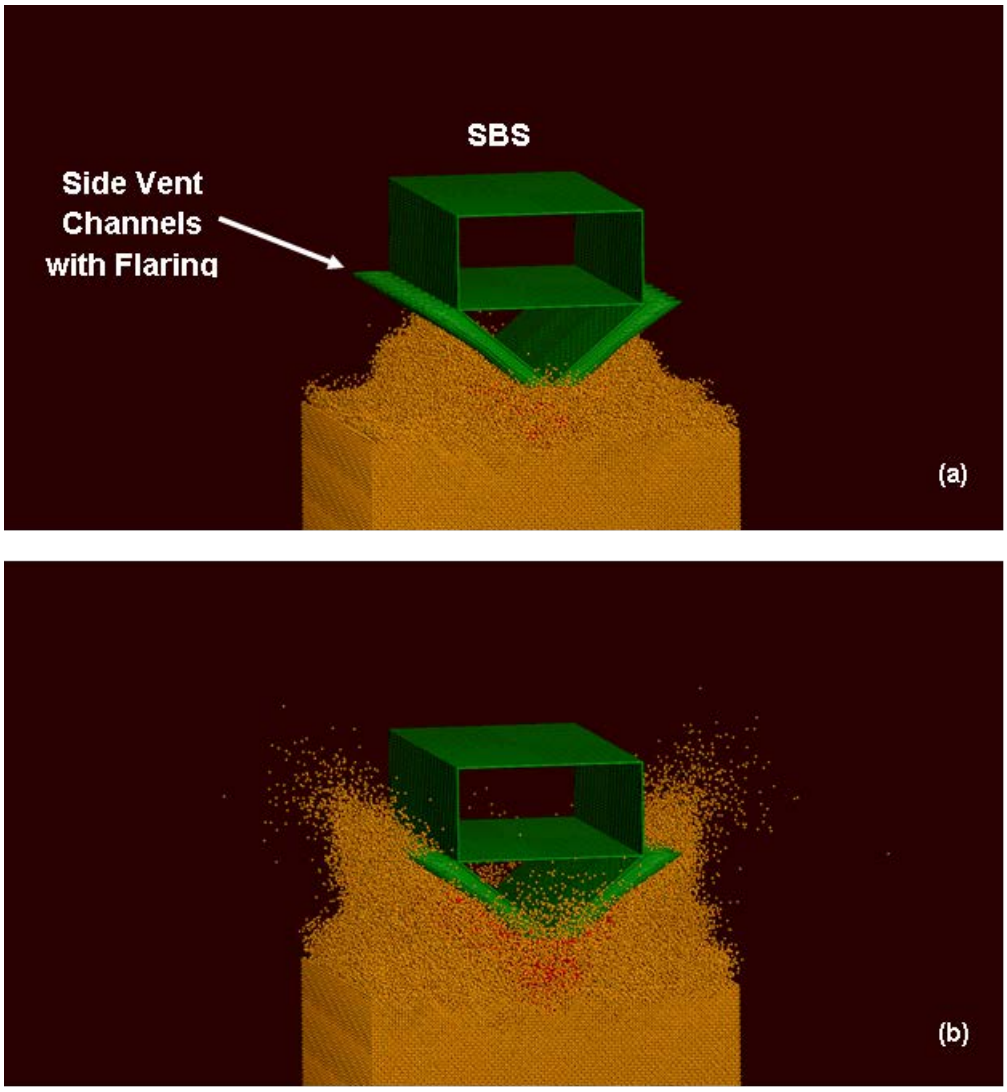

Figure 4–8 Spatial distribution of soil, HE detonation products and steel (the SBS material) in the case of the rigid SBS configuration equipped with flared side-vent-channels at post-detonation times of: (a) 2 ms; (b) 4 ms; (c) 6 ms; and (d) 8 ms.

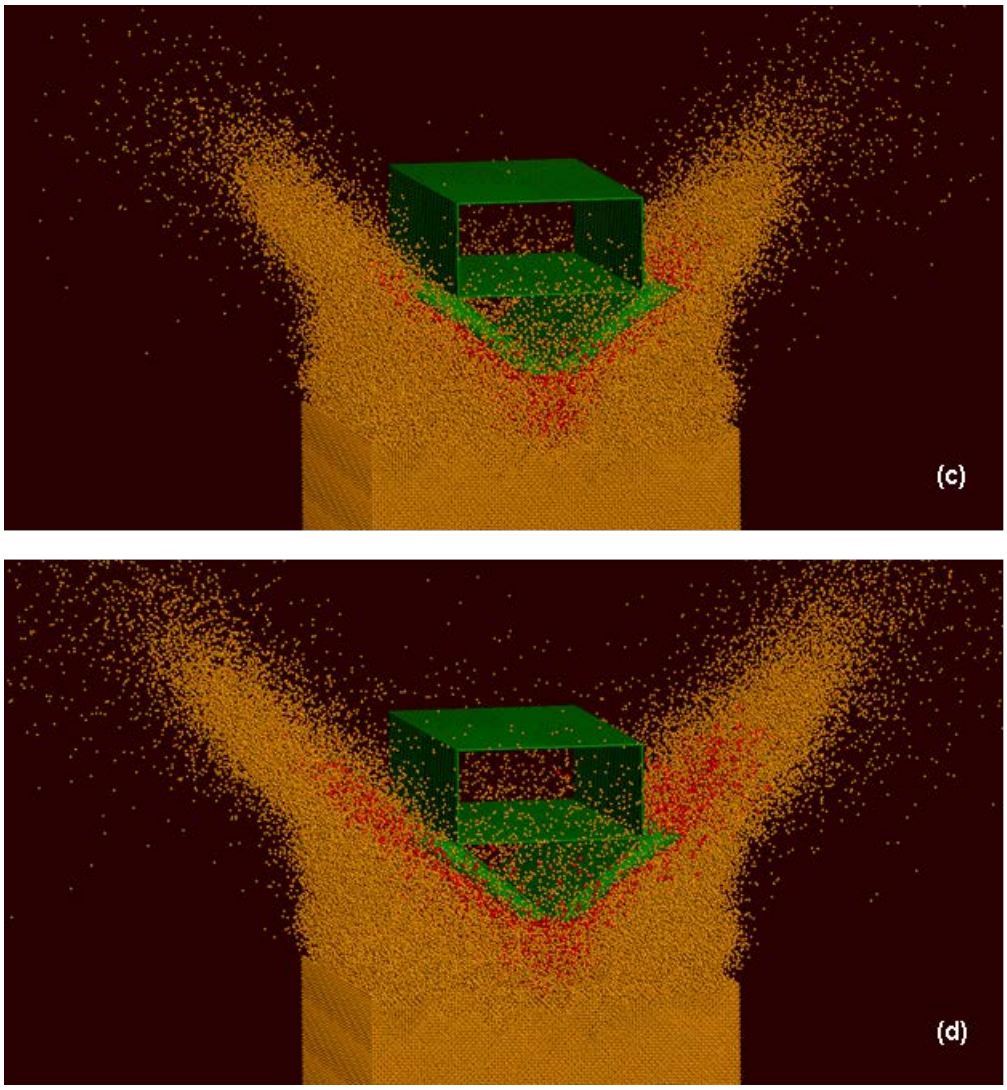

Figure 4-8. Continued.

Particle-Velocity Spatial Distribution and Temporal Evolution for a Typical SBS

Spatial distribution of the particle and SBS velocities at four (2 ms, 4 ms, 6 ms and 8 ms) post-detonation times for the same SBS configuration as the one referred to in conjunction with Figures 8(a)–(d), is shown in Figures 4-9(a)–(d). Examination of the results displayed in Figures 4-9(a)–(d) clearly reveals: (a) formation of a "hump" on the top surface of the soil above the detonated mine, Figure 4-9(a); (b) the onset of formation of a crater within the soil, Figures 4-9(c)–(d); and (c) non-uniform distribution of the particle velocities over the constant-z section of the channels. The velocity non-uniformity is characterized by smaller particle velocities (indicated by the blue or adjacent spectrum colors) in the portions of the channels closer to the V-hull and higher particle velocities (indicated by the red or adjacent spectrum colors) in the portions of the channels farther away from the V-hull. This finding can be rationalized as follows. Interaction of the ejected particles with the portions of the channel walls which are adjacent to the V-hull gives rise to a transfer of upward momentum to the SBS and an associated reduction in the particle (upward) velocities. On the other hand, interaction of the ejected particles with the portions of the channel walls which are away from the V-hull gives rise to a transfer of a downward momentum to the SBS and the associated increase in the particle (upward) velocities.

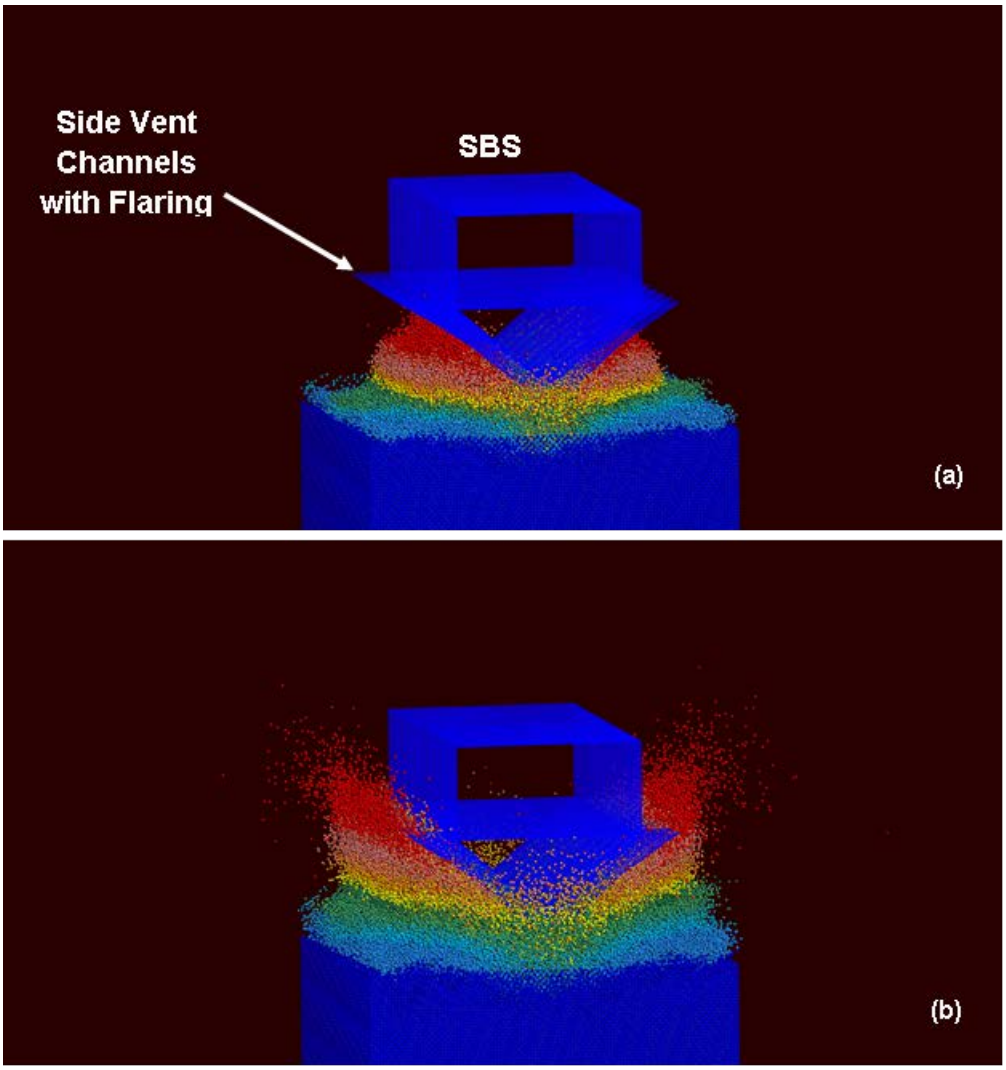

Figure 4–9 Spatial distribution of the velocities of the soil and mine-detonation-product particles and rigidized-SBS for the same SBS configuration as that referred to in Figures 8(a)–(d) at post-detonation times of: (a) 2 ms; (b) 4 ms; (c) 6 ms; and (d) 8 ms.

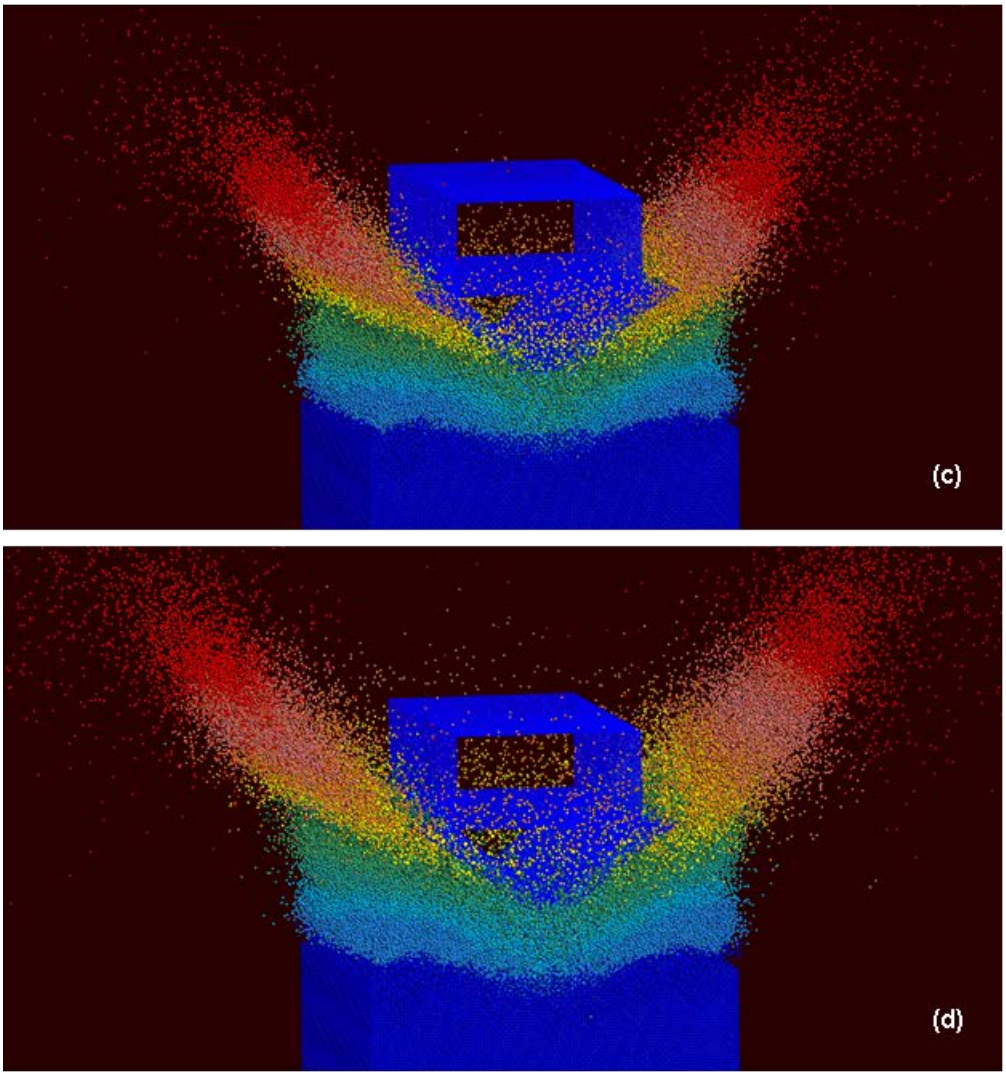

Figure 4-9. Continued.

SBS Velocity and Acceleration Temporal Evolution

The results presented in the previous section suggested that the presence of flared side-vent channels may have a positive role in reducing the effect of buried-landmine detonation on the SBS. In this section, more quantitative results pertaining to this blast-mitigation effect of the side-vent channels are presented and discussed.

Examples of the typical SBS velocity vs. time and SBS acceleration vs. time results obtained in the present work are shown in Figures 4-10(a)–(b), respectively. In both cases, the quantity plotted along the y-axis is normalized by its maximum value while the time is normalized by its value corresponding to the SBS maximum velocity. Examination of the results displayed in these figures shows that the SBS velocity initially experiences a sharp rise, reaches a peak value and then gradually decreases under the influence of gravity. As far as acceleration is concerned, it reaches its peak value much earlier than the velocity and then sharply drops as the additional momentum transfer to the SBS from the detonation products and soil ejecta decreases.

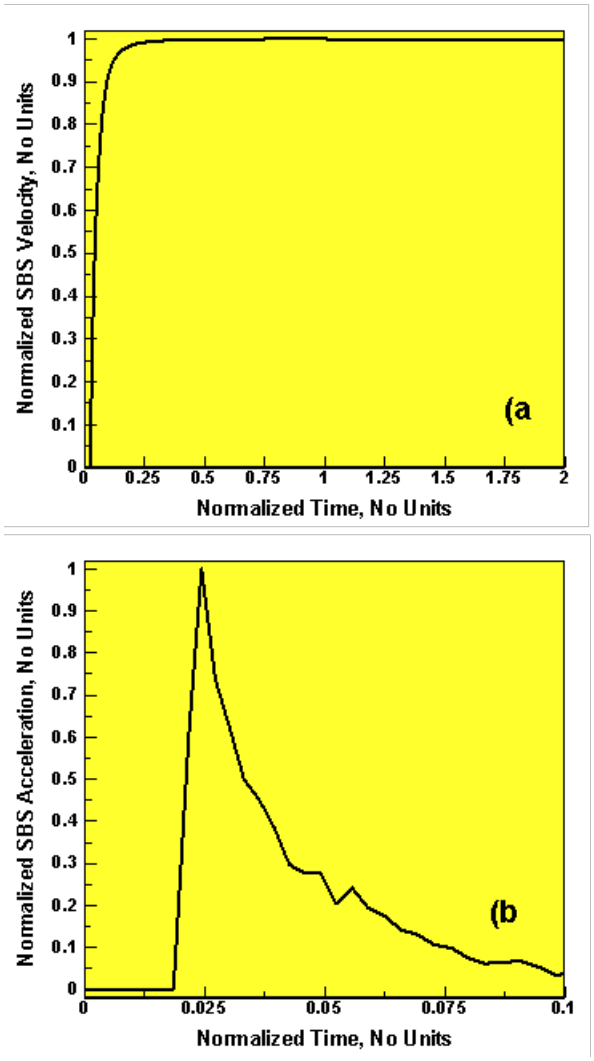

Figure 4–10 Examples of the typical: (a) SBS normalized-velocity vs. time; and (b) SBS normalized-acceleration vs. time results obtained in the present work.

4.5.2. Side-Vent-Channel Shape/Size Optimization Results

The results of the genetic-algorithm-based SBS shape/size optimization procedure are displayed in Figures 4-11(a)–(c) and 4-12(a)–(d). In each of these figures, the x-axis is associated with the transferred-momentum-reduction weighing factor. When this factor is set to 0.0, optimization is completely controlled by the SBS-acceleration-reduction maximization requirements. Contrarily, when this factor is set to 1.0, it is the maximization of the transferred-momentum reduction which controls the optimization process.

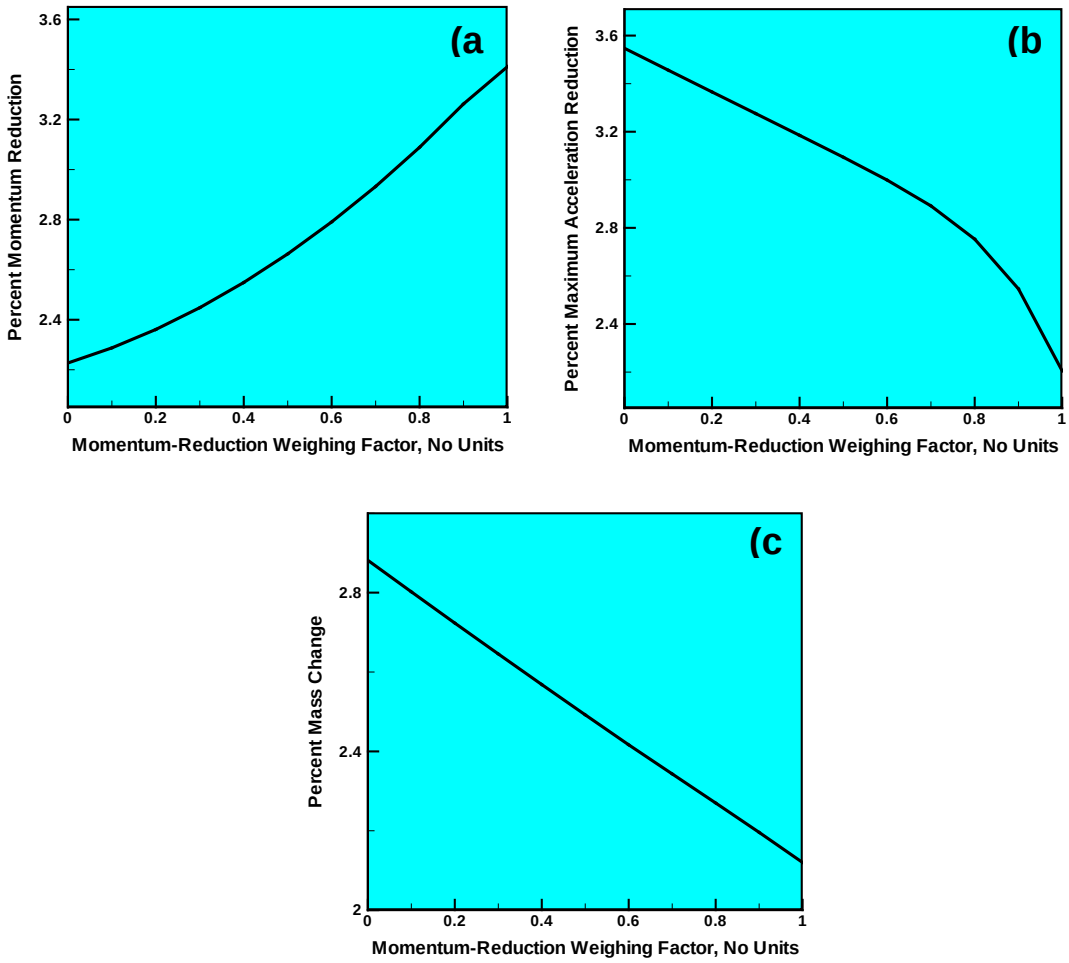

Figure 4–11 Variation in the optimized values of the: (a) percent momentum reduction; and (b) percent maximum acceleration reduction (the two quantities whose weighted sum constitutes the objective function) with changes in the momentum-reduction weighing factor. The reference configuration corresponds to the V-hulled SBS without side-vent-channels. The associated percent change in the SBS mass is depicted in (c).

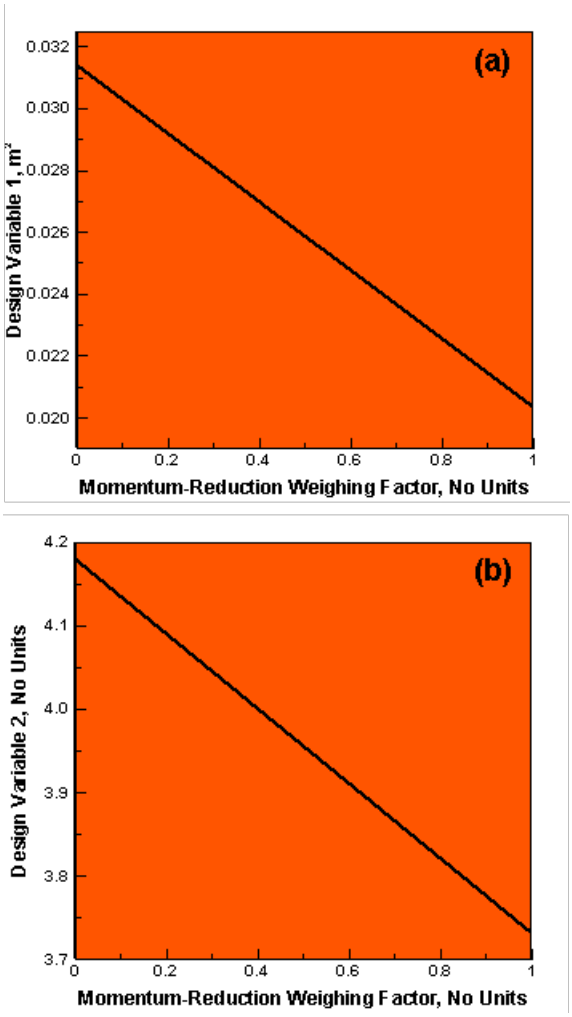

Figure 4–12 Variation of optimum values of the four SBS shape/size design variables as a function of the percent-momentum-reduction weight factor: (a) DV_1 – inlet area; (b) DV_2 – outlet-to-inlet area ratio; (c) DV_3 – fraction of the channel length along which flaring is carried out; and (d) DV_4 – major-to-minor-axes ratio at the side-vent-channel inlet.

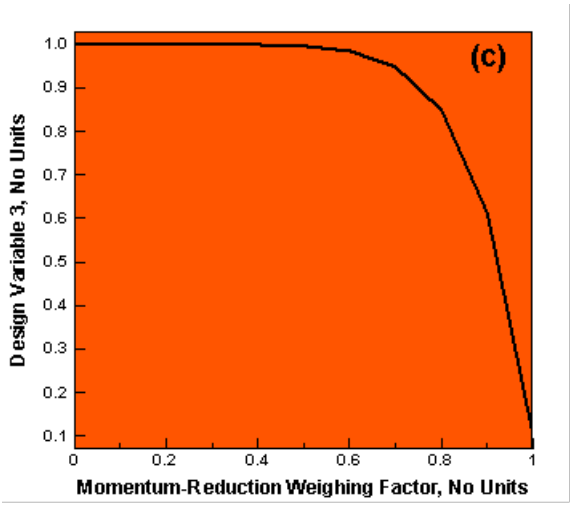

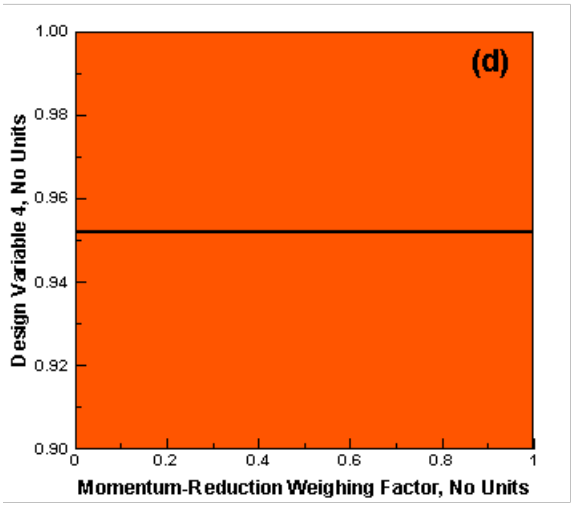

Figure 4-12 Continued.

In Figures 4-12(a)–(d), the optimal values of the four design variables are plotted as a function of the transferred-momentum weighing factor. Examination of the results displayed in these figures reveals that:

(a) as the momentum-reduction weighing factor increases, both the inlet area (DV_1), Figure 4-12(a), and the outlet-to-inlet area ratio (DV_2), Figure 4-12(b), decrease in a monotonic manner. This decrease is associated with a decrease in the SBS mass and is, hence, expected. That is, as more emphasis is placed on the reduction of the transferred momentum to the SBS (through an increase in the momentum-reduction weighing factor), the larger is the tendency of the SBS to acquire a lower-mass configuration. However, the observed changes in DV_1 and DV_2 are not only the reflection of the accompanying changes in the SBS mass, but also are the result of a delicate balance between the competing factors controlling blast-mitigation efficiency of the side-vent-channel solution. Specifically, as the inlet area is increased, more soil particles are allowed to enter the SBS channel. This, initially, increases the blast-mitigation efficiency of the side-vent-channels. However, increase in the inlet area beyond a critical value gives rise to undesirable particle/particle collisions, the collisions which may significantly reduce the blast-mitigation efficiency of the side-vent-channel solution;

(b) the third design variable, DV_3, Figure 4-12(c), which represents the flared fraction of the side-vent-channel length, decreases, at a progressively higher rate, as the momentum-reduction weighing factor increases. This finding can be readily rationalized in terms of the effect of the magnitude of DV_3 on the side-vent-channel mass (at constant levels of the remaining three design variables). That is, as DV_3 increases, the side-vent-channel mass also increases. Consequently, in the maximum-acceleration-reduction regime associated with low values of the

momentum-reduction weighing factor, a larger side-vent-channel mass (i.e. a larger value of DV_3) is preferred. Alternatively, in the maximum-momentum-reduction regime associated with high values of the momentum-reduction weighing factor, a smaller side-vent-channel mass (i.e. a smaller value of DV_3) is preferred. These requirements for the optimum SBS mass are balanced, during the optimization procedure, against the effect of side-vent-channel flaring on its blast-mitigation efficiency. Specifically, if the flared portion of the side-vent-channels is insufficiently long, the beneficial downward-thrust effects are found to be compromised;

(c) the fourth design variable, DV_4, Figure 4-12(d), is fairly insensitive to the magnitude of the momentum-reduction weighing factor. It should be noted that the optimal mean value of DV_4 (0.95) suggests that the side-vent-channels should be of a non-circular cross-section and should have their longer axes aligned with the V-hull. Taking into account the V-hull-apex half-angle (=67.75°), the side-vent-channel cross-section aspect ratio is determined as 1:0.36. This ratio is mainly controlled by the previously defined constraint related to the maximum allowable side-vent-channel extension (beyond the SBS width) in the lateral direction.

4.6. Summary and Conclusions

Based on the results obtained in the present work, the following main summary remarks and conclusions can be drawn:

1. The present work deals with a design-optimization analysis of our recently proposed side-vent-channel concept/solution for mitigation of the blast-loads resulting from a shallow-buried mine detonated underneath a light tactical vehicle.

2. The side-vent-channel concept/solution is based on the use of side-vent-channels attached to the V-shaped vehicle underbody, and was motivated by the ideas and principles of operation of the so-called "***pulse detonation***" rocket engines.

3. To maximize the blast-mitigation potential of the side-vent-channel solution (i.e. the capacity of the solution for reduction in the momentum transferred to, and the maximum acceleration acquired by, the targeted vehicle), a shape/size optimization procedure is employed. Within this procedure, proper shaping and sizing of the side-vent-channels is carried out in order to promote venting of ejected soil and supersonically-expanding gaseous detonation products, and the generation of a downward thrust on the targeted vehicle.

4. The results obtained show that shape/size optimization of the side-vent-channels has a limited ability in enhancing the blast-mitigation potential of the solution beyond the level reported in our prior work for the case of side-vent-channels with a circular cross-section.

4.7 References

1. M. Grujicic, B. d'Entremont, J. S. Snipes, and R. Gupta, "***A Novel Blast-Mitigation Concept for Light Tactical Vehicles***," pending approval from sponsor for manuscript submission, February 2012.

2. M. Grujicic, R. Yavari, J. S. Snipes, S. Ramaswami, and R. Gupta, "***A Combined Finite-Element/Discrete-Particle Analysis of a Side-Vent-Channel-Based Concept for Improved Blast-Survivability of Light Tactical Vehicles***," pending approval from sponsor for manuscript submission, February 2012.

3. http://www.flickr.com/photos/52467065@N03/4872272343/, accessed June 5, 2013.

4. M. Grujicic, G. Arakere, H. K. Nallagatla, W. C. Bell, I. Haque, "***Computational Investigation of Blast Survivability and Off-road Performance of an Up-armored High-Mobility Multi-purpose Wheeled Vehicle (HMMWV)***," Journal of Automobile Engineering, 223, 301–325, 2009.

5. M. Grujicic, G. Arakere, W. C. Bell, I. Haque, "***Computational Investigation of the Effect of Up-armoring on Occupant Injury/Fatality Reduction of a Prototypical High-mobility Multi-purpose Wheeled Vehicle Subjected to Mine-blast***," Journal of Automobile Engineering, 223, 903–920, 2009.

6. http://www.flickr.com/photos/25thcab/6190521808/, accessed June 1, 2013.

7. J. Capouellez, K. Drotleff, G. Wolfe, A. Cichosz, F. Helsel, A. Mikaila, J. R. Pickens , R. W. Semelsberger, S. Kerr, E. Wettlaufer, P. Massoud, J. Wood and B. Barringer, "***Optimized Light Tactical Vehicle***,", 27th Army Science Conference, No. FP-11, 2010, 1–8.

8. M. Grujicic, B. Pandurangan and B. A. Cheeseman, "***The Effect of Degree of Saturation of Sand on Detonation Phenomena Associated with Shallow-buried and Ground-laid Mines***," Shock and Vibration, 13, 41–62, 2006.

9. M. Grujicic, B. Pandurangan, J. D. Summers, B. A. Cheeseman and W. N. Roy, "***Application of the Modified Compaction Material Model to Soil with Various Degrees of Water Saturation***," Shock and Vibration, 15, 79–99, 2008.

10. M. Grujicic, B. Pandurangan, R. Qiao, B. A. Cheeseman, W. N. Roy, R. R. Skaggs and R. Gupta, "***Parameterization of the Porous-Material Model for Sand with Different Levels of Water Saturation***," Soil Dynamics and Earthquake Engineering, 28, 20–35, 2008.

11. M. Grujicic, B. Pandurangan, N. Coutris, B. A. Cheeseman, W. N. Roy and R. R. Skaggs, "***Derivation and Validation of a Material Model for Clayey Sand for Use in Landmine Detonation Computational Analysis***," Multidiscipline Modeling in Materials and Structures, 5, 311–344, 2009.

12. M. Grujicic, B. Pandurangan, N. Coutris, B. A. Cheeseman, W. N. Roy and R. R. Skaggs, "***Computer-simulations based Development of a High Strain-rate, Large-deformation, High-pressure Material Model for STANAG 4569 Sandy Gravel***," Soil Dynamics and Earthquake Engineering, 28, 1045–1062, 2008.

13. M. Grujicic, B. Pandurangan, N. Coutris, B. A. Cheeseman, W. N. Roy and R. R. Skaggs, "***Derivation, Parameterization and Validation of a Sandy-Clay Material Model for Use in Landmine Detonation Computational Analyses***," Journal of Materials Engineering and Performance, 10, 434–444, 2010.

14. M. Grujicic, T. He, B. Pandurangan, W. C. Bell, N. Coutris, B. A. Cheeseman, W. N. Roy and R. R. Skaggs, "***Development, Parameterization and Validation of a Visco-Plastic Material Model for Sand With Different Levels of Water Saturation***," Journal of Materials: Design and Applications, 223, 63–81, 2009.

15. M. Grujicic, B. A. Cheeseman, "***Concurrent Computational and Dimensional Analyses of Design of Vehicle Floor-Plates for Landmine-Blast Survivability***," Journal of Materials Engineering and Performance, submitted for publication, January 2013.

16. M. Grujicic, P. S. Glomski, and B. A. Cheeseman, "***Dimensional Analysis of Impulse Loading Resulting from Detonation of Shallow-buried Charges***," Multidiscipline Modeling in Materials and Structures, accepted for publication, March 2013.

17. P. S. Westine, B. L. Morris, P. A. Cox and E. Polch, "***Development of computer program for floor plate response from land mine explosions***," Contract Report No. 1345, for U.S. Army TACOM Research and Development Center, 1985.

18. B. L. Morris, "***Analysis of Improved Crew Survivability in Light Vehicles Subjected to Mine Blast***," Final Report for Contract No. DAAK70-92-C-0058 for the U.S. Army Belvoir RDEC, Ft. Belvoir, VA, 1993.

19. D. Bergeron, S. Hlady and M. P. Braid, "***Pendulum Techniques to Measure Land Mine Blast Loading***," 17th International MABS Symposium, Las Vegas, USA, June 2002.

20. M. P. Braid, "***Experimental Investigation and Analysis of the Effects of Anti-personnel Landmine Blasts***," Defence R&D Canada, Suffield Special Publication, DRES SSSP 2001-188, December 2001.

21. L. C. Taylor, R. R. Skaggs, and W. Gault, "***Vertical impulse measurements of mines buried in saturated sand***," Fragblast, 9, 19–28, 2005.

22. A. Wenzel, and J. M. Hennessey, "***Analysis and measurements of the response of armor plates to land mine attacks***," Proceedings of the Army Symposium on Solid Mechanics, Warren, MI, 114–128, 1972.

23. E. Buckingham, "***On Physically Similar Systems; Illustrations of the Use of Dimensional Equations***," Physical Review, IV, 345–376, 1914.

24. L. Olovsson, A. G. Hanssen, T. Børvik, "***A particle-based approach to close-range blast loading***," European Journal of Mechanics A/Solids, 29, 1–6, 2010.

25. J. C. Maxwell, "***Illustrations of the Dynamical Theory of Gases***," Philosophical Magazine 19, 19–32, 1860.

26. T. Børvik, L. Olovsson, A.G. Hanssen, K.P. Dharmasena, H. Hansson, H.N.G. Wadley, "***A Discrete Particle Approach to Simulate the Combined Effect of Blast and Sand Impact Loading of Steel Plates***," Journal of Mechanics and Physics of Solids, 59, 940–958, 2011.

27. P.C. Souers, "***Cylinder test on C-4. Report UCRL-TR-230845***," Energetic Materials Center, Lawrence Livermore National Laboratory, Livermore, CA, USA, 2007. https://e-reports-ext.llnl.gov/pdf/347222.pdf [accessed on June 5, 2013]

28. K.J. Frutschy, R.J. Clifton, "***High-temperature pressure-shear plate impact experiments on OFHC copper***," Journal of the Mechanics and Physics of Solids, 46, 1723–1743, 1998.

29. M. Grujicic, B. Pandurangan and A. Hariharan, "***Comparative Discrete-particle vs. Continuum-based Computational Investigation of Soil Response to Impulse Loading***," Journal of Materials Engineering and Performance, 20, 1520–1535, 2011.

30. M. Grujicic, R. Yavari, J.S. Snipes, S. Ramaswami, "***Extension of a Current Continuum-Level Material Model for Soil into the Low-Density Discrete-Particle Regime***," Journal of Materials Engineering and Performance, in press. DOI: 10.1007/s11665-012-0429-3

31. M. Grujicic, W. C. Bell, G. Arakere, I. Haque, "***Finite Element Analysis of the Effect of Up-armoring on the Off-road Braking and Sharp-turn Performance of a High-Mobility Multi-purpose Wheeled Vehicle (HMMWV)***", Journal of Automobile Engineering, 223, D11, 1419–1434, 2009.

32. M. Grujicic, V. Sellappan, M. A. Omar, N. Seyr, A. Obieglo, M. Erdmann and J. Holzleitner, "***An Overview of the Polymer-to-Metal Direct-Adhesion Hybrid Technologies for Load-Bearing Automotive Components***", Journal of Materials Processing Technology, 197, 363–373, 2008.

33. D. E. Goldberg, "***Genetic Algorithms in Search, Optimization and Machine Learning***", Addison-Wesley, Reading, MA 1989.

CHAPTER 5: CONCLUSIONS AND SUGGESTIONS FOR FUTURE WORK

5.1. Conclusions

While each of the chapters 2 through 4 contains a summary of the conclusions resulting from the work reported in these chapters, a list of more general conclusions arrived at the end of the present work is presented in the remainder of this section. This list includes:

1. Advanced engineering-analysis methods and tools are continuously improving and reaching the level of physical fidelity and accuracy making them valuable tools for design, concept validation and performance prediction of complex mechanical systems (e.g. the side-vent-channel blast mitigation solution, in the present case).

2. Specifically, in the present work, combined Eulerian/Lagrangian fluid structure interaction (FSI) transient non-linear finite-element based method and a combined Finite-Element/Discrete-Particle transient non-linear finite element method, in conjunction with the advanced evolutionary design-optimization methods (like the Genetic algorithm) were found to be extremely valuable when assessing the blast mitigation potential of the newly proposed side-vent-channel blast mitigation solution.

3. When designing blast protection systems like the flared side-vent channel solution proposed in the present work, care should be taken in order to properly define the quantities/metrics which capture and quantify the blast mitigation potential of the system being investigated. However, due to the intrinsic complexity of the problem involving detonation of a shallow buried mine (located underneath a light tactical military vehicle), and the subsequent interactions of the air-born blast waves, soil ejecta, gaseous detonation products and mine fragments with the target vehicle, this task is quite challenging.

4. The present work clearly rationalized that when designing and optimizing a blast-mitigation solution (like the flared side-vent channel solution, proposed in the present work), a

trade-off between the conflicting requirements regarding the minimum momentum transfer to the target vehicle (promoted by the minimum vehicle mass), and the minimum initial acceleration of the vehicle (promoted by the maximum vehicle mass) must be addressed.

5. While the use of the design optimization analysis to maximize the performance of the blast-mitigation solution under specific mine-blast scenarios shows some potential, its general utility is questionable considering the stochastic nature of the blast-detonation events (e.g. size and shape, depth of burial and relative location of shallow buried mine with respect to vehicle).

6. While the observed blast-mitigation effects offered by the newly proposed flared-side-vent-channel solution of 3 to 4 percent may appear relatively small, to designers of blast-resistant military vehicles, these effects are generally considered to be noteworthy.

5.2. Suggestions for Future Work

The present work can be extended in a number of ways and directions. One of these directions is further development of the flared side-vent channel blast-mitigation concept itself. For example, the present concept involves a constant V-hull half angle. This constraint can be removed and the V-hull be allowed to have a more complex geometry. Also, further improvements in the methods and tools used to analyze the potential of the proposed flared-side-vent channel solution can be made. For example, in chapters 2 and 3 key limitations of the utilized combined Eulerian/Lagrangian and the combined Finite-Element/Discrete-Particle computational algorithms were identified. Some of these limitations can be removed through the utilization of combined finite-element/discrete-particle/fluid-continuum computational approach. This approach will enable a more accurate modeling of the interactions between the discreet ejected particles of soil and the gas phase (consisting of air and gaseous detonation products).

In the majority of the computational analyses carried out in the present work, the vehicle structure was assumed to be of a rigid nature. This was done in order to reduce the computational cost. To more comprehensively assess the blast-mitigation potential of the present solution, the vehicle structure flexibility, deformability and potential damage/failure of the vehicle structure should be taken into account.